Title

Lower free-tropospheric mixing and the transition to tropical deep convection: observational estimates and biases in global climate models

Author

Emmenegger, Todd

Publication Date

2024

Peer reviewed|Thesis/dissertation

UNIVERSITY OF CALIFORNIA

Los Angeles

Lower free-tropospheric mixing and the transition to tropical deep convection: observational estimates and biases in global climate models

A dissertation submitted in partial satisfaction

of the requirements for the degree

Doctor of Philosophy in Atmospheric and Oceanic Sciences

by

Todd Emmenegger

2024

ABSTRACT OF THE DISSERTATION

Lower free-tropospheric mixing and the transition to tropical deep convection: observational estimates and biases in global climate models

by

Todd Emmenegger

Doctor of Philosophy in Atmospheric and Oceanic Sciences

University of California, Los Angeles, 2024

Professor J. David Neelin, Chair

Conditional instability and the buoyancy of convective plumes drive moist convection in the tropics but have a variety of representations in model convective schemes. Generally, instability—generated on the large-scale—is removed by local convection and precipitation. This process is reflected in statistical relationships between precipitation and bulk column measures of relevant variables, such as humidity and CAPE. A first-order relationship that can be leveraged for climate model diagnostics is the precipitation 'pickup' in which precipitation conditionally averaged on humidity undergoes a sharp, sudden increase. The strength and location of the pickup—referred to as the critical point—is used to assess model sensitivity to lower-free tropospheric moisture. Observational data from the Atmospheric Radiation Measurement (ARM) permanent field observational sites are augmented with satellite observations of precipitation and temperature as an observational baseline. Coupled Model Intercomparison Project Phase 6 (CMIP6) models are assessed. Models perform relatively well in regards to the critical point of the pickup when model temperature biases are accounted for. The conditional average precipitation is decomposed into the product of the probability of raining and mean precipitation during raining times (conditional intensity), showing that models which do perform well do so through compensating biases—model conditional intensity that is too low at a given humidity is compensated in part by excessive

probability of precipitation.

Biases uncovered are further explored with the use of an entraining plume model. The estimation of a bulk plume entrainment rate which we term the "pseudo-entrainment," captures the trade-off between lager temperature lapse rates and smaller subsaturation across the models. This pseudo-entrainment diagnostic is also a reasonable indicator of the critical value of integrated buoyancy for precipitation onset.

Using a combination of reanalysis and observational products (ARMBE, COSMIC2, and ERA5), the precipitation onset is expressed as a weighting between CAPE-like and subsaturation-like factors, here including the condensate loading and direct water vapor effect on buoyancy. The evolution of convection and its feedback to the environment are shown to have a considerable impact in making this relationship more precise. Virtual and condensate effects have a significant effect on plume buoyancy; however, the weighting between instability and subsaturation proves robust when these effects on plume buoyancy are introduced.

The dissertation of Todd Emmenegger is approved.

Gang Chen

Rong Fu

Karen McKinnon

J. David Neelin, Committee Chair

University of California, Los Angeles

2024

To my parents, Jan and Kurt,

and my siblings, Branson and Ansley

Contents

List of Figures

Acknowledgements

Chapter 1 contains figures from Zhang et al. (2020a) and Turk et al. (2022). The work performed in Zhang et al. (2020a) was supported by the DOE ARM program and performed under the auspices of the U. S. Department of Energy by Lawrence Livermore National Laboratory under contract No. DE-AC52-07NA27344. I would like to thank Jill Zhang, Cheng Tao, and Shaocheng Xie for hosting me at LLNL for collabaorative work.

Chapter 2 contains work from Emmenegger et al. (2022) which was supported under U.S. Department of Energy Grant DE-SC0011074 and subcontract B634021 and National Science Foundation AGS-1936810. I would like to acknowledge the U.S. Department of Energy's Atmospheric Radiation Measurement (ARM) program and the Program for Climate Model Diagnosis and Intercomparison to Earth System Science Portals for making CMIP data available. I would like to thank Dr. Kathleen Schiro for discussion and for providing an initial set of scripts that the current diagnostics built upon, as well as Dr. Wuyin Lin for providing the high frequency E3SM output.

Chapter 3 contains a version of Emmenegger et al. (2024). This work was supported under National Science Foundation AGS-1936810, NOAA NA21OAR4310280, the DOE DE-SC0022995, and NASA grant 80NM0018F0617 and also partially supported by the U.S. Department of Energy's Atmospheric Radiation Measurement program (ARM). I would like to thank my coauthors Yi-Hung Kuo and Fiaz Ahmed for their help during the research and writing process.

The contents of Chapters 2 and 3 were published in the *Journal of Climate*, ©American Meteorological Society 2022, 2024. Chapter 4 contains a draft of a manuscript in progress. This work has been supported under National Science Foundation AGS-2414576.

I would like to especially thank Yi-Hung Kuo for letting me distract him from his work to help me with research and coding on an almost daily basis. Fiaz Ahmed always found time to help me out when the research became tricky. I would also like to thank Shoacheng Xie and Joe Turk for the opportunities they've provided for me at LLNL and JPL. I would like to extend my gratitude to Baird Langenbrunner for his AOS112 python scripts, which made my life as a TA a whole lot easier.

Lastly, I am very grateful and fortunate to have been advised by David Neelin, whose guidance made no problem feel insurmountable.

Vita

EDUCATION

University of California, Los Angeles, CA

M.S. Atmospheric and Oceanic Sciences — November 2022

University of Georgia

B.S. Mathematics — July 2017

ACADEMIC EXPERIENCE AND AWARDS

Jacob A. Bjerknes Award — February 2022

Graduate Researcher/Subcontractor, LLNL — March 2019 - September 2020

Researcher, UNC Chapel Hill Wave Propagation Lab — August 2017 - August 2018

REU Participant Penn State Dept of Meteorology — May 2016 - August 2016

Concept Development, UGA Small Satellite Lab — January 2017 - August 2017

Research Assistant, UGA Dept of Geography — October 2015 - August 2017

PUBLICATIONS

1. Emmenegger, T., Ahmed, F., Kuo, Y. H., Xie, S., Zhang, C., Tao, C., & Neelin, J. D. (2024). The physics behind precipitation onset bias in CMIP6 models: the pseudo-entrainment diagnostic and trade-offs between lapse rate and humidity. *Journal of Climate,* **37(6)**, 2013-2033.
2. Turk, F.J., Cardellach, E., de la Torre-Juárez, M., Padullés, R., Wang, K.N., Ao, C.O., Kubar, T., Murphy, M.J., Neelin, J.D., Emmenegger, T. and Wu, D., 2024. Advances in the Use of Global Navigation Satellite System Polarimetric Radio Occultation Measurements for NWP and Weather Applications. *Bulletin of the American Meteorological Society*, **105(6)**, E905-E914.
3. Emmenegger, T., Kuo, Y. H., Xie, S., Zhang, C., Tao, C., & Neelin, J. D. (2022). Evaluating Tropical Precipitation Relations in CMIP6 Models with ARM data. *Journal of Climate*, **35(19)**, 2743-2760.
4. Turk, F. J., Padullés, R., Morabito, D. D., Emmenegger, T., & Neelin, J. D. (2022).

Distinguishing Convective-Transition Moisture-Temperature Relationships with a Constellation of Polarimetric Radio Occultation Observations in and near Convection. *Atmosphere*, **13(2)**, 259.

5. Zhang, C., Golaz, J. C., Forsyth, R., Vo, T., Xie, S., Shaheen, Z., ... & Ullrich, P. (2022). The E3SM Diagnostics Package (E3SM Diags v2. 6): A Python-based Diagnostics Package for Earth System Models Evaluation. *Geoscientific model development discussions, 2022,* 1-35.

6. Zhang, C., Xie, S., Tao, C., Tang, S., Emmenegger, T., Neelin, J. D., ... & Shaheen, Z. (2020). The ARM Data-Oriented Metrics and Diagnostics Package for Climate Models: A New Tool for Evaluating Climate Models with Field Data. *Bulletin of the American Meteorological Society,* **101(10)**, E1619-E1627.

INVITED TALKS

1. "An assessment of entrainment and precipitation onset over the tropical pacific in observations and CMIP6 models." 2nd PAZ Polarimetric Radio Occultations User Workshop, Co-organized by JPL and ICE-CSIC/IEEC, Keck Center, California Institute of Technology, Pasadena, CA. November 29, 2023.

2. "The Physics Behind Precipitation Onset Bias in CMIP6 Models: The Pseudo-entrainment Diagnostic and Trade-offs Between Lapse Rates and Humidity." Earth Science Seminar, Jet Propulsion Laboratory, Pasadena, CA. August 22, 2022.

Chapter 1

Introduction

1.1 Background and Overview

Poorly constrained representations of tropical deep convection and precipitation are major contributors to uncertainty in Global Climate Model (GCM) projections. Past and present generations of GCM precipitation output has been shown to be too insensitive to free-tropospheric moisture, and numerous studies have reported significant model improvement with more realistic representations of entrainment. With the aid of entraining plume models and their physical assumptions, we construct novel constraints for tropical convection, intorudcing a simple metric that estimates model entrainment to quantify biases in temperature and moisture.

This disseration discusses published and to be published work evaluating observational and GCM sensitivity to moisture. Chapter 2 discusses an analysis of GCM model behavior published in Emmenegger et al. (2022), where diagnostics based on simple, statistical relationships between the environment and precipitation are used to evaluate the moisture dependence of convection in a cohort of CMIP6 models. A first-order test using precipitation conditionally-averaged on column water vapor (CWV) shows a large intermodel spread in the transition to deep convection. When temperature dependence is accounted for by

diagnostics based on column relative humidity (CRH)—normalizing CWV by it saturation value—biases in CWV sensitivity are generally compensated for and models show convective onset at environmental conditions similar to observations. However, a closer inspection of this transition reveals a drizzle bias in models in where precipitation occurs too often at low intensities.

Physically, the sensitivity of the environment to CRH is due to the mixing of environmental air into buoyant plumes, or entrainment. In chapter 3, I discuss work published in Emmenegger et al. (2024) where biases in convective onset are investigated more thoroughly through the use of an entraining plume model. The vertical profiles of moisture and temperature using θ_e are assessed among the same CMIP6 model cohort as chapter 2. Applying the small-buoyancy assumption—the environmental temperature rapidly adjusts to minimize buoyancy—to raining-times average profiles presents biases in the vertical profiles of temperature and moisture as a consequence of inaccurate mixing. It is shown that if models do not apply the correct mixing rate, they must compensate between temperature and moisture biases, but are not able to correctly capture both.

Chapter 4 contains current work relating to analytical expression of LFT buoyancy while retaining the microphysical effects of water vapor and condensate. A measure of LFT buoyancy is expressed as a weighting between CAPE-like and subsaturation-like quantities. Using observational and reanalysis products: ARMBE, COSMIC2, and ERA5, it is shown that both quantities contribute equally to buoyancy. The evolution of these quantities during convection are evaluated and emphasize the importance of time dependence in assessing convective transition.

The remainder of this chapter contains summaries of collaborative work on other publications I was a part of.

1.2 ARM-DIAGS Python Package for Climate Model evaluation: Zhang et al. (2020a)

The ARM-DIAGs package uses comprehensive datasets from the Atmospheric Radiation Measurement (ARM) campaign to provide a suite of standard metrics and diagnostics to evaluate climate model performance (Zhang et al., 2020a). The convective onset metrics are derived from the robust relationship between CWV, precipitation, and temperature at ARM sites to evaluate the convective transition from model output and can discern between different convective parametrizations. Figure 1.1 shows the convective transition statistics for E3SM model output. The transition to deep convection, represented by strong increase in the conditional average precipitation in Fig 1.1a, shows that the E3SM model begins the transition to deep convection at too low CWV (black dots) when compared to observations (blue dots). As the column is relatively dry compared to observations during convection, the physical interpretation is the E3SM model convective scheme mixes too little—a plume originating in the boundary layer cannot entrain too much of this dry air and remain buoyant. The convective trigger function can also be inferred from 1.1b, where the probability of precipitation increases linearly after a critical value. The CWV PDF (1.1c) is limited on the right by the moisture sink of precipitation. Since the E3SM model mixes too little in its convective scheme, its environment does not moisten sufficiently compared to observations. This illustrates how the mixing rate affects the mean state—climatological humidity here—of models.

1.3 Convective Transition In and Near Radio-Occultations: Turk et al. (2022)

The relationship between convective onset and lower-free tropospheric moisture (q_{LFT}) arises from the effect of entrainment on convective updrafts. Higher q_{LFT} air dilutes the convective

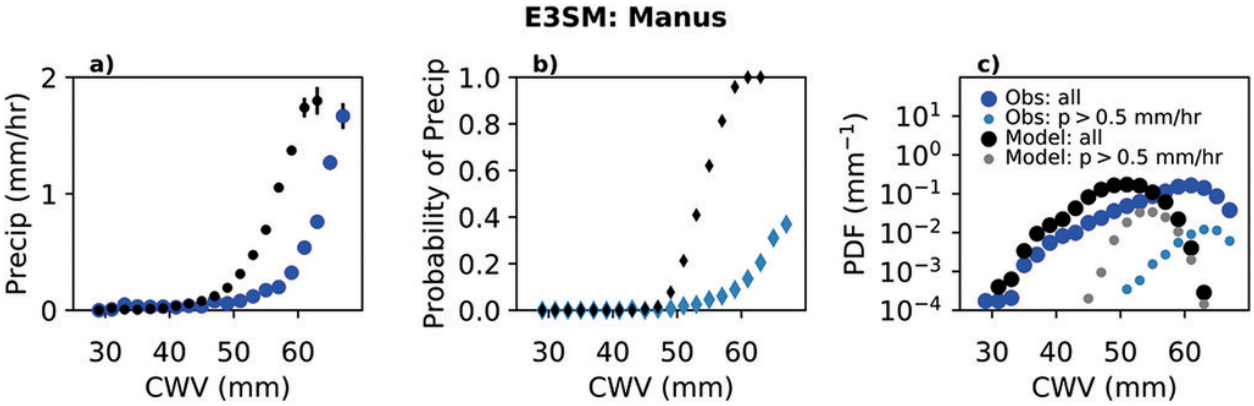

Figure 1.1: (a) Precipitation conditionally averaged on CWV for observations based on ARMBE precipitation and gap-filled Microwave Radiometer Retrievals (MWRRET) of CWV (blue) and E3SM model output (black) over Manus Island. (b) As in (a), but for precipitation probability (the number of CWV observations with rain rates greater than a small threshold, here 0.5 mm h–1, divided by the total number of CWV samples in each bin). (c) The PDFs of CWV for observations (dark blue) and model (black) and of the contribution to this from points with precipitation exceeding 0.5 mm h–1 for observations (light blue) and model (gray). Originally published in Zhang et al. (2020a)

updraft less in its ascent, lending the updraft higher buoyancy hence more vigorous convection. Figure 1.2 shows precipitation conditionally averaged on q_{LFT}. Model precipitation (color lines) appear to increases at a much weaker rate with increasing q_{LFT} when compared to ARM (solid-black line). This metric does not take temperature dependence of conditional instability into account.

Conditional-averaging precipitation on a temperature dependent measure (subsaturation, the difference between equivalent potential temperture and equivalent potential saturation temperature, $\theta_e^{LFT} - \theta_{es}^{LFT}$) as in Figure 1.3b, makes the model pick up their precipitation at a stronger rate more similar to ARM. Figure 1.3a shows average vertical profiles of θ_e and θ_{es} 3 hours before a precipitating event begins. The orange-shaded region represents an integrated measure of undiluted buoyancy (nomixing CAPE) by raising air from the surface, which conserves its θ_e (solid line) and comparing it to the environmental θ_{es} (dotted line). Models with more (less) CAPE before the start of the event are more (less) dependent on LFT moisture. The NASA-GISS model (blue line) has moister surface air (θ_e) and a cooler

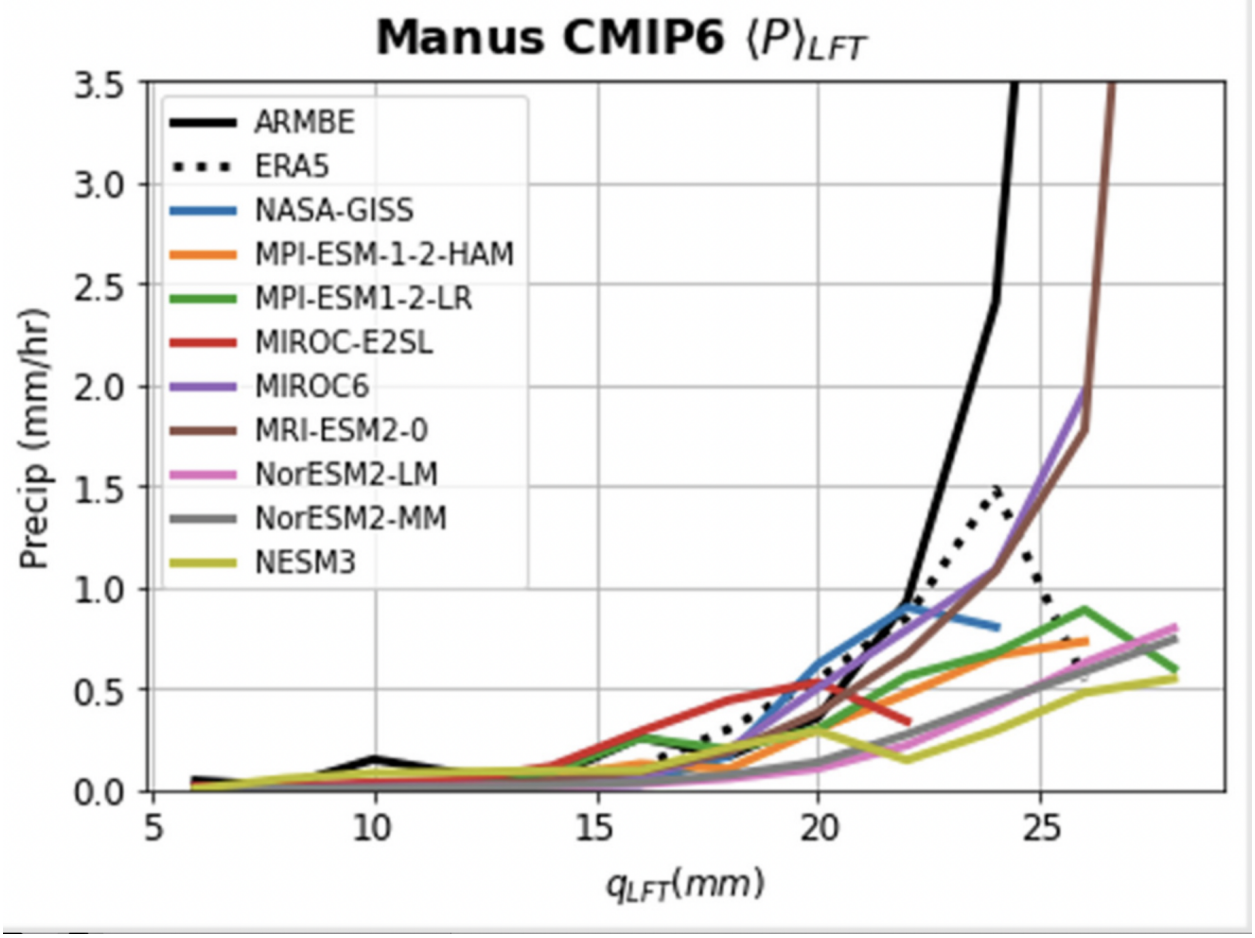

Figure 1.2: Precipitation rate ($\mathrm{mm\,h^{-1}}$) conditionally averaged as a function of lower free-tropospheric water vapor q_{LFT} (units of mm) from ten CMIP6 models (colored lines), relative to the ARM Best-Estimate observations (solid black line). Originally published in Turk et al. (2022)

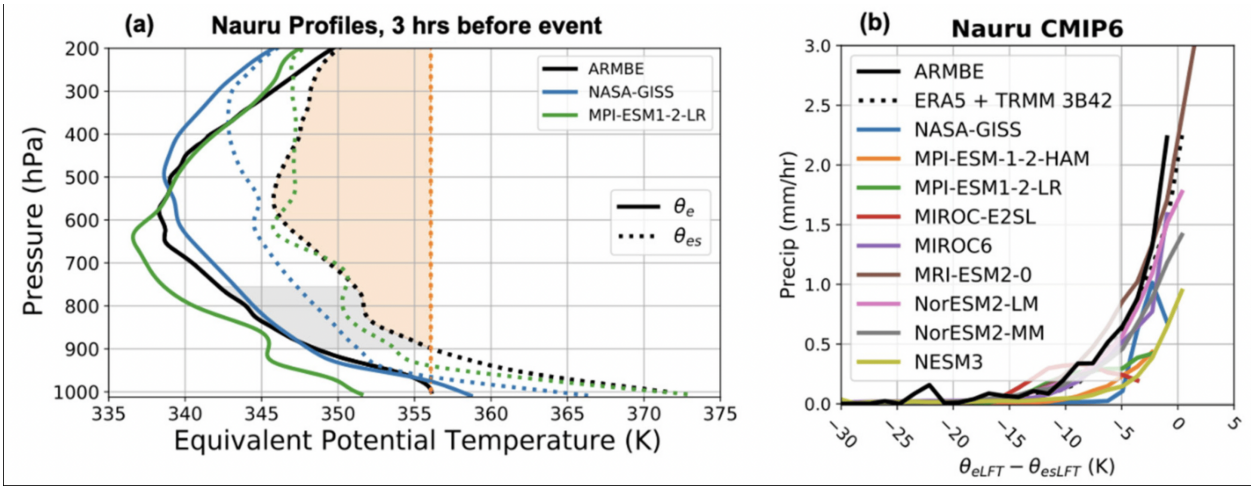

Figure 1.3: Using vertical profile information to assess convective conditions in CMIP6 models. (a) Vertical profiles of equivalent potential temperature θ_e(solid curves) and saturation equivalent potential temperature θ_{es} (dashed curves) at the Nauru island ARM site for the ARM Best-Estimate observations (ARMBE) and two examples of CMIP6 climate models (denoted NASA-GISS and MPI-ESM1-2-LR). The vertical axis is in units of pressure (1 hPa = 100 Pa). The profiles are for conditions 3 h prior to precipitation exceeding 0.5 mm h^{-1}, as a measure of typical profiles associated with onset of deep convection. For the observed curves, the orange shaded area gives a measure of conditional instability for a non-entraining parcel, and the gray area indicates the subsaturation ($\theta_e - \theta_{es}$) in the lower troposphere (750–900 hPa) that reduces conditional instability when entrained into the convective plume. (b) Precipitation conditionally averaged on this subsaturation ($\theta_e - \theta_{es}$) in the lower troposphere (750-900 hPa layer) for ARMBE observations and several CMIP6 models. Originally published in Turk et al. (2022)

LFT (using θ_{es} showing it has more CAPE on average at the beginning of an event, while its pickup in precipitation (Figure 1.3b occurs at a significantly moister environment.

Chapter 2

Evaluating Tropical Precipitation Relations in CMIP6 Models with ARM data

Abstract

A set of diagnostics based on simple, statistical relationships between precipitation and the thermodynamic environment in observations is implemented to assess Coupled Model Intercomparison Project Phase 6 (CMIP6) model behavior with respect to precipitation. Observational data from the Atmospheric Radiation Measurement (ARM) permanent field observational sites are augmented with satellite observations of precipitation and temperature as an observational baseline. A robust relationship across observational datasets between column water vapor (CWV) and precipitation, in which conditionally-averaged precipitation exhibits a sharp pickup at some critical CWV value, provides a useful convective onset diagnostic for climate model comparison. While a few models reproduce an appropriate precipitation pickup, most models begin their pickup at too low CWV and the increase in precipitation with increasing CWV is too weak. Convective transition statistics compiled

in column relative humidity (CRH) partially compensate for model temperature biases—although imperfectly since the temperature dependence is more complex than that of column saturation. Significant errors remain in individual models and weak pickups are generally not improved. The conditional-average precipitation as a function of CRH can be decomposed into the product of the probability of raining and mean precipitation during raining times (conditional intensity). The pickup behavior is primarily dependent on the probability of raining near the transition and on the conditional intensity at higher CRH. Most models roughly capture the CRH dependence of these two factors. However, compensating biases often occur: model conditional intensity that is too low at a given CRH is compensated in part by excessive probability of precipitation.

2.1 Introduction

The U.S. Department of Energy (DOE)'s Atmospheric Radiation Measurement (ARM) program provides unique field observations at its tropical and subtropical sites for exploring the complex interactions and relationships between clouds, aerosols, and radiation and their associated large-scale environments (Mather and Voyles, 2013; Xie et al., 2010; Zhang et al., 2020b). Bretherton et al. (2004) identified a robust nonlinear relationship between column water vapor (CWV) and precipitation, ($\langle P \rangle$), conditionally averaged by CWV bin. At sufficiently high temporal and spatial resolution, conditionally averaged precipitation ramps up once a critical CWV has been reached. That is, for CWV values past a certain threshold, the expected rate of precipitation begins to increase rapidly or 'pickup.' The CWV-precipitation relationship applies to both mesoscale and smaller convective scales and is observed over tropical land and ocean in observational records (Neelin et al., 2009; Schiro, 2017) and some models (Kuo et al., 2020). This sharp increase in precipitation represents the occurrence of conditional instability in the transition to deep convection as a function of thermodynamic conditions (Schiro et al., 2016a). Holloway and Neelin (2009a)

assessed this transition with radiosondes from the tropical western pacific ARM site Nauru, concluding that CWV serves as a proxy for the role of free tropospheric humidity on the buoyancy of entraining plumes. Plume buoyancy is highly sensitive to entrainment and mixing of environmental air; the importance of free-tropospheric humidity to the onset of deep convection is well known and is reflected in the pickup (Ahmed and Schumacher, 2015; Bretherton et al., 2004; Kuo et al., 2018; Neelin et al., 2009). Recent work has focused on the conditional average temporal evolution associated with this transition (Wolding et al., 2020).

The onset of deep convection is a complex process, and realistic representations of it in climate models are necessary for accurate simulations of convective-precipitation statistics (Sahany et al., 2012). In past generations of Global Climate Models (GCMs), model precipitation has been shown to be too insensitive to free-tropospheric humidity, leading to errors on a range of spatial and temporal scales. A number of studies (Bechtold et al., 2008a; Neale et al., 2008; Neelin et al., 2010; Sahany et al., 2012; Zhao et al., 2009) have identified significant model improvement with more realistic representations of entrainment and mixing (Schiro et al., 2016a). Kuo et al. (2020) compared pairs of models which differ primarily in their moist convective parameterization schemes (e.g. the GFDL AM4 variants AM4G9 [double-plume convective scheme] and the AM4B6 [Donner convective scheme]) and concluded that the basic convection onset statistics can distinguish convective parametrizations. A large intermodel spread in tropical precipitation presents a challenge towards future climate projections (Biasutti, 2013; Biasutti and Sobel, 2009; Maloney et al., 2019; Su et al., 2017; Voigt et al., 2016). Tropical precipitation contributes significantly to biases in climatologies and large-scale modes of tropical variability such as the MJO (Del Genio, 2012; Jiang et al., 2017; Zhu and Hendon, 2015), the diurnal cycle of precipitation (Covey et al., 2016; Del Genio and Wu, 2010; Hourdin et al., 2013; Rio et al., 2009), and the double ITCZ (Hirota et al., 2014; Hwang and Frierson, 2013; Mapes and Neale, 2011; Oueslati and Bellon, 2013; Tian and Dong, 2020).

Model diagnostics of tropical convection play an integral part in understanding the

limitations of model behavior in future warming scenarios; this study explores biases in tropical precipitation related processes across a model cohort from the recent Coupled Model Intercomparison Project Phase Six (CMIP6). The analysis tools presented in this work form part of the ARM data-oriented metrics and diagnostics package (ARM-DIAGS) (Zhang et al., 2020b), to facilitate process-level evaluation of climate models using ARM datasets. After overviewing data and models (section 2), in section 3 we present the convective transition statistics at two tropical western pacific sites, Manus and Nauru, highlighting the important features of the observed datasets and discuss and compare CMIP6 model behavior. In section 4 we discuss the influence of temperature in the surrounding large scale environment and identify potential biases of models. In section 5 we present the statistics compiled in column-relative humidity as a way of reducing model temperature bias in the diagnostics.

2.2 Data and Models

The ARM program datasets of precipitation and CWV are used as an observational baseline in the model comparison in evaluating the relationship of CWV and precipitation. Here we present the results from two Tropical Western Pacific ARM sites: Nauru (0°31'S, 166°54'E) for the period 1999-2009 and Manus (2°3'S, 147°25'E) for 1998 - 2010. ARM sites use a Microwave Radiometer for CWV measurements and an Optical Scientific optical rain gauge (ORG815) for precipitation (hereinafter referred to as ORG). CWV measurements are recorded every 20 s but exhibit gaps due to the 'wet-window' problem in which water collects on the surface of the lens and introduces erroneous measurements during intense precipitation. As in Schiro et al. (2016a), the wet-window problem is addressed by a linear interpolation of CWV values across time periods of 6 hours or less. The wet-window problem primarily affects high CWV bins and the interpolation is often across short timescales and underestimates peak CWV (Schiro et al., 2016a). CWV during strong precipitation events does not diminish rapidly—typically on the scale of hours (Schiro et al., 2016a).

In addition to the in-situ precipitation data, satellite retrieval Tropical Rainfall Measuring Mission (TRMM) 3B42 version 7 precipitation measurements (Mission, 2011) are augmented with the in-situ CWV. In model evaluation, TRMM 3B42 data is averaged spatially over 1° from its 0.25°×0.25° resolution, centered on the lat-lon point nearest to the sites.

Here we analyze 11 CMIP6 models and include the one-hourly European Center for Medium-Range Weather Forecasts Reanalysis 5th Generation (ERA5) atmospheric reanalysis product (Hersbach et al., 2020); model and the reanalysis data used are summarized in Table 1. Six-hourly snapshots of three-dimensional moisture and temperature, and three-hourly averaged precipitation rates are extracted from the model cohort for the years 1995-2015 of their historical experiment. The Department of Energy (DOE) E3SM project provides data from two simulations: E3SM-1-0 0.25 × 0.25, a 21-year, high-resolution coupled simulation forced with repeating annual cycle forcing approximating observed conditions in 1950 (Caldwell et al., 2019) and E3SM-1-0-EAM 1.00 × 1.00, a 6-year atmosphere-only Atmospheric Model Intercomparison Project (AMIP) climatology run using present-day climate forcing for the year 2000, with climatological sea-surface temperature and sea-ice prescribed from observations (Rasch et al., 2019; Xie et al., 2018; Zhang et al., 2019). These models were chosen based on availability of six-hourly three-dimensional snapshots of temperature and moisture and three-hour-average precipitation data in the Earth System Grid Federation archive at the time of analysis.

The data for each model is extracted from the nearest point to each ARM site. The column for CWV is defined as the surface to 200 mb. Precipitation data for NASA-GISS, MPI-ESM1-2-LR, MIROC-E2SL, MIROC6, MRI-ESM2-0, NESM3, E3SM-1-0-EAM and E3SM-1-0 is three hourly averaged output, while MPI-ESM1-2-LR, NorESM2-LM, and NorESM2-MM output is six hourly averaged. The effects of using different temporal averaging windows in the statistics are discussed in the beginning of Section 3. With the exception of the E3SM-1-0-EAM, all model outputs are from coupled ocean-atmosphere GCMs. Model CWV data for all models are six hourly instantaneous snapshots. CWV is analyzed as causal to

Model name	Institute	Resolution (lon × lat), vertical levels	Convective Trigger/Closure	References
NASA-GISS	Goddard Institute for Space Studies, NASA	2.00° × 2.00°, 40	Higher moist static energy of an adiabat to environment at level above/Cloud-base buoyancy	DelGenio and Yao (1993); NASA Goddard Institute for Space Studies (NASA/GISS) (2018); Schmidt et al. (2014)
MPI-ESM-1-2-HAM	Max Planck Institute for Meteorology	1.85° × 1.88°, 47	Net positive moisture convergence/CAPE	Möbis and Stevens (2012); Wieners et al. (2019a)
MPI-ESM1-2-LR	Max Planck Institute for Meteorology	1.85° × 1.88°, 47	Net positive moisture convergence/CAPE	Möbis and Stevens (2012); Wieners et al. (2019b)
MIROC-E2SL	Japan Agency for Marine-Earth Science and Technology	2.77° × 2.81°, 40	CAPE/Prognostic convective kinetic energy	Ando et al. (2021); Hajima et al. (2019)
MIROC6	Japan Agency for Marine-Earth Science and Technology	1.39° × 1.41°, 81	CAPE/Prognostic convective kinetic energy	Ando et al. (2021); Tatebe and Watanabe (2018)
MRI-ESM2-0	Meteorological Research Institute Japan Meteorological Agency	1.11° × 1.13°, 80	CAPE/CAPE	Yukimoto et al. (2019, 2011)
NorESM2-LM	Norwegian Meteorological Institute	1.89° × 2.50°, 32	CAPE/CAPE	Seland et al. (2020, 2019)
NorESM2-MM	Norwegian Meteorological Institute	0.94° × 1.25°, 32	CAPE/CAPE	Bentsen et al. (2019); Seland et al. (2020)
NESM3	Nanjing University of Information Science and Technology	1.85° × 1.88°, 47	Net positive moisture convergence/CAPE	Cao and Wang (2019); Cao et al. (2018)
E3SM-1-0	DOE E3SM Project	0.25° × 0.25°, 72	CAPE CAPE	Caldwell et al. (2019)
E3SM-1-0-EAM	DOE E3SM Project	1.00° × 1.00°, 72	CAPE CAPE	Rasch et al. (2019)

Table 2.1: List of models analyzed in this study. Table is similar to the table in Pathak et al. (2019) for CMIP5 models. The references column gives the data source and the source for the convective trigger/closure.

precipitation, the start of the precipitation averaging window coincides with the time of the CWV snapshot, or precipitation lags CWV. The statistics presented in the following sections were also evaluated with precipitation leading CWV and the statistics remained robust (not shown). We note the caveat that the ARM radiometer CWV is measured locally, as opposed to the model values from a grid cell on the order of $(100\ \mathrm{km})^2$ and is available at higher time resolution. The comparison remains reasonable given that CWV tends to have longer spatial and temporal autocorrelation than precipitation (Holloway and Neelin, 2010; Kuo et al., 2018; **?**) and that coarse-graining of data on scales from 25-200 km has modest impacts (Kuo et al., 2018). The spatial dependence of the convective onset statistics are further explored in Section 3.

In section 4, we address the temperature dependence of the moisture-precipitation relationship which requires a calculation of the column-integrated (from the surface to 200 mb) saturation specific humidity, $\widehat{q_{sat}}$, $\widehat{q_{sat}} \equiv g^{-1} \int q_{sat}\big[T(p), p\big] dp$ where $q_{sat}\big[T(p), p\big]$ is the saturation humidity with respect to liquid water, is used as a bulk measure of tropospheric temperature. The column relative humidity for observations is calculated from one-hourly snapshots of CWV and temperature of the ARM Best Estimate data (ARMBE)(Xie et al., 2010), an hourly integrated product assembled from various ARM measurements for use in climate model evaluation. Stringent quality controls were applied to raw ARM data used in producing ARMBE. The one-hourly snapshots at the beginning of the precipitation averaging window are chosen for the ARMBE statistics, remaining consistent with the causal relationship of CWV to precipitation. Model $\widehat{q_{sat}}$ is calculated from six-hourly snapshots and treated in the same fashion as CWV in that it leads the precipitation averaging window. In the following discussion, we use "ARM" to refer to the data directly from ARM individual instruments, which are often at much higher temporal frequencies and applied less data quality controls than the ARMBE product.

2.3 Convective Transition Statistics in CWV

Figures 2.1 and 2.2 show the basic set of convective onset statistics for ensemble of CMIP6 models at the Nauru and Manus site. Schiro et al. (2016a) and Kuo et al. (2018) examined the effects of temporal averaging on the convection onset statistics, concluding that up to and including a three hour averaging window (the temporal resolution of the majority of the cohort of CMIP6 models examined here) the prominent characteristics of the pickups (Figs. 2.1a and 2.2a) are largely preserved; beyond three hours, the pickups begin to be slightly smoothed by the averaging. Observational data for Figures 2.1 and 2.2 use three hour averages, the effects of temporal averaging are shown in Figure S1 of the supplemental material.

The convective transition statistics of three observational products: TRMM Microwave Imager processed by Remote Sensing Systems algorithm v7.1 (TMI; Wentz et al. (2015)), 0.25° × 0.25° resolution , ARMBE, and ARM are compared in Figure 2.3. CWV measurements between observational products are compared in Figure S2 of the supplemental material, and overall, observational CWV measurements are consistent, with a slight low bias in TMI measurements. In ground-based observational products, ARM and ARMBE, the drop of precipitation at the highest CWV can be attributed to the wet-window problem (Kuo et al., 2018). That is, the CWV values during high precipitation events are likely missing from the record, and the gap-filling can only partially restore the missing information. Heavily raining times are thus preferentially missing, or associated with gap-filled portions of the CWV that tend to miss the very highest values, resulting in a low bias in precipitation at the highest CWV. The $\langle P \rangle$ of TMI reaches much higher precipitation rates ($\sim 6\,\mathrm{mm\,h^{-1}}$) at the highest CWV bin (Fig. 2.3). ARMBE data exhibits a $\langle P \rangle$ with nonzero values at low CWV due to its hourly average.

The probability of precipitation curves (Figs. 2.1b and 2.2b) display the most sensitivity to temporal averaging: as the temporal averaging increases, the pickup occurs at lower CWV and higher CWV values display a higher probability of precipitation. Temporal averages over

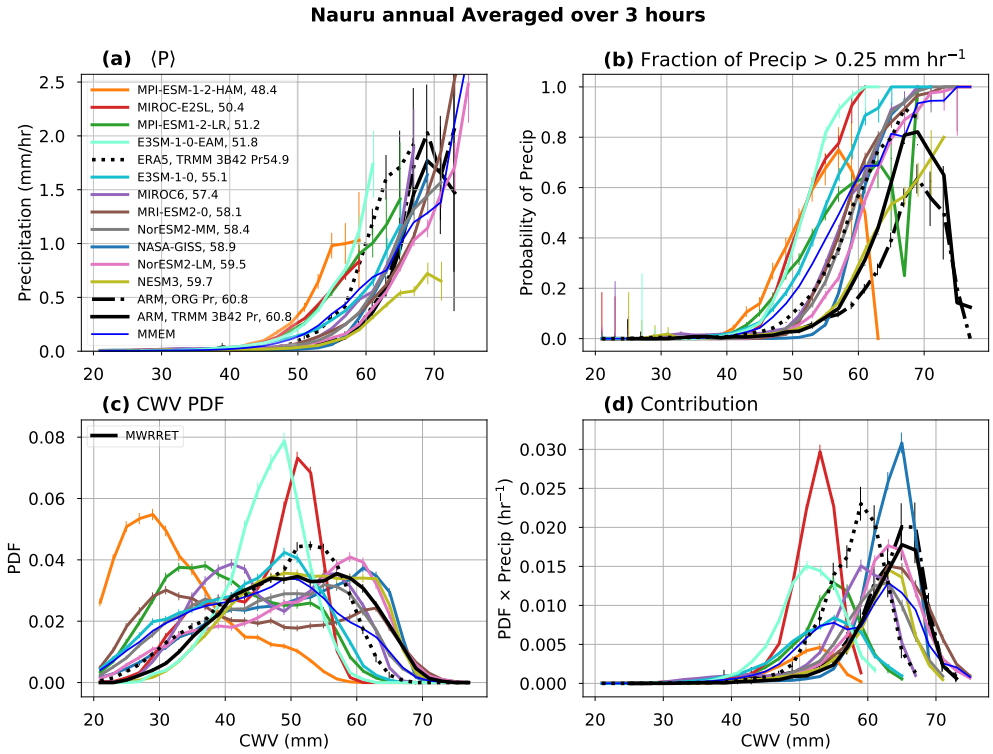

Figure 2.1: **(a)** CWV conditionally-averaged precipitation rate ($\langle P \rangle$), the critical water vapor value of the pickup, w_c, is quantified by a linear fit to $\langle P \rangle$and is listed in the legend; models are listed in ascending order according to their estimate w_c. Errorbars represent the standard error **(b)** probability of precipitation (fraction of precipitation > 0.25 mm hr^{-1} in respective CWV bin), errorbars are the Wilson Score Interval for 90% confidence **(c)** the CWV PDF, with 90% Wald Interval errorbars and (d) the precipitation contribution, or the $\langle P \rangle$-weighted PDF ($\langle P \rangle \times$CWV PDF), with errorbars that represent the error propagation of the weighting (the sum of fractional error in (a) and (c)) for ARM in-situ ORG (dash-black), TRMM-3B42 1°-spatial average precipitation (solid black), CMIP6 models (colors), and the multimodel mean (blue) for the Nauru ARM site.The observational and all model precipitation data with the exception of MPI-ESM-1-2-HAM, NorESM2-LM, and NorESM2-MM are averaged over 3 hour-windows. MPI-ESM-1-2-HAM, NorESM2-LM, and NorESM2-MM precipitation data are six hour averages. Both observational precipitation products are augmented with ARM in-situ microwave radiometer CWV. The CWV bin-width is 2 mm. Statistics are not calculated for bins with less than 10 counts.

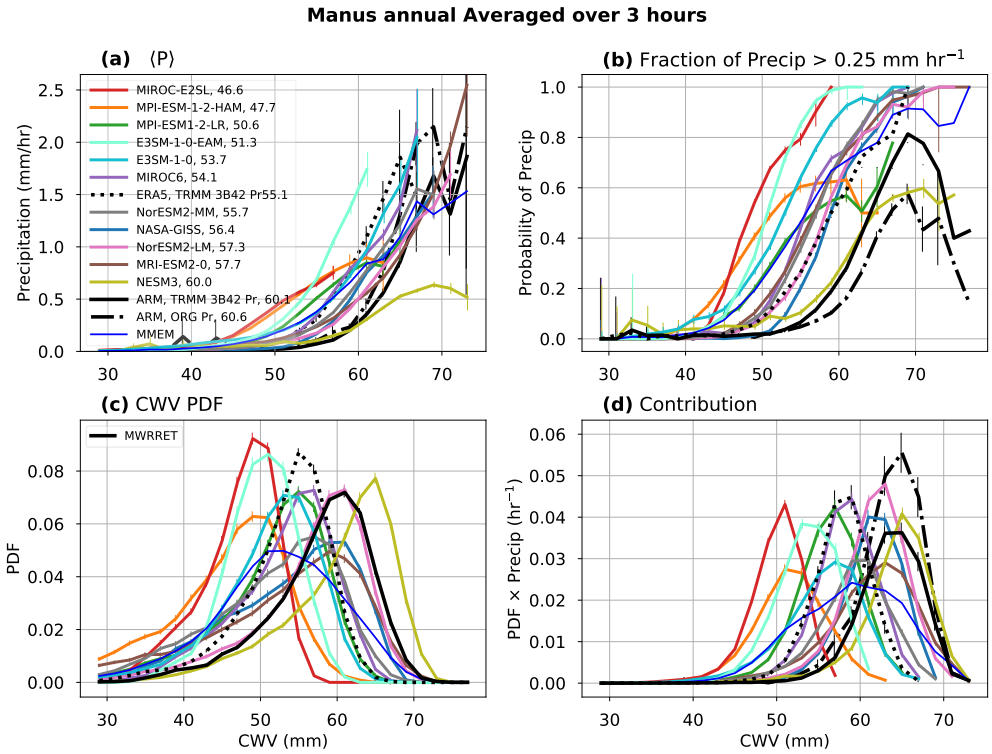

Figure 2.2: Same as Figure 1, but for the Manus Island ARM site.

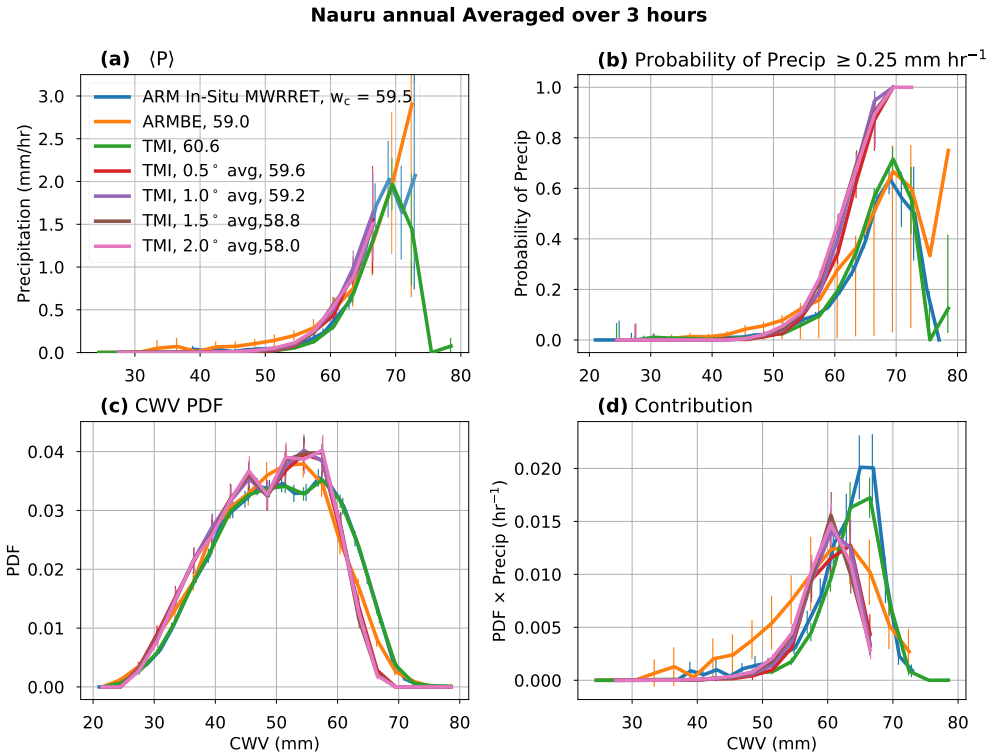

Figure 2.3: Similar to Figure 2.1 but for observational products and different spatial averages.

3 hour or greater intervals are more likely to span raining times. The wet-window problem similarly affects the observed probability at the highest CWV.

The important feature of the conditionally-averaged precipitation is the sharp, sudden increase of $\langle P \rangle$ or 'pickup' above a critical CWV value. We refer to this critical value of CWV as w_c. Previous quantitative approximations of w_c have been calculated through the CWV-axis intercept of a linear fit in a representative range of $\langle P \rangle$ (Kuo et al., 2018; Sahany et al., 2012). The range for the fit used here corresponds to consecutive monotonically increasing $\langle P \rangle$ above $0.25\,\mathrm{mm\,h^{-1}}$ and w_c is defined as the point in which the linear fit crosses a precipitation value of $0.25\,\mathrm{mm\,h^{-1}}$. Applying these conditions to approximating w_c lessens low w_c bias caused by slower increasing $\langle P \rangle$ (see NESM3 $\langle P \rangle$ in Figs. 2.1a and 2.2a for example of weakly increasing $\langle P \rangle$) and/or nonzero $\langle P \rangle$ values at low CWV caused by potential drizzle biases. Approximated w_c values are displayed in the legend of Figures 2.1 and 2.2.

An important takeaway when comparing observational products in Figure 2.3, is that the critical value of the pickup remains robust across the satellite retrieval and ARM datasets at ~ 60 mm. Although the form of the pickup remains the same, the w_c value can depend on factors that vary between land and ocean such as the mean tropospheric temperature, boundary layer dynamics and a stronger diurnal cycle over land (Schiro et al., 2016a). In evaluating model performance with the convective transition statistics, whether the model point nearest to the ARM site used in analysis is one over land or ocean could have an impact on the location of its w_c. In Figure 2.3, w_c remains robust at the Nauru sites across the ARM ground-based data and the TMI satellite retrieval. Note that only Nauru is shown here as TMI retrieval data is limited to points over oceans; the spatial extent of Nauru ($4\,\mathrm{km} \times 6\,\mathrm{km}$ (Long and McFarlane, 2012)) is small enough such that TMI records data for the site, while the $2^\circ \times 2^\circ$ data centered on Manus contains missing points. Nauru may exhibit more maritime characteristics due to its small spatial extent, but still has some island heating characteristics (Long and McFarlane, 2012), impacting boundary layer structure and

generating downwind cloud streets (Matthews et al., 2007).

The spatial dependence of the convective transition statistics were discussed in Kuo et al. (2018); the authors find $\langle P \rangle$ and the CWV PDF insensitive to the spatial resolution due to the large autocorrelation on spatial scales of moisture and temperature, while the probability of precipitation shifts slightly towards lower CWV values. Figure 2.3 shows a comparison of observational products and the effects of spatial averaging in the convective onset statistics. The spatial averages taken from boxes 0.5° to 2.0° centered on Nauru do not substantially differ from each other. The w_c of the spatial averages occur slightly earlier than that of the nonaveraged points. The probability of precipitation $\geq 0.25\,\mathrm{mm\,h^{-1}}$ occurs earlier for spatial averages, and increases at a slightly faster rate, particularly at lower CWV values where the probability transitions from nonzero values.

The robustness of $\langle P \rangle$ over different spatial scales up to 2°-box is due to the large spatial autocorrelation of CWV. The TMI curve (green) in Figure 2.3 includes all points within a 1° box centered on Nauru; compared to the 1° average in the plot (purple), the pickup is slightly later and CWV PDF extends to higher values, suggesting that the spatial average reduces the probability of high CWV values.

The characteristic shape of the CWV PDFs of the observations features a gradual increase at a low CWV towards a broad peak which drops off rapidly around w_c and is determined by the large-scale flow interacting with convective physics (Kuo et al., 2020). The CWV PDF is limited on the left by the large-scale flow—regions dominated by ascent (descent) spend more time at higher (lower) CWV—and the right by precipitation. The sharp decrease in the CWV PDF at higher $\langle P \rangle$ is consistent with precipitation becoming an effective moisture sink as the CWV reaches w_c (Schiro et al., 2016a). The aforementioned wet-window could also affect the highest portion of the CWV PDF, reducing the frequency at which high CWV values are recorded by the radiometer during strong precipitation. In comparing observational products, (satellite to ground-based measurements, Figure 2.3) the most notable differences in the statistics are the characteristics of the CWV PDFs. At both sites, the CWV PDFs

of TMI data rise and peak at lower CWV values and dropoff before the in-situ radiometer data. It is likely this low bias in the TMI data stems from the retrieval algorithms of the instruments, as the bias is noticeable in the scatter plots of the CWV from the ARM in-situ and TMI (Fig. S2). However, the start of the CWV PDF dropoff is robust between the two datasets, differing in the rate at which the PDF begins drop.

In general, models tend to have an early pickup. Around half of the models: NASA-GISS, NorESM2-LM, NorESM2-MM, MIROC6, and E3SM-1-0-EAM reach similar $\langle P \rangle$ at their highest CWV bin to observations at both sites. MRI-ESM2-0 precipitates at a higher rate ($\sim 3\,\mathrm{mm\,h^{-1}}$) at both sites, picking up earlier yet increasing its $\langle P \rangle$ at a slower rate. MPI-ESM-1-2-HAM, MIROC-ES2L, and NESM3 show low maximum rates of $\langle P \rangle$at both sites. The approximated w_c for some models (MIROC6, MRI-ESM2-0, NorESM models, and NESM3) models are within a range of $\sim$3 mm to observations at both sites; the difference in the approximated w_c in these models stems from the rate at which their $\langle P \rangle$ increases. MPI-ESM-1-2-HAM, NorESM2-LM, and NorESM2-MM precipitation data are six-hour time averages. As discussed in the beginning of this section, a six-hour temporal averaging window slightly smooths the pickup in $\langle P \rangle$ and reduces the precipitation rate only slightly; although NorESM2-LM and NorESM2-MM $\langle P \rangle$ curves agree fairly well with observations.

Respective model performance of $\langle P \rangle$ remains relatively consistent in magnitude, slope, and w_c of $\langle P \rangle$ across the two sites. Model pickup tends to be too weak with increasing CWV at both sites. NASA-GISS, MIROC6, and E3SM-1-0-EAM pickup at a rate similar to that of observations at Nauru, while only E3SM-1-0-EAM replicates the pickup slope at Manus. One known factor that can contribute to an early pickup (i.e., at low CWV) is insufficient effect of lower free tropospheric moisture on buoyancy through entrainment (Holloway and Neelin, 2009a; Kuo et al., 2017; Schiro and Neelin, 2019). It is also plausible that the early pickup in models could be associated with the pervasive model drizzle problem (Chen and Dai, 2019; Jing et al., 2017; Rushley et al., 2018; Stephens et al., 2010), suggesting that the lack of sufficiently strong dependence on the moisture environment yields models that precipitate

too frequently at low intensities. In addition, the unrealistically strong coupling of convection with surface heating, as assumed in many convection parameterizations, may also lead model convection to be triggered too easily (Xie et al., 2019).

Figures 2.1b and 2.2b show the fraction of precipitation over a threshold, $0.25\,\mathrm{mm\,h^{-1}}$, in each CWV bin. The errorbars represent the Wilson Score 95% confidence interval for each bin. In comparison to observations, the fraction above the threshold increases at a similar rate to the ORG precipitation set of observations at Nauru, and slightly faster than the TRMM-3B42 precipitation set with increasing CWV. At Manus, the majority of models increase slightly faster than both observational precipitation datasets. We note that the probability of precipitation (Figs. 2.1b, 2.2b) is more sensitive to averaging than $\langle P \rangle$, both to temporal averaging as previously discussed, and to spatial averaging, as observed when comparing the higher precipitation fraction of the TRMM 3B42 curve (averaged over 1°) in comparison to the in-situ ORG curve. Nonetheless there is high consistency between the probability measure of the pickup and the conditional average measure—models that pickup early in one also do so in the other.

Differences in the observational CWV PDFs between the Nauru and Manus site are easily observed in terms of their shapes. Nauru exhibits a broad peak from ∼40 mm to ∼60 mm, while Manus shows a more narrow peak from ∼55 mm to ∼65 mm. This reflects the large-scale flow around each site. The Manus site is located at the heart of the western Pacific warm pool and exhibits a more pronounced ascent climatology compared to the Nauru site, which is located on the edge of the western Pacific warm pool (Xie et al., 2010). Nauru experiences both the upwelling and downwelling portions of the Walker Circulation (Long and McFarlane, 2012).

At the Nauru site, most models exhibit more complicated CWV PDFs than the observations. MPI-ESM-1-2-HAM has a strong peak towards lower CWV, with a long trailing tail to higher CWV at the right. Generally, models exhibit either a broad peak or bimodal distribution at Nauru (Fig. 2.1c). The more complicated PDF shapes observed in models

could possibly be attributed to climatological biases. The Nauru site's location on the edge of the western Pacific warm pool is associated with a weaker ascent regime compared to the Manus site, leading to more time spent at lower CWV. The location of the sites in the tropical western pacific would suggest likely effects of ENSO related forcing on vertical motion. The peak at lower CWV can be attributed to the balance between surface evaporation and moisture divergence (Kuo et al., 2018). E3SM-1-0-EAM and MIROC-E2SL show a prominent peak and narrow range of CWV, with a steep and early dropoff around their w_c for both Nauru and Manus (Figs. 2.1c and 2.2c). In the above discussion of w_c's relation to the CWV PDF and the peaks of the contribution, models that pickup early (late) in general have CWV PDFs and contribution peaks shifted towards lower (higher) CWV (Figs. 2.1c and 2.2c).

Overall, the models replicate the characteristic shape of the CWV PDF at the Manus site, implying that the models are able to capture the ascent regime of the large scale flow at Manus. NorESM2-LM almost replicates the observed PDF exactly. The widths of the CWV PDF peaks are appropriate for the majority of models at Manus. Peaks of the CWV PDF for MRI-ESM2-0, Nor-ESM2-MM, NASA-GISS rise too slow and these models have fatter tails to the left of their peaks. Models peak at lower CWV than in observations, consistent with the location of their w_c. Although NESM3's w_c is the closest to observations, its PDF peaks at a higher CWV. It is possible that the weaker pickup of this model allows the column to stay at higher CWV as precipitation is not as effective of a moisture sink as in other models. This calls for an additional consideration in the relationship between the pickup and CWV PDF. Typically, the CWV PDF is characterized by an abrupt drop on the right at higher CWV around values in the range of the pickup; the sudden drop is consistent with precipitation's dissipative effects of water vapor and buoyancy (Schiro et al., 2016a).The slope of $\langle P \rangle$ reflects the behavior of a convective event in which the high precipitation rate cannot be sustained as CWV and buoyancy are consumed, and the precipitation rate starts to diminish. All models capture the prominent peak in the CWV PDF at Manus (Fig. 2.2c) and for the most part have CWV PDF dropoff rates similar to observations, yet have more

shallow $\langle P \rangle$ rates of increase.

Distributions of precipitation contributions give how much of the total amount of precipitation comes from a given range of water vapor values (units are h^{-1} from the precipitation units $\mathrm{mm/h}^{-1}$ and the PDF units of mm^{-1} giving the occurrences per interval of water vapor). These are useful because they capture the combination of two effects: the sharp increase of conditionally averaged precipitation at w_c and the rapid drop in the frequency of occurrence above w_c. These provide similar information as the PDFs of precipitating points (the PDF of time spent at a CWV and precipitating greater than $0.25\,\mathrm{mm\,h}^{-1}$; not shown here) but without the need of setting a threshold.

The contribution peaks are generally wider than those of the observations. Contribution peaks for the models with the appropriate w_c to observations at Nauru, NESM3 and NorESM2-LM, show early peaks in their contribution. All models behave appropriately in their characteristics of CWV PDFs and precipitation contributions respective of their w_c: rapid dropoff of the CWV PDF in the range of high $\langle P \rangle$ and precipitation contribution peaks in a narrow range after w_c.

We note significant difference between the ERA5 reanalysis and the ARM CWV at both sites. The ERA5 w_c occurs at a lower value than the ARM data at both sites, resulting in a low-CWV environment bias (Figs. 2.1 and 2.2). A significant contributor to this is likely temperature bias, as discussed in section 2.5. Figure 2.3 illustrates that significant differences in $\langle P \rangle$ and the CWV PDFs are not readily attributable to those which arise from varying spatial-averaging domains and in-situ measurements.

2.4 Temperature Dependence

In evaluating the models, biases of the large-scale environment should be taken into account before definitive conclusions of the efficacy of model's convective-precipitation related processes are reached. The temperature dependence of the convection onset statistics is inferred from

column saturation: higher average column temperature requires higher CWV to reach saturation which shifts w_c towards higher CWV. The threshold w_c is dependent on the temperature through the convecting layer, sometimes parameterized as a fixed value of its saturation in models (e.g. Betts and Miller (1986) scheme). Models that exhibit a cold bias in daily temperatures should therefore reach column saturation at lower CWV and pick up earlier (lower w_c). A traditional way to account for a temperature bias would be to examine convection onset statistics in column relative humidity (CRH (%) $\equiv$ (CWV / $\widehat{q_{sat}}$)$\times$100), where CRH is calculated with its instantaneous CWV and $\widehat{q_{sat}}$ values (Bretherton et al., 2004; Wolding et al., 2020).

The convection onset statistics for observations (1°-averaged TRMM-3B42 precipitation) and three representative models—the rest of the models are shown in the Supplementary Information (Figs. S5 and S6)—conditioned on $\widehat{q_{sat}}$ are shown in Nauru (Fig. 2.S8) and Manus (Fig. 2.5). The same data in the CWV domain is shown in the supplemental material Figure S3 and S4. The models shown here were chosen to give a survey of various model biases with respect to observations: MRI-ESM2-0 picks up at a slow rate with a w_c within 3 mm of observations and reaches a higher rate of precipitation in its highest CWV bin, NESM3 exhibits the slowest pickup and its CWV PDF drops off at higher CWV than observations, E3SM-1-0 picks up at a rate similar to that of observations, yet much earlier than observations. For observational statistics conditioned on ARMBE derived $\widehat{q_{sat}}$, the temperature dependence discussed above is observed as $\widehat{q_{sat}}$-binned pickup curves and PDFs collapse to a nearly single CRH value. An additional measure of $\widehat{q_{sat}}$ for observations is calculated from one-hourly 0.25° European Center for Medium-Range Weather Forecasts ERA5 atmospheric temperature reanalysis (Hersbach et al., 2020) for the years 2002-2014. Results using ERA5 $\widehat{q_{sat}}$ are displayed in Figures S5d,e,f and S6d,e,f.

In general, models exhibit some degree of temperature dependence, the two exceptions being the MPI models (shown in supplemental material panels m, n, o, p, q and r Figures S5, S6). Models are consistent in showing temperature dependence across the Nauru and

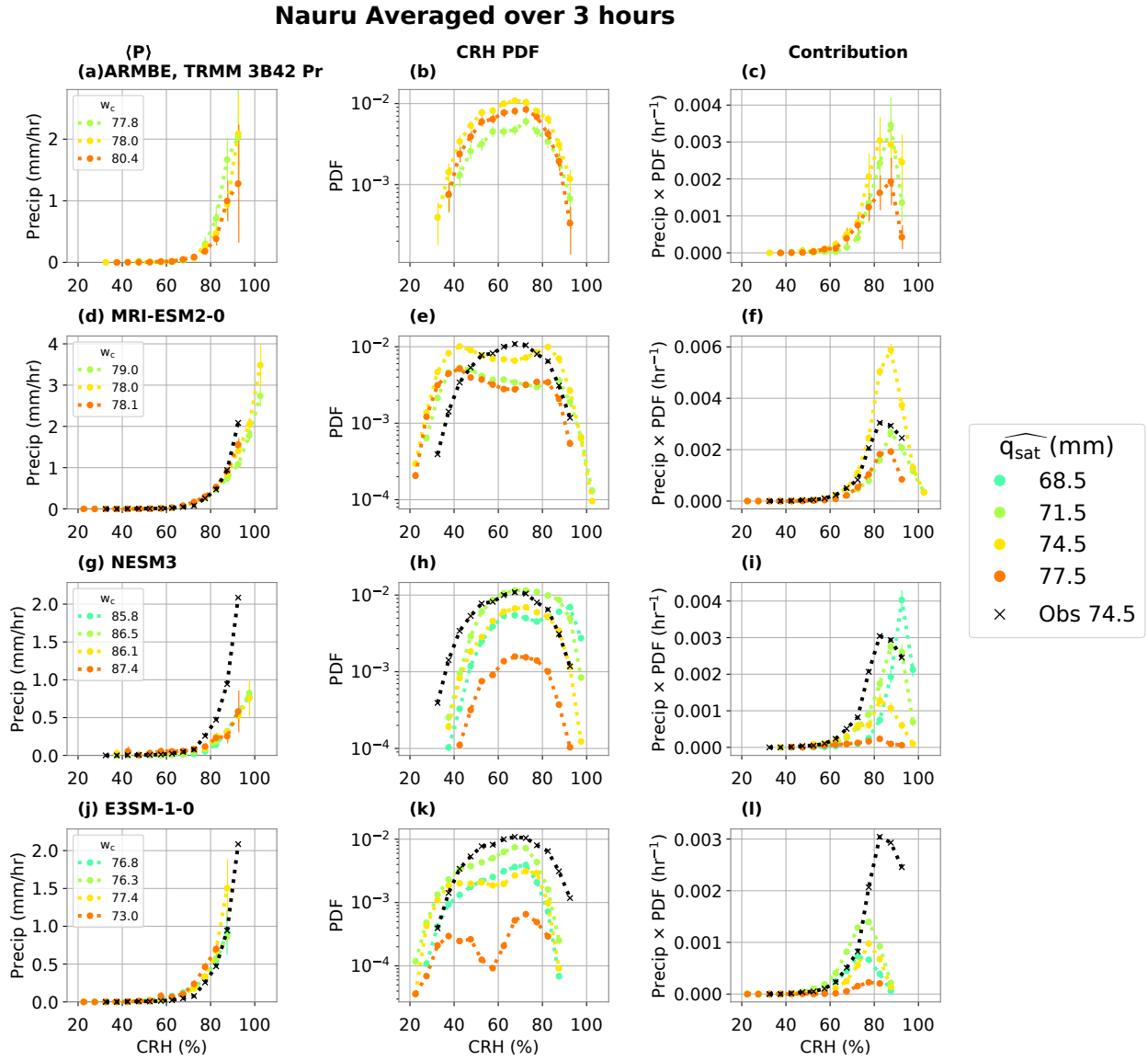

Figure 2.4: **(a)** $\langle P \rangle$ conditioned on $\widehat{q_{sat}}$, errorbars represent the standard error with the w_c for each respective $\langle P \rangle$ listed in the legend and **(b)** the CRH PDF conditioned on $\widehat{q_{sat}}$with 90% Wald Interval errorbars and **(c)** the precipitation contribution for each $\widehat{q_{sat}}$bin $\langle P \rangle$-weighted PDF with errorbars that represent the error propagation of the weighting (the fractional sum of error of (a) and (b)) for each $\widehat{q_{sat}}$bin for Nauru. The top panel is the ARMBE CRH with TRMM 3B42 precipitation averaged over 1° centered on the nearest spatial point. Three representative models are shown, all with w_c within a close range to that of the observations. The most populated $\widehat{q_{sat}}$ bin for observations (74.5 mm) statistics are overlaid on the model (black x). Statistics are not calculated for bins with less than 10 counts.

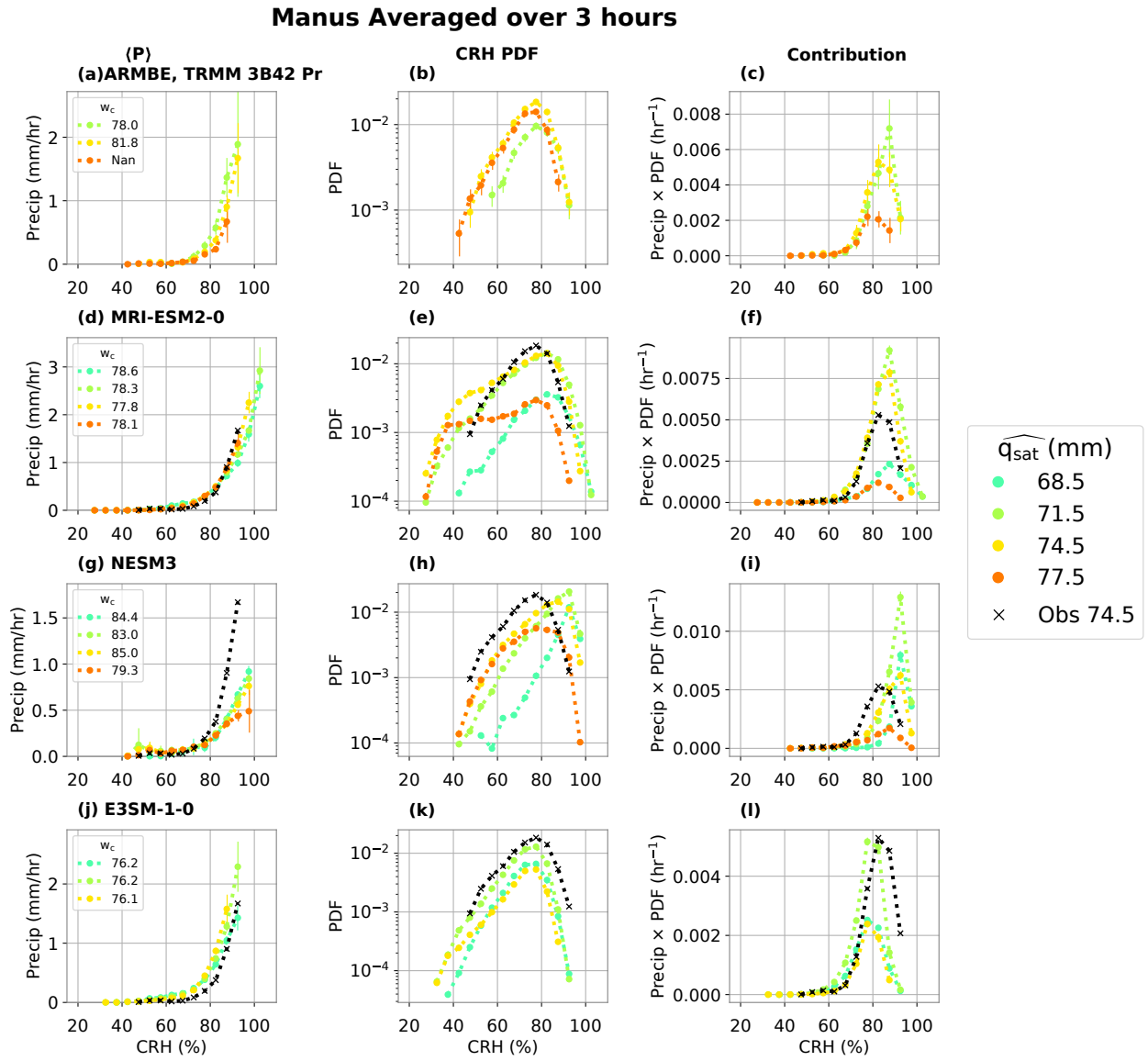

Figure 2.5: Similar to Figure 2.S8, but for the Manus site. A w_c value of Nan in the legend indicates that $\langle P \rangle$ does not contain an adequate number of points in the precipitation rate range for estimation.

Manus sites. The $\widehat{q_{sat}}$ value with the largest contribution (Figs 2.S8 and 2.5) depends on large-scale conditions in the frequency of temperature, as the magnitude of $\widehat{q_{sat}}$-conditioned $\langle P \rangle$ at saturation does not display a discernible dependence on $\widehat{q_{sat}}$.

Basinwide convective transition statistics are consistent when conditioned on ERA5 and NCEP2 Reanalyses $\widehat{q_{sat}}$ (not shown). The $\widehat{q_{sat}}$ PDF for the ARMBE, NCEP Reanalysis 2 and the ERA5 reanalysis products and models is shown in Figure 2.6. A cold bias is seen in the NCEP Reanalysis 2 $\widehat{q_{sat}}$ compared to ERA5 especially for Manus. ARMBE $\widehat{q_{sat}}$ is significantly warmer than both reanalysis products and the majority of models. The statistics for column variables of the ARMBE were compared to radiosonde measurements (Stokes and Schwartz, 1994) and were found to be nearly identical (not shown).

A noticeable feature of the model comparisons in Figure 2.6 is the $\widehat{q_{sat}}$ bias apparent in each model. In comparing the thermodynamic environment of models, NASA-GISS, MIROC-E2SL and MPI-ESM-1-2-HAM have a strong cold bias (peaks $\sim$ 5 mm low of ERA5), MRI-ESM2-0 is the only model with a large warm bias (peaks $\sim$3 mm high) at both sites while the other models seem to crowd around the ERA5 $\widehat{q_{sat}}$ peak, mostly at a slightly higher (within $\sim$ 1 mm) $\widehat{q_{sat}}$.

The observations and reanalysis products conditioned using $\widehat{q_{sat}}$ collapse to a nearly single critical CRH at the sites. In ARMBE and models, the collapse is not perfect, owing to the more nuanced relationship of convective onset to plume buoyancy and its associated factors: boundary layer moisture and temperature relative to the lower free troposphere (LFT), and subsaturation of the LFT (Adames et al., 2021; Ahmed and Neelin, 2018b). Models are consistent in their temperature dependence in the pickup conditioned on $\widehat{q_{sat}}$ across sites (Figs. 2.S8, 2.5).

The characteristics shapes of the $\widehat{q_{sat}}$-binned CRH PDFs in Figures 2.S8 and 2.5 panels b,e,h, and k are similar to the CWV PDFs (Figs. 2.1c, and 2.2c) discussed earlier—a peak at low CRH with a sharp decrease towards lower CRH and a slow increase to the right, peaking again around w_c, and dropping off sharply. The point at which the PDF (2.S8 and

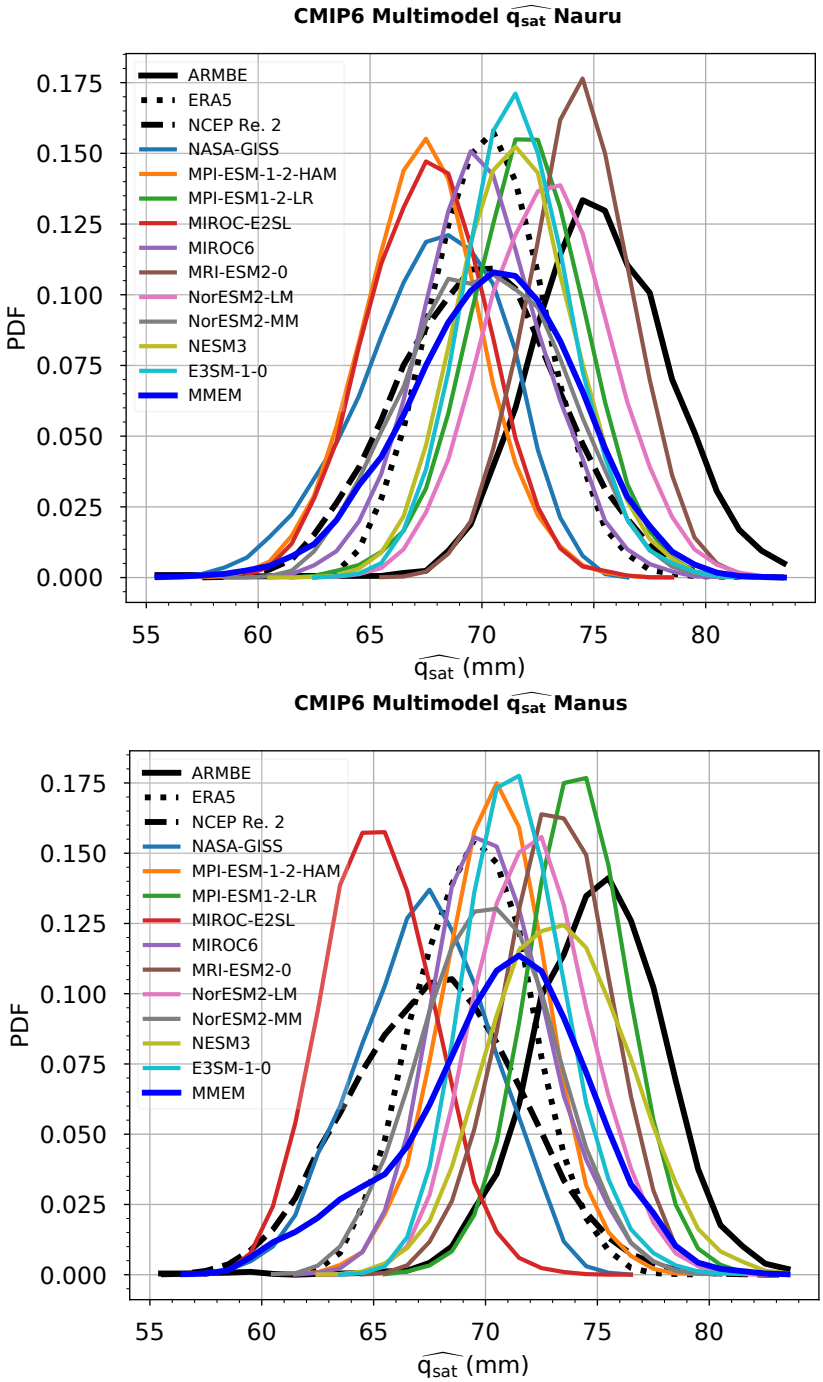

Figure 2.6: The $\widehat{q_{sat}}$ PDF for (top) Nauru and (bottom) Manus of observations and reanalysis products and models.

2.5 panels b, e, h, and k) begins to decrease rapidly is referred to as the dropoff. It occurs above w_c in the range where convection and the moisture sink associated with precipitation tend to oppose increases of buoyancy and CWV, respectively. The highest $\widehat{q_{sat}}$-bin PDF seems to spend more time at lower CRH and drops off before the other bins. The probability shifting to lower CRH values as $\widehat{q_{sat}}$ increases is expected, as reaching higher values of CRH at higher $\widehat{q_{sat}}$ requires more moisture. However, the inconsistency of the CRH value of the dropoffs across the $\widehat{q_{sat}}$ bins presents a caveat in using CRH in the statistics. CRH tends to overcompensate for temperature dependence as the location of the dropoff of the PDFs in CWV does not increase as fast with temperature as $\widehat{q_{sat}}$ (Kuo et al., 2020; Neelin et al., 2009). This results in the failure of normalization by $\widehat{q_{sat}}$ to completely collapse the statistics in Figs. 2.S8 and 2.5 panels b, e, h, and k. In other words, CRH puts too much emphasis on saturation; other considerations with respect to temperature affect the dropoffs of the $\widehat{q_{sat}}$-binned PDFs. For convective precipitation, criteria for conditional instability have a more complex dependence on temperature than simply saturation, so it is unsurprising that temperature biases are not completely resolved when using CRH.

2.5 Convective Transition Statistics in CRH

2.5.1 Does CRH collapse temperature dependence?

In section 4, we discuss how compiling the convection onset statistics in CRH helps account for potential model temperature biases through $\widehat{q_{sat}}$ binning. In general, model convection onset statistics display temperature dependence at both sites, $\widehat{q_{sat}}$-binned conditionally averaged precipitation in CRH collapse to a single critical CRH, CRH PDFs drop off at a similar CRH—also replicate the 'overcompensation' behavior of the higher $\widehat{q_{sat}}$ bins noted in the observations—and contributions peak around a similar CRH. The early pickups of the models in CWV are suggestive of a cold bias. In Figure 2.6 we note a large spread of temperature biases at Nauru compared to the ERA5 dataset: three models which show a relatively

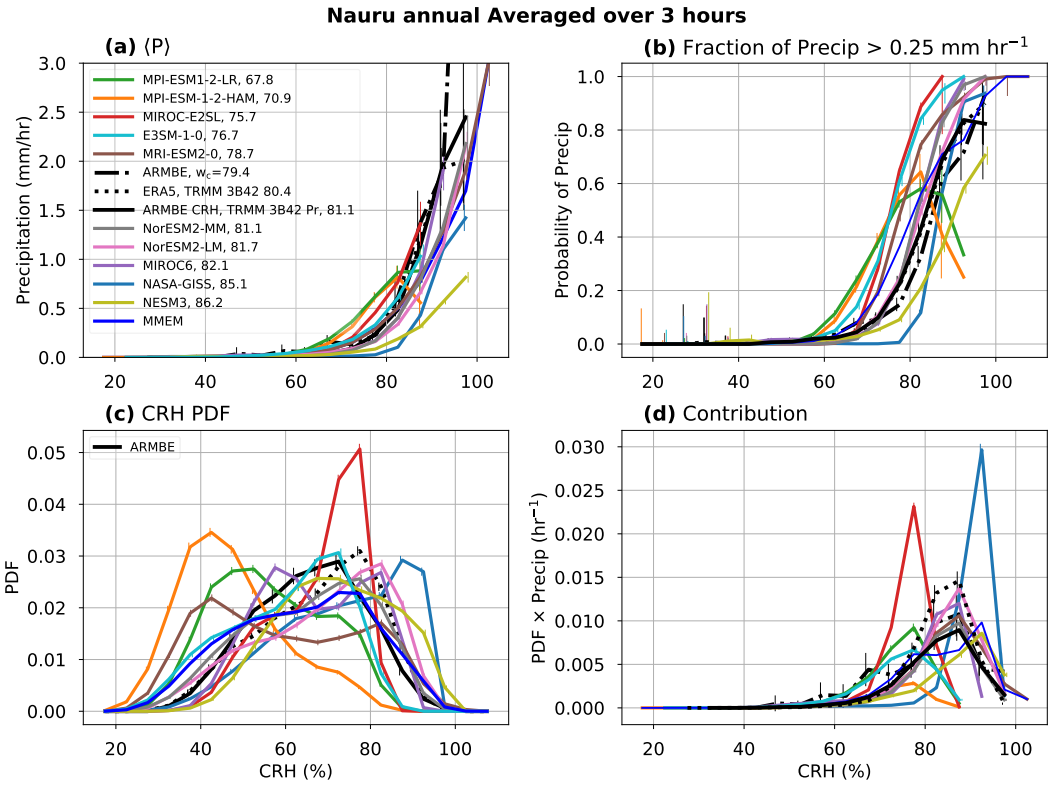

Figure 2.7: Similar to Figure 2.1, but the statistics are compiled in CRH for the Nauru site. The CRH bin-width is 5 %.

strong cold bias (NASA-GISS, MPI-ESM-1-2-HAM, MIROC-E2SL), two models with a slight cold bias (MIROC6 and NorESM2-MM), three with a slight warm bias (MPI-ESM-1-2-LR, NorESM2-LM, and NESM3), and one model with a strong warm bias (MRI-ESM2-0).

Figures 2.7 and 2.8 are similar to Figures 2.1 and 2.2, but the statistics are now compiled in CRH. The statistics for two additional ARM sites are included in the supplemental material to expand on site comparisons included in the ARM-DIAGS package: Darwin, another ARM tropical western pacific site (2° 3' 36" S, 147° 25' 30" E) and Southern Great Plains (SGP, 36° 36' 18" N, 97° 29' 6" W) in Figures S7 and S8 respectively (Gaustad and Riihimaki, 1998; Holdridge and Kyrouac, 1998; Turner et al., 2007).

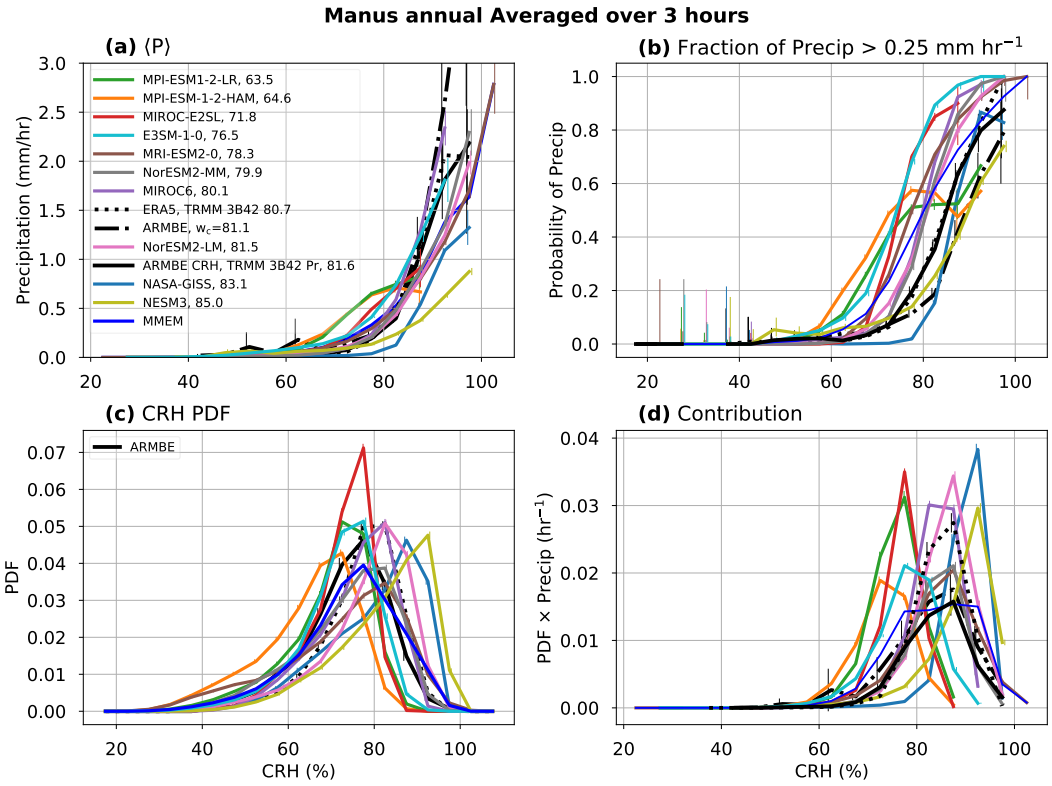

Figure 2.8: Similar to Figure 2.7, but for the Manus ARM site.

2.5.2 Basic convective onset statistics in CRH

Despite the limitations of CRH in accounting for temperature dependence (because the CRH PDFs drop off earlier for higher $\widehat{q_{sat}}$, as discussed above), it does prove useful for accounting for systematic model bias. Specifically, while the majority of models tend to pickup early relative to observations and reanalysis products in CWV, in Figures 2.7a and 2.8a, we see that accounting for temperature biases with CRH shifts model pickups so that they exhibit a spread above and below observations. The ARMBE $\widehat{q_{sat}}$ for both locations shown here (Fig. 2.6) is significantly warmer (∼5 mm) than ERA5 and the Multimodel Ensemble Mean. Accounting for the large difference in $\widehat{q_{sat}}$ by compiling the statistics in CRH shifts the pickup of the observations near the center of the model cohort at both sites. Note that despite differences in $\widehat{q_{sat}}$ between ARMBE and ERA5, the pickups in CRH agree fairly well, suggesting consistency between water vapor and $\widehat{q_{sat}}$ values within each product.

The CRH statistics are not limited to only adjusting the pickup. Similar to the CWV

PDFs shown in Section 3, the CRH PDFs of the models maintain their ability to capture the characteristic shape seen in observations at Manus, and show similar discrepancies to their CWV in their CRH distribution at the Nauru site. The smaller peak in the observational CRH PDF at Nauru is an artifact of the large scale environment effect on the CWV PDF and determined by the dry regime dynamics.

Considering the temperature dependence of CWV and the $\widehat{q_{sat}}$-binned CRH PDFs, the CRH PDFs collapse as (lower) higher CWV bins coincide with (lower) higher $\widehat{q_{sat}}$ and the dropoff of the $\widehat{q_{sat}}$-binned CRH PDFs seen in Figures 2.S8 and 2.5 panels b,e,h, and k have a dropoff located around a similar CRH in Figure 2.7c and 2.8c (e.g. just below 80% CRH in these cases). The collapsing effect of CRH is more notable at the Nauru site, the broad peak of the CWV PDF at Nauru in observations narrows into a more prominent CRH peak around its critical CRH. As discussed in section 2, the models behave appropriately in their CWV with respect to their pickup so models with temperature dependence should be able to replicate this behavior. In lower $\widehat{q_{sat}}$ bins, where overcompensation is not a problem (i.e. critical CWV increases relatively one-to-one with $\widehat{q_{sat}}$) the CRH PDF will tighten around its critical CRH. The effect to which the overcompensation has on the CRH PDFs is dependent on the value of the higher $\widehat{q_{sat}}$ bins and their frequency. With respect to both these factors, higher $\widehat{q_{sat}}$ bins only have a minor shift to the left (around a 1-2 CRH bins) and do not constitute a significant portion of the PDFs in both observations and models and may only shift some mass to the left, making the CRH PDF a little wider. A notable feature of the three models with $\widehat{q_{sat}}$ dependence is that their CRH PDFs dropoff faster than the observations, while they exhibited more appropriate dropoffs in the CWV PDF. An interesting feature of the CRH PDFs at Manus is that model PDFs which dropoff at a similar rate to observations in CWV maintain to do so in CRH, although the precipitation does not pick up in the models as fast as observations. A noticeable feature in the NASA-GISS model is the drastic dropoff close to saturation at both sites. The contribution peak of models follow the aforementioned discussion related to the CRH PDF and conditional precipitation, in that models that pickup

early tend to peak their contributions too early at all sites.

2.5.3 Decomposition into probability of precipitation and conditional intensity, $\Pr(P^+)$ and $\langle P^+ \rangle$

In our discussion of the slope of $\langle P \rangle$ in section 3, we draw comparisons between the dropoffs of the CWV PDFs in models and observations. The pickup depends strongly not only on the probability of raining times (e.g., Brown et al., 2010; Holloway and Neelin, 2010; Peters and Neelin, 2006) but also has a dependence on the sensitivity of precipitation intensity to environmental humidity during raining times (e.g., Kuo et al., 2018). A probability decomposition of the pickup such as the one performed in Igel and Biello (2019) for global precipitation, can help look at the relative contributions of these two factors. Consider a simple formulation of $\langle P \rangle$ based on the Law of Total Expectation where the sample space is partitioned in two regimes, raining (precipitation above some threshold, P^+) and nonraining (precipitation measurement below some threshold, P^-):

$$\begin{aligned} \langle P \rangle_i &= \mathbb{E}(P_i|P_i^+)\Pr(P_i^+) \\ &\quad + \mathbb{E}(P_i|P_i^-)\Pr(P_i^-) \\ \langle P \rangle_i &\approx \mathbb{E}(P_i|P_i^+)\Pr(P_i^+) \end{aligned} \tag{2.1}$$

where the subscript i is used to denote the CRH bins, Pr is the probability operator, and $\mathbb{E}$ is the expectation operator. The threshold is set to $0.25\,\mathrm{mm\,h^{-1}}$ here, consistent with the Probability of Precipitation metric (panel b in Figs. 2.1,2.2,2.7, and 2.8). Assuming that the average of precipitation values under the threshold is negligible compared to the average above, the conditional precipitation can be thought of as the product of probability of raining and the conditional mean precipitation during raining times, $\langle P^+ \rangle$, here termed conditional intensity for brevity. Figure 2.9 shows $\langle P^+ \rangle$ for the cohort.

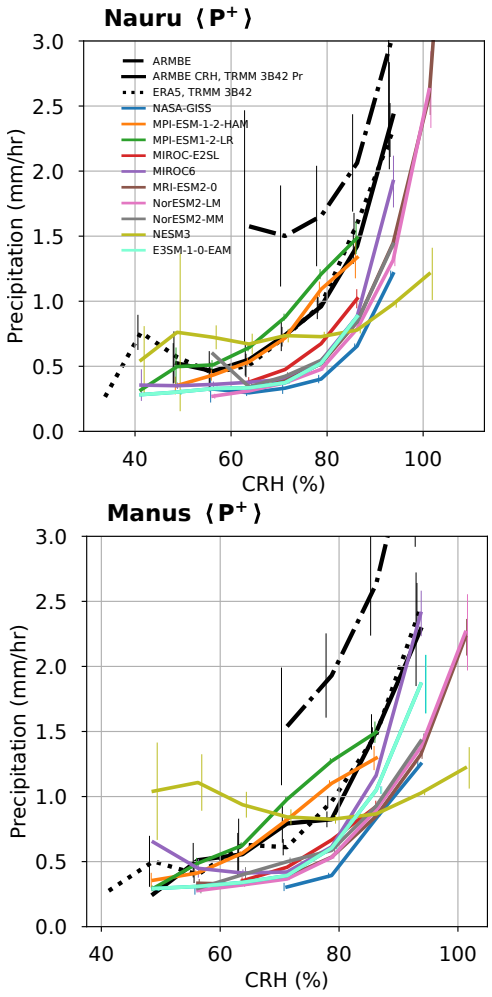

Figure 2.9: Similar to Figure 2.7a and 2.8a but the conditional average, $\langle P^+ \rangle$ is calculated over raining times only (precipitation greater than or equal to $0.25\,\mathrm{mm\,h^{-1}}$). Errorbars represent the standard error of the precipitating points.

Observations and model $\langle P^+ \rangle$, with the exception of NESM3, show sensitivity to CRH at both sites. The Probability of Precipitation (panel b in Figs. 2.7 and 2.8) and $\langle P^+ \rangle$ exhibits a sharp increase at some point in the CRH domain, suggesting that $\langle P \rangle$ is the product of two 'pickups,' $\langle P^+ \rangle$ and $\Pr(P^+)$. In ARMBE CRH and ERA5 CRH with TRMM-3b42 precipitation, $\langle P^+ \rangle$ increases sharply in the upper CRH range (black curves in Fig. 2.9). In models, with the exception of the MPI models, this occurs at even higher CRH.

This behavior may be summarized as: (i) the beginning of the $\langle P \rangle$ pickup is more dependent on increases in the Probability of Precipitation: (ii) where the probability caps out at high CRH, $\langle P^+ \rangle$ begins to govern the $\langle P \rangle$. This can be seen in Figure 2.10, which shows the decomposition of the two factors as in Equation 2.1. The logarithmic y-axis of Figure 2.10 allows the factors in Equation 2.1 to be seen additively as $\ln\langle P^+ \rangle + \ln \Pr(P^+)$ (with the caveat that a constant could be added to one and subtracted from the other). Thus the change across the CRH range of the orange and green curves in Figure 2.10 gives the relative contribution of $\langle P^+ \rangle$ and $\Pr(P^+)$, respectively. Note differences between $\ln\langle P \rangle$ and its estimation, $\ln\langle P^+ \rangle + \ln \Pr(P^+)$ are small except for at lower $\langle P \rangle$ values. In observations (Fig. 2.10a,b,c) the probability $\Pr(P^+)$ governs $\langle P \rangle$ through the early part of the increase, until $\Pr(P^+)$ flattens out, whereupon $\langle P^+ \rangle$ increases become important.

Most of the models capture this behavior at least qualitatively, with the following exceptions. The MPI models have a $\langle P^+ \rangle$ increase that is reasonable compared to observations (Figs. 2.9, 2.10e,f) but the probability $\Pr(P^+)$ picks up substantially earlier (Figs. 2.7b and 2.8b) resulting in an early pickup in $\langle P \rangle$ (Figs. 2.7a and 2.8a). NESM3's $\langle P^+ \rangle$ lies relatively flat, or shows very little sensitivity to CRH (Figs. 2.9 and 2.10l).

In neither the observational products or the models is the $\langle P \rangle$ curve well described by an exponential, perhaps not surprisingly given the competing ingredients contributing to it. The observational products show a faster-than-exponential increase (upward curvature in Fig. 2.10) in the vicinity of w_c, and a slower-than-exponential increase at very high CRH. Most of the models share this feature, with the exception of the MPI models and MRI-ESM2-0, and

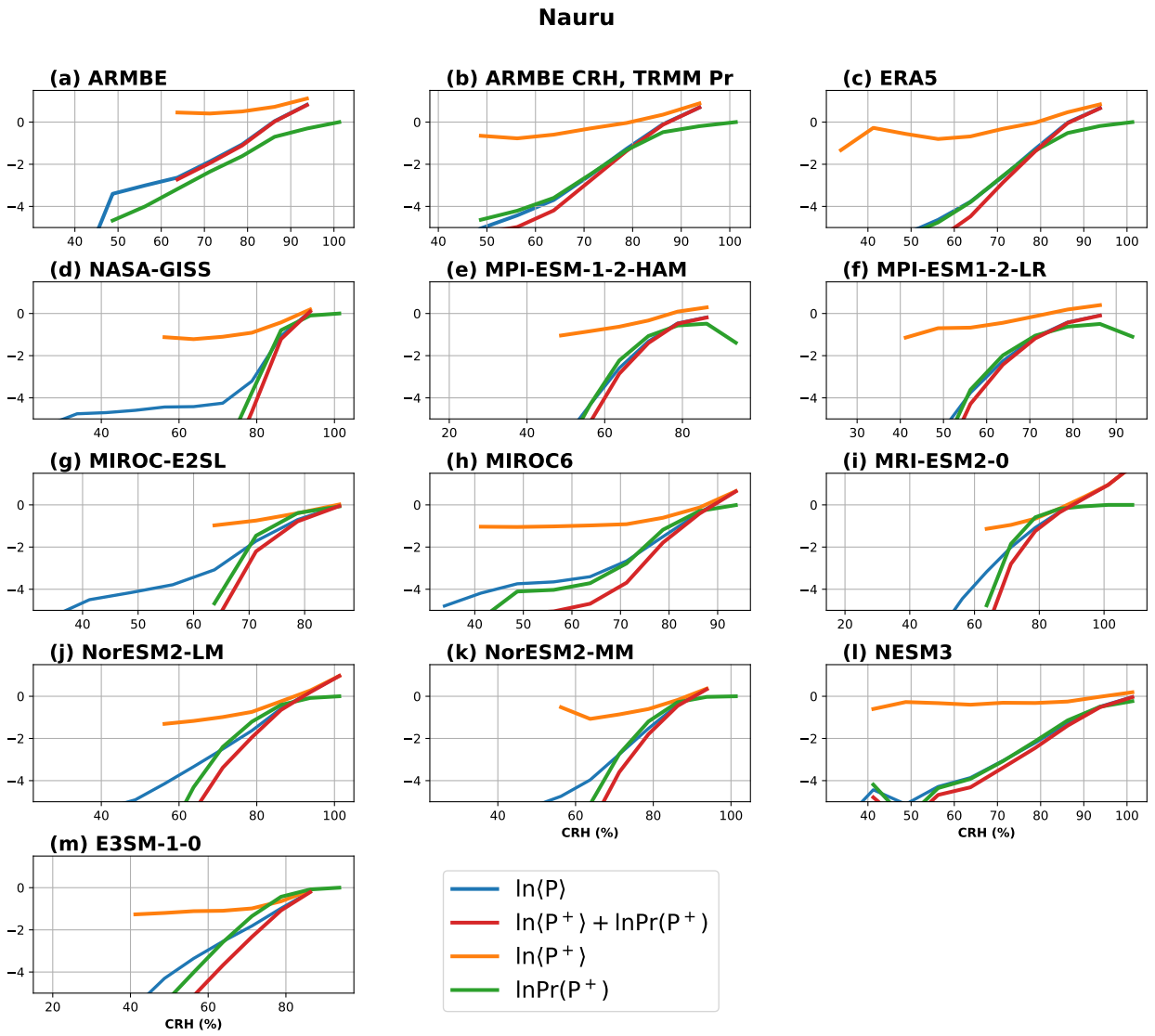

Figure 2.10: The $\langle P \rangle$ (blue), $\ln\langle P^{+} \rangle$ (orange), $\ln \Pr(P \geq 0.25)$ (green), and $\ln\langle P^{+} \rangle + \ln \Pr(P \geq 0.25)$ (red) for the cohort examined at Nauru. Note that the y-axis is in log units. The orange curve here is the same as the $\langle P^{+} \rangle$ curves shown in Figure 2.9.

with NASA-GSS exhibiting an exaggerated version.

The competing contributions of $\langle P^+ \rangle$ and $\Pr(P^+)$ may be expected to depend on spatial resolution for very fine scales. However, Figure S9 shows that for the range of spatial averaging relevant to model comparison, the observations are not sensitive to spatial scale.

With respect to averaging over raining times, the sensitivity of the precipitation threshold needs to be considered. The larger the threshold, the larger the nonraining times average precipitation is compared to raining average. The choice of $0.25\,\mathrm{mm\,h^{-1}}$ captures the sharp increase in probability of raining in panel b of Figures 2.1, 2.1, 2.7 and 2.8, while low enough such that its increase in probability remains robust when averaging over spatial scales used in models (panel b in Figure 2.3). The average over nonraining times also remains negligible compared to the average over raining times as seen in Figure 2.10.

An analysis of precipitation biases in CMIP5 models by Pathak et al. (2019) found that biases in models were more closely related to convective trigger and closure assumptions, as opposed to the cloud model employed in the GCM. A popular trigger based on convective potential energy (CAPE) where convection is activated once CAPE is above a certain threshold (often with modifications such as CAPE generation by large scale forcing (Xie and Zhang, 2000), additional relative humidity thresholds (Xie et al., 2002), diluting CAPE with entrainment assumptions (Zhang, 2009), or some combination (Suhas and Zhang, 2014)) is used in the majority of the models examined here with the exception of the NASA-GISS, the MPI models, and NESM3. NASA-GISS uses a convective trigger based on buoyancy considerations (a virtual temperature test) where convection is initiated if a parcel, lifted adiabatically, has a higher virtual temperature than the level above (DelGenio and Yao, 1993). Suhas and Zhang (2014) evaluated convective triggers and found CAPE-based triggers to be among the best performing in activating convection at appropriate times. Convective triggers for each model are listed in Table 1.

Contrasting to the above, MPI models and NESM3 use the Tiedtke (1989) scheme with modifications for deep convection by Nordeng (1994). The convective triggers for these models

have buoyancy requirements and also require net positive moisture convergence (Möbis and Stevens, 2012) since this is used in the convective closure. The buoyancy component is simply buoyant surface-level air at the lifting condensation level, which may be too easily met.

We underline that biases in w_c are not only due to biases in a model's convective trigger, but are also related to the lifecycle of a convective cloud (Wolding et al., 2020). During a precipitating event, a convective column evolves through different convective-cloud/precipitation type regimes reflected in changes to the column's moisture and/or temperature content. The pickup is therefore not so readily attributable to the onset of convection, but also may reflect a latter stage in the convective life-cycle from which moisture is consumed by precipitation, and the column shifts to a lower CRH or CWV content. The diagnostic separation into $\langle P^+ \rangle$ and $\Pr(P^+)$ here will depend on this full lifecycle and thus on both convective triggers and closures.

The models with moisture-convergent-based triggers/closures, MPI models and NESM3, show a shallower rate of $\langle P \rangle$ increase along with more nonzero values (lower probability of precipitation past pickup bin) compared to the rest of the cohort (Figs. 2.7, 2.8 panels a and b respectively). While their behavior differs in terms of $\langle P^+ \rangle$ (MPI performing well, while NESM3 is essentially flat), in their overall simulation of $\langle P \rangle$, $\langle P^+ \rangle$, and $\Pr(P^+)$ (Figs. 2.7, 2.8, 2.9, and 2.10), they tend to be outliers in terms of poor performance relative to models with buoyancy-based triggers/closures.

The w_c's of buoyancy-based trigger (CAPE triggers and NASA-GISS) models lie in a close vicinity to that of observations and the probability of raining is too high at lower and mid-range CRH values (Figs. 2.7 and 2.8 panels a and b respectively), implying that these models seem to compensate for the nearly constant values of precipitation in mid-values of CRH by raining more frequently. This is similar to the drizzle problem mentioned earlier—a consequence of models reacting too fast to surface heating and the diurnal cycle, as CAPE does not accumulate to allow for strong precipitation events (Xie et al., 2019).

Here we have focused on tying model biases in $\langle P \rangle$ to the frequency and magnitude of

precipitation—for the purpose of attributing bias to behavior during the raining ($\langle P^{+} \rangle$) or nonraining (probability of precipitation) regime. Column integrated measures do not fully elucidate the biases in the generation of CAPE and buoyancy that contribute to these biases. Event-by-event statistics, their temporal evolution, and the associated vertical thermodynamic structures are explored in a companion paper, in which a similar set of statistics in the more physically insightful buoyancy domain is used, similar to the analysis done in Ahmed and Neelin (2021a).

2.6 Conclusions and Discussion

The relationship between CWV and precipitation is observed across ARM sites and in all CMIP6 models examined here. All models exhibit some form of the observed CWV-related pickup in precipitation in which the conditional-average precipitation rate increases rapidly past some critical value of CWV, w_c. The physical relationship among statistics seen in observations is reflected in the behavior of the individual models in which w_c determines the CWV PDF dropoff. The majority of the models' convection onset statistics display some degree of temperature dependence in the CWV value of the pickup and collapse approximately to a common critical CRH value across $\widehat{q_{sat}}$ bins. However, prior results suggest that the onset of convective instability has a more complex dependence on temperature. The vertical structure of temperature and moisture, as well as the entrainment of free tropospheric air, affect the buoyancy of a rising convective plume, yielding an onset moisture-temperature dependence slightly different than that of bulk saturation (Holloway and Neelin, 2009a; Kuo et al., 2017; Schiro et al., 2018a; Wolding et al., 2020; Wolding and Maloney, 2015). Some aspect of these factors is apparently systematically different in the climate model representations than in the ARMBE data and ERA5 reanalysis. However, models are able to reproduce similar column saturation humidity PDFs to those of observations.

In section 4, we examine the temperature dependence of the convection transition statistics.

We note the problems associated with compiling the statistics in CRH, despite the hope that this common practice might reduce the effect of the temperature biases of models. Compiling the statistics in CRH helps to account for model temperature biases in bringing the critical point of model pickup closer to that of observations, shifting the cohort of model pickups so that not all models pickup earlier than observations and reanalysis. This is especially important for the case of the ERA5 reanalysis product whose cold temperature bias at the ARM sites relative to ARMBE data (shown in Fig. 2.6) accounts for the its earlier pickup in CWV (Figs. 2.1a and 2.2a) CRH PDF dropoffs remain consistent with the location of w_c. The rate of dropoff of model CRH PDFs remains similar to that of the observations for models with no temperature dependence, while models which display temperature dependence exhibited a faster rate in their CRH PDF dropoff. Further separating the conditional average precipitation into probability of precipitation, $\Pr(P^+)$ and conditional intensity (conditional precipitation in the raining regime, $\langle P^+ \rangle$) reveals that models which produce $\langle P \rangle$ similar to observations do so through compensating biases. Through this framework, the $\langle P \rangle$ behavior is characterized as being primarily dependent on the probability of precipitation near the transition and the conditional intensity at higher CRH. Models which do perform well in reproducing $\langle P \rangle$ similar to that of observations do so by initiating convection too often at lower CRH, while their $\langle P^+ \rangle$ picks up at a value later than observations. Most models exhibit low conditional intensity $\langle P^+ \rangle$ relative to observations. A few models which pick up at too low CRH values, the MPI models, are able to replicate a similar $\langle P^+ \rangle$ to that of observations, but are limited in their CRH range, and rain too frequently at low CRH. Models using descendants of the Tiedtke scheme appear to fare worse overall by these measures than models with buoyancy-based schemes. Except for NASA-GISS, models rain too frequently at low CRH regardless of the convective trigger.

Models are able to capture the characteristic shape of the CWV and CRH PDFs fairly well at the Manus site, a site dominated by the ascent regime. Models do have trouble with their PDFs at sites with seasonal variations in large-scale flow regime. At the Nauru site, the

observational PDFs of CWV have a single broad peak whereas in some models, the CWV PDF is bimodal. In general, the CMIP6 model cohort examined here: (1) pickup too early in CWV and do not increase their conditionally-averaged precipitation fast enough in both CWV and CRH; (2) associated with this, the precipitation contribution as a function of CWV or CRH peaks at too low a value; (3) the models capture the characteristic shape of CWV and CRH PDFs for sites that do not have strong variations in large-scale flow regime; and (4) exhibit behavior consistent in their CWV and CRH PDFs and peaks of contributions in relation to their critical CWV and CRH.

The ARM datasets allow for higher temporal resolution analysis. As discussed in section 3a, time-averaging up to 3 hours has little effect on the important characteristics of the statistics; we expect the higher resolution Cloud Feedback Model Intercomparison Project data for the models discussed here to remain consistent with our results once released. Higher resolution data would benefit diagnosing the large intermodel spread in regards to the various convective parametrizations on faster timescales. In a companion paper, we explore event-by-event behavior of models in the context of their associated vertical thermodynamic structures. The analysis tools and datasets presented here will be continued to be added in the ARM-DIAGS package to facilitate use of these analyses by the climate community (Zhang et al., 2020b).

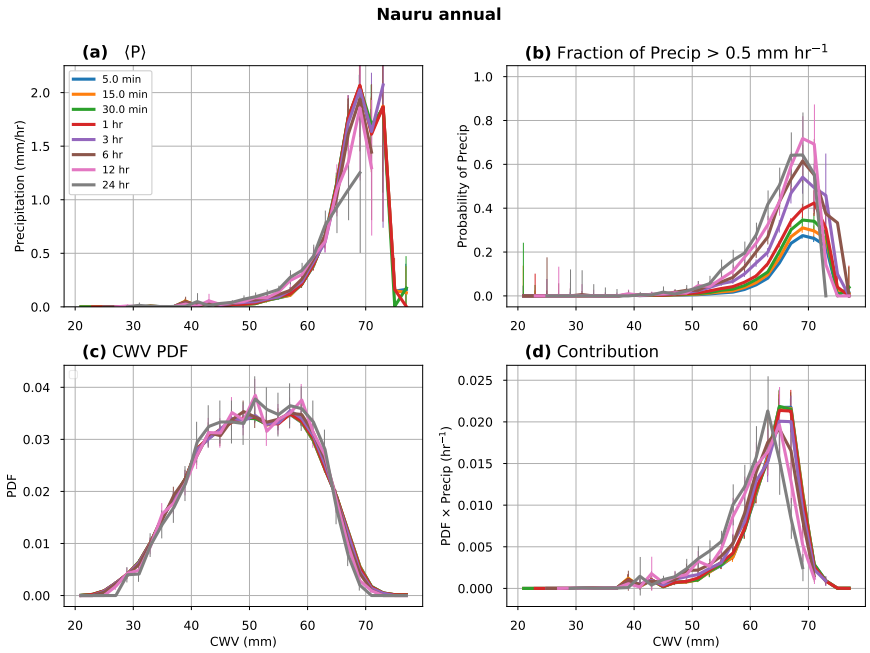

Figure 2.S1: Similar to Figures 1 and 2 of the main text, but the statistics are performed on varying time intervals: 5 minutes, 15 minutes, 30 minutes, 1 hour, 3 hours, 12 hours, and 24 hours.

2.7 Supplemental Material

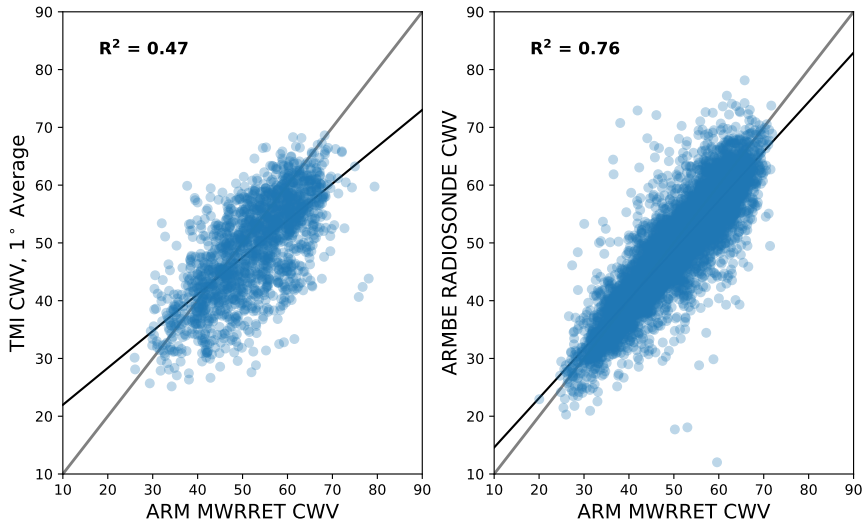

Figure 2.S2: Scatter plots of ARM MWRRET CWV to TMI 1°-averaged CWV (left) and ARMBE (right). Correlation coefficient is labeled in the plot. Gray lines are one-to-one, the black line is the regression.

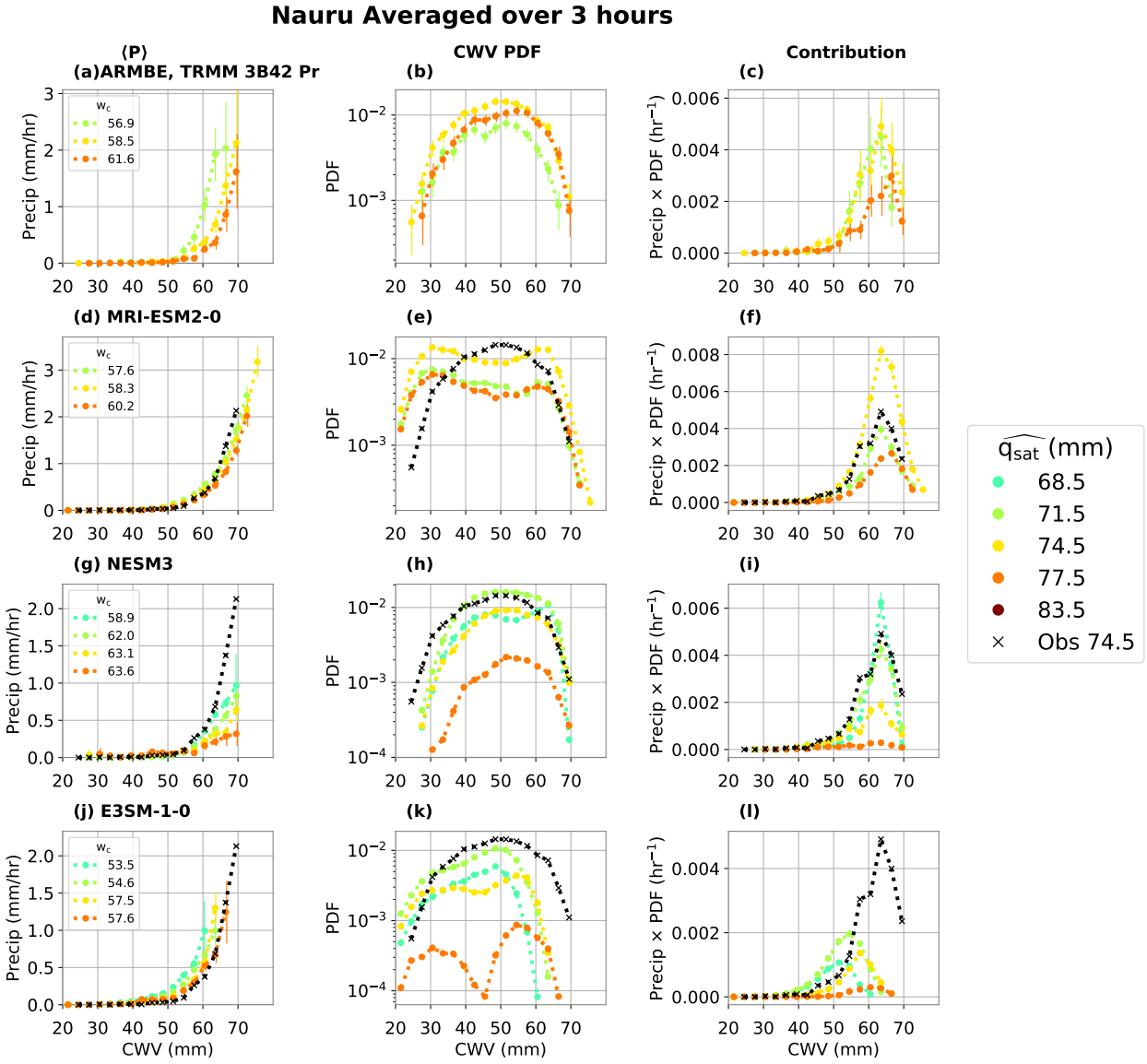
Nauru Averaged over 3 hours
⟨P⟩
(a)ARMBE, TRMM 3B42 Pr
CWV PDF
(b)
Contribution
(c)
(d) MRI-ESM2-0
(e)
(f)
(g) NESM3
(h)
(i)
(j) E3SM-1-0
(k)
(l)
Precip (mm/hr)
PDF
Precip × PDF (hr⁻¹)
CWV (mm)
w_c
56.9
58.5
61.6
57.6
58.3
60.2
58.9
62.0
63.1
63.6
53.5
54.6
57.5
57.6
q̂_sat (mm)
68.5
71.5
74.5
77.5
83.5
Obs 74.5

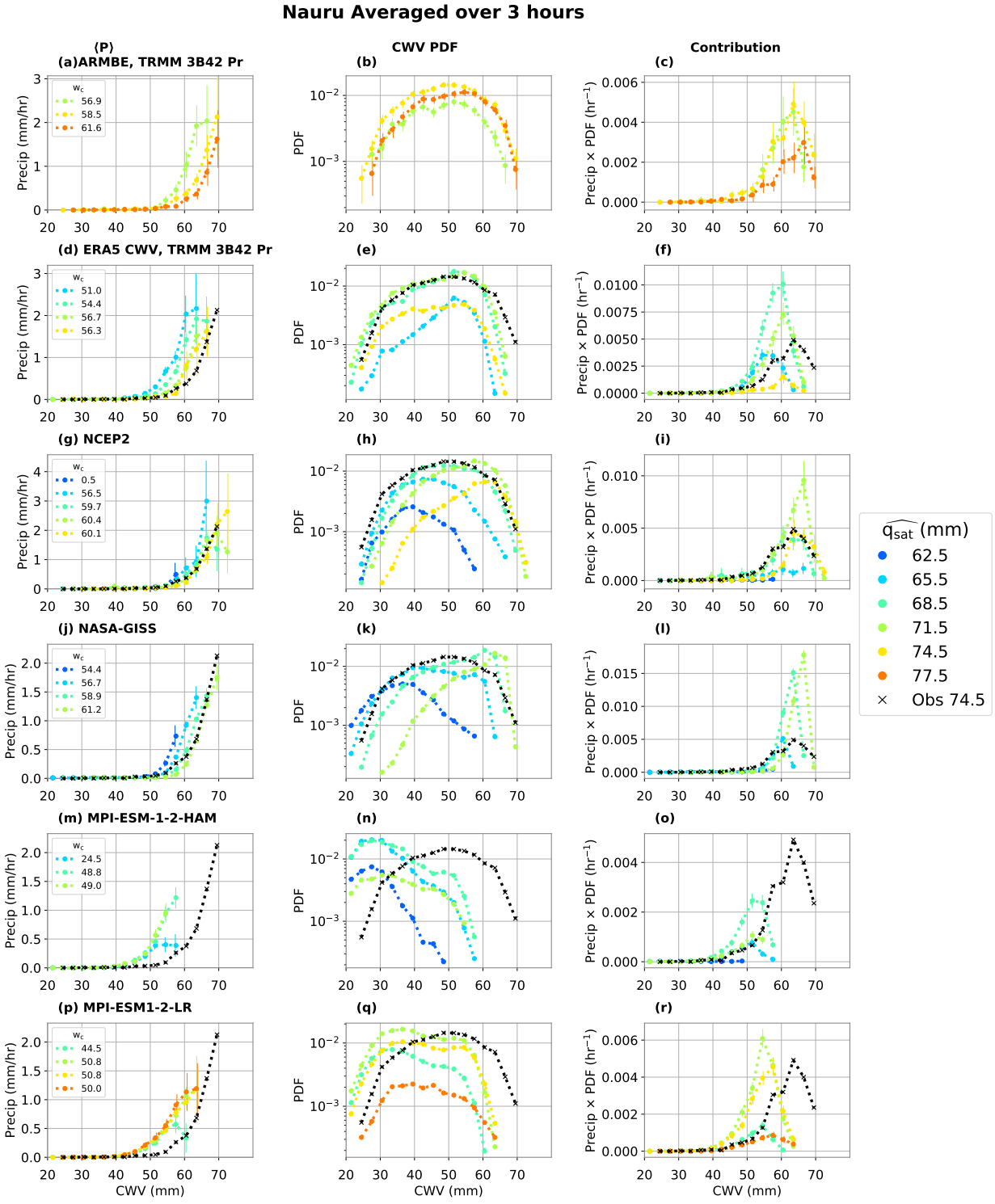
Nauru Averaged over 3 hours
⟨P⟩
CWV PDF
Contribution
(a)ARMBE, TRMM 3B42 Pr
(b)
(c)
(d) ERA5 CWV, TRMM 3B42 Pr
(e)
(f)
(g) NCEP2
(h)
(i)
(j) NASA-GISS
(k)
(l)
(m) MPI-ESM-1-2-HAM
(n)
(o)
(p) MPI-ESM1-2-LR
(q)
(r)
Precip (mm/hr)
PDF
Precip × PDF (hr⁻¹)
CWV (mm)
wc
56.9
58.5
61.6
51.0
54.4
56.7
56.3
0.5
56.5
59.7
60.4
60.1
54.4
56.7
58.9
61.2
24.5
48.8
49.0
44.5
50.8
50.8
50.0
q̂sat (mm)
62.5
65.5
68.5
71.5
74.5
77.5
Obs 74.5

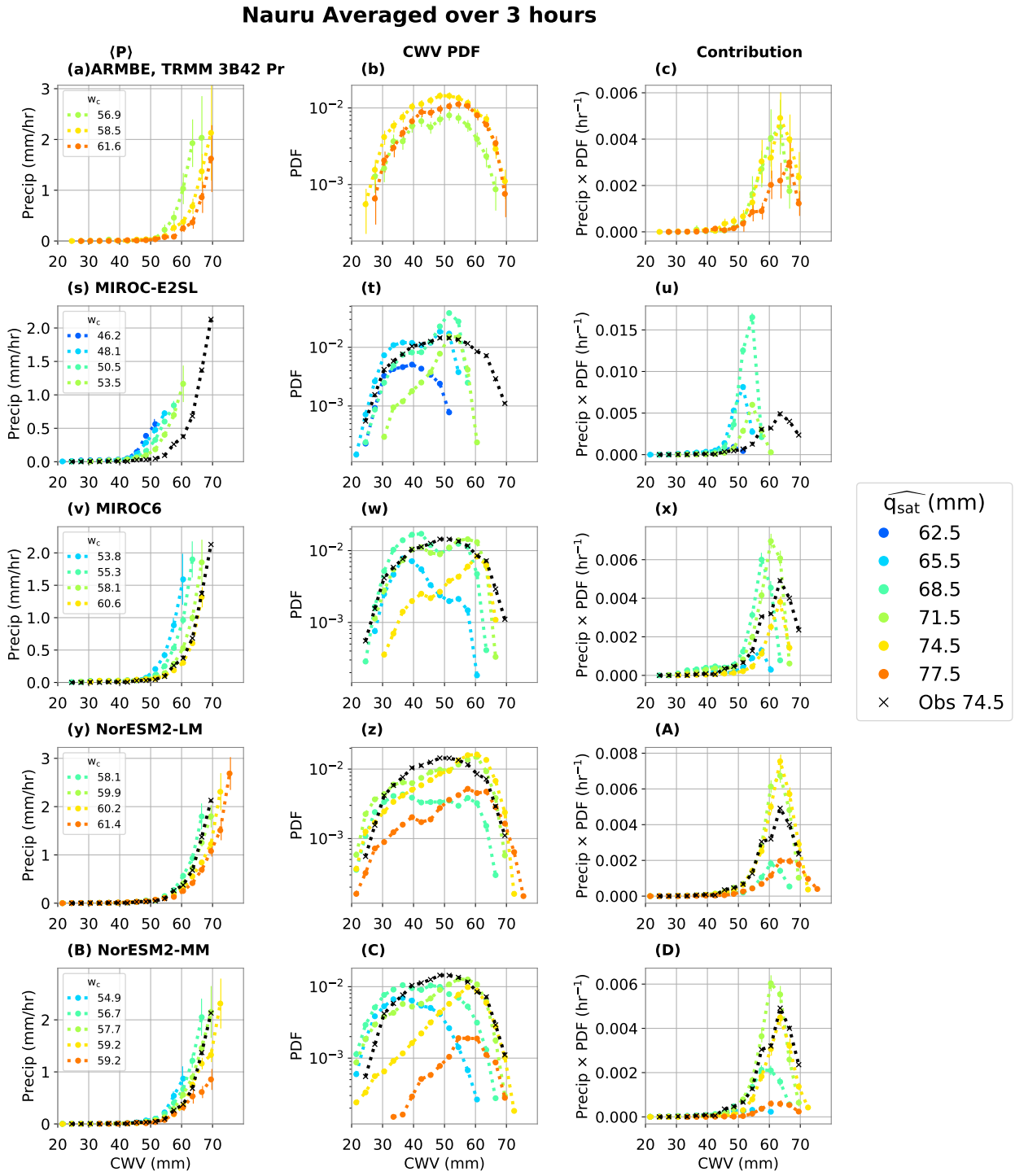

Figure 2.S3: . **(a)** $\langle P \rangle$ conditioned on $\widehat{q_{sat}}$, errorbars represent the standard error **(b)** the CWV PDF conditioned on $\widehat{q_{sat}}$ with 90% Wald Interval errorbars and **(c)** the precipitation contribution for each $\widehat{q_{sat}}$bin $\langle P \rangle$-weighted PDF with errorbars that represent the error propagation of the weighting (the fractional sum of error of (a) and (b)) for each $\widehat{q_{sat}}$bin for Nauru. The CWV bin-width is 3 mm to account for lower counts in each $\widehat{q_{sat}}$ bin and the $\widehat{q_{sat}}$ bin width is 3 mm. The top panel is the in-situ ARM microwave radiometer CWV with TRMM 3B42 precipitation averaged over 1° centered on the nearest spatial point. Three representative models are shown, all with w_c within a close range to that of the observations. The most populated $\widehat{q_{sat}}$ bin for observations (74.5 mm) statistics are overlaid on the model (black x). Statistics are not calculated for bins with less than 10 counts.

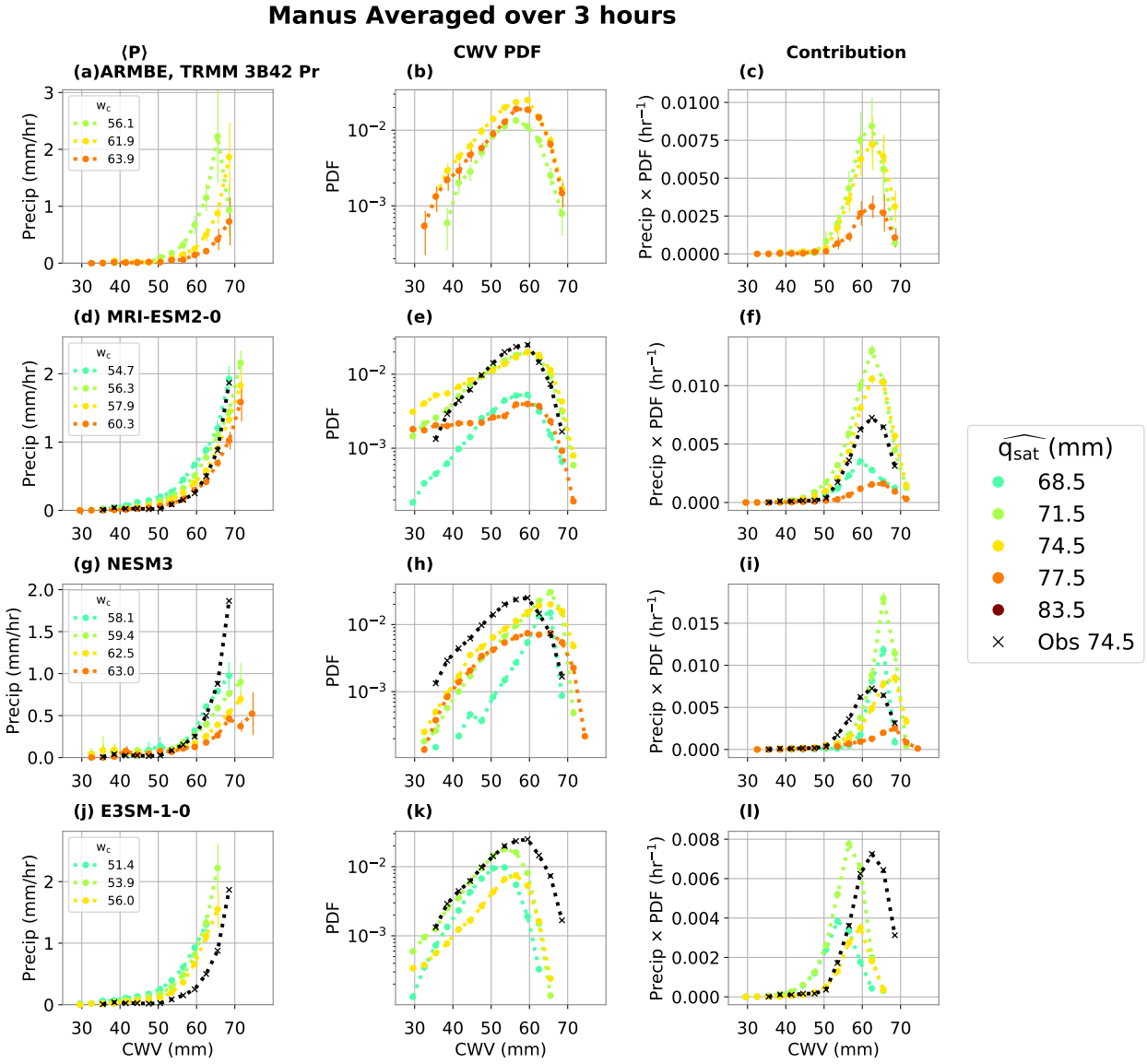
Manus Averaged over 3 hours
⟨P⟩
CWV PDF
Contribution
(a)ARMBE, TRMM 3B42 Pr
(b)
(c)
(d) MRI-ESM2-0
(e)
(f)
(g) NESM3
(h)
(i)
(j) E3SM-1-0
(k)
(l)
Precip (mm/hr)
PDF
Precip × PDF (hr⁻¹)
CWV (mm)
wc
56.1
61.9
63.9
54.7
56.3
57.9
60.3
58.1
59.4
62.5
63.0
51.4
53.9
56.0
q̂sat (mm)
68.5
71.5
74.5
77.5
83.5
Obs 74.5

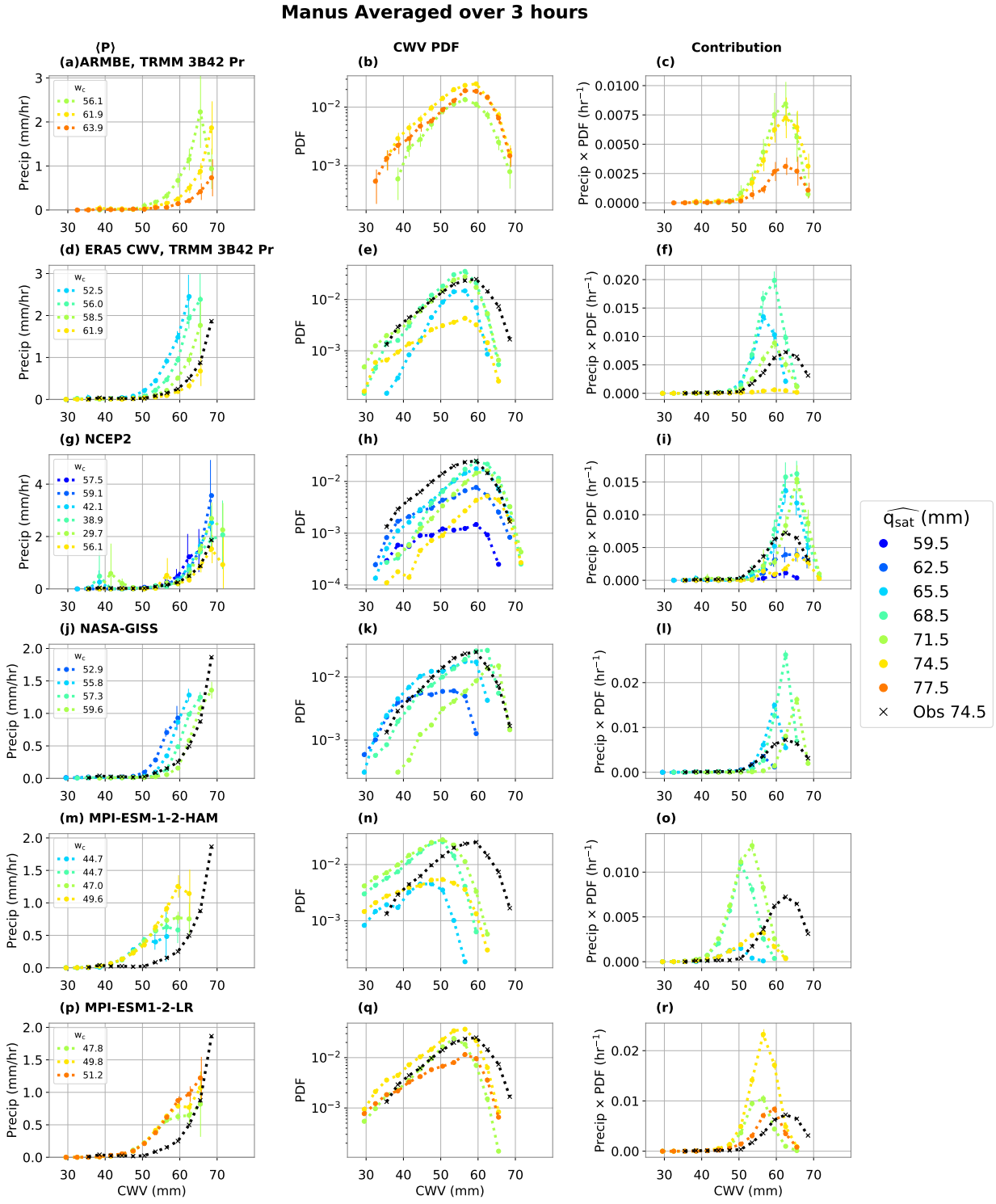
Manus Averaged over 3 hours
⟨P⟩
(a)ARMBE, TRMM 3B42 Pr
CWV PDF
(b)
Contribution
(c)
(d) ERA5 CWV, TRMM 3B42 Pr
(e)
(f)
(g) NCEP2
(h)
(i)
(j) NASA-GISS
(k)
(l)
(m) MPI-ESM-1-2-HAM
(n)
(o)
(p) MPI-ESM1-2-LR
(q)
(r)
Precip (mm/hr)
PDF
Precip × PDF (hr⁻¹)
CWV (mm)
wc
56.1
61.9
63.9
52.5
56.0
58.5
61.9
57.5
59.1
42.1
38.9
29.7
56.1
52.9
55.8
57.3
59.6
44.7
44.7
47.0
49.6
47.8
49.8
51.2
q̂sat (mm)
59.5
62.5
65.5
68.5
71.5
74.5
77.5
Obs 74.5

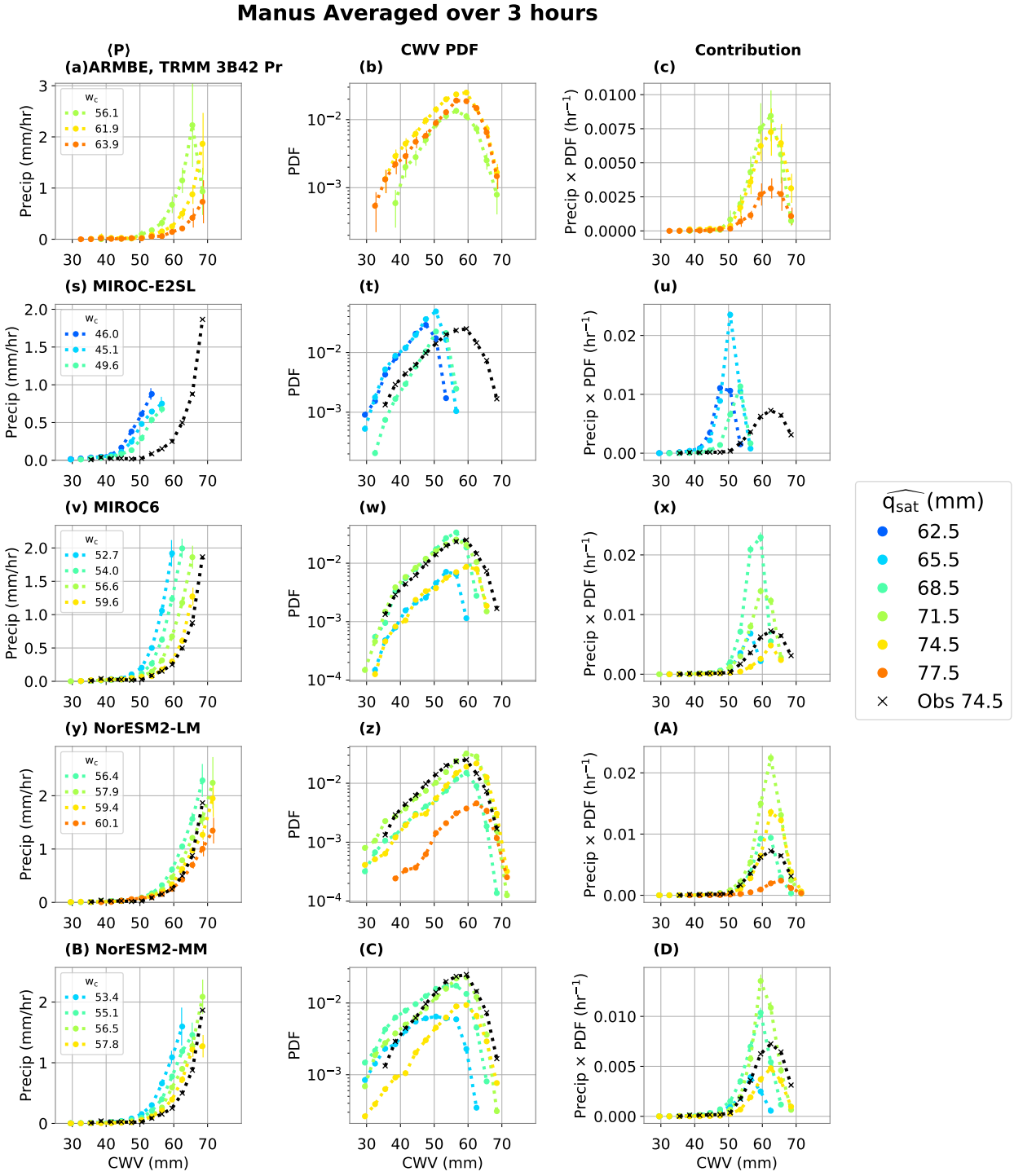

Figure 2.S4: Similar to figure S1, but for the Manus site.

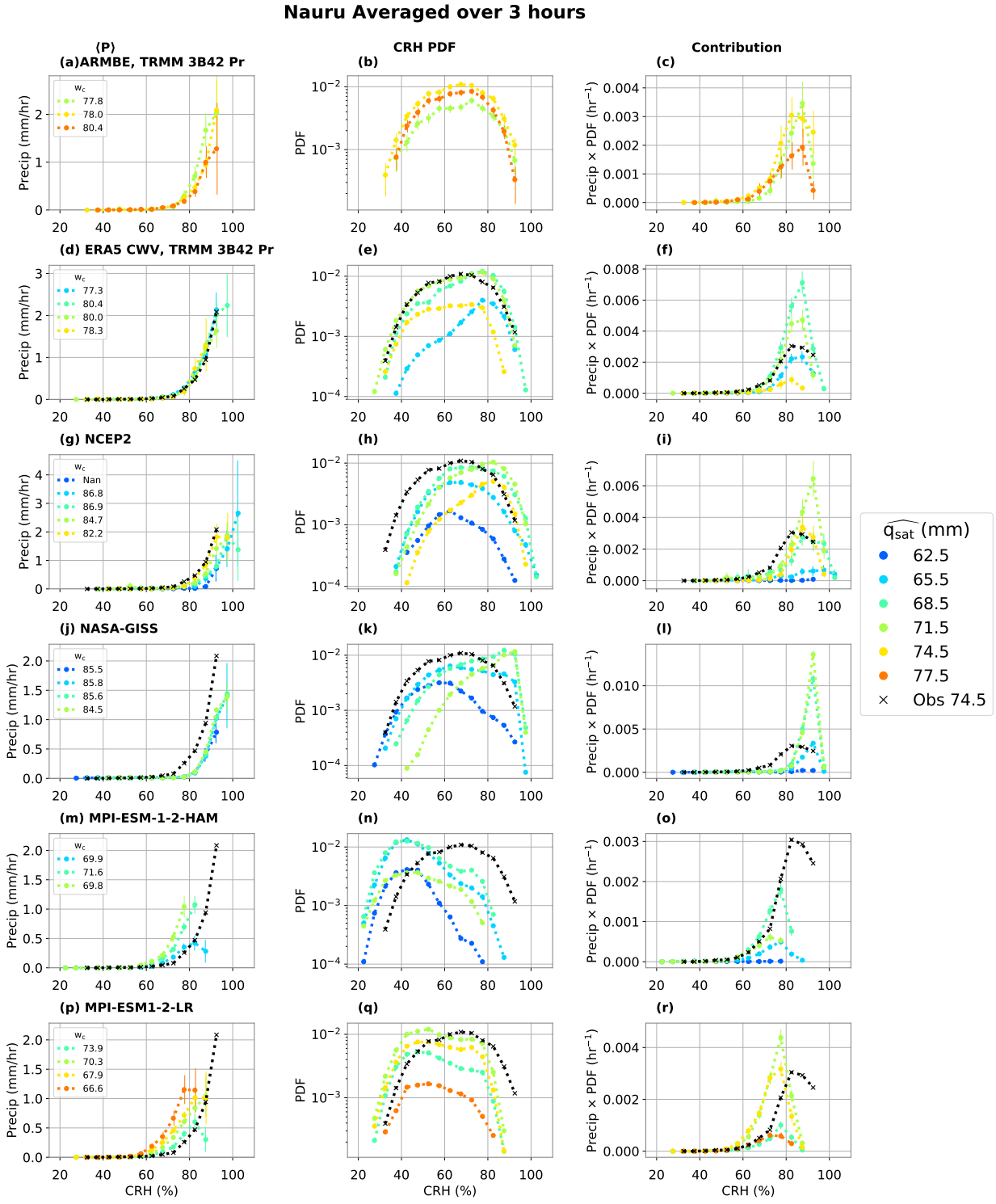
Nauru Averaged over 3 hours
⟨P⟩
CRH PDF
Contribution
(a)ARMBE, TRMM 3B42 Pr
(b)
(c)
(d) ERA5 CWV, TRMM 3B42 Pr
(e)
(f)
(g) NCEP2
(h)
(i)
(j) NASA-GISS
(k)
(l)
(m) MPI-ESM-1-2-HAM
(n)
(o)
(p) MPI-ESM1-2-LR
(q)
(r)
Precip (mm/hr)
PDF
Precip × PDF (hr⁻¹)
CRH (%)
wc
77.8
78.0
80.4
77.3
80.4
80.0
78.3
Nan
86.8
86.9
84.7
82.2
85.5
85.8
85.6
84.5
69.9
71.6
69.8
73.9
70.3
67.9
66.6
q̂sat (mm)
62.5
65.5
68.5
71.5
74.5
77.5
Obs 74.5

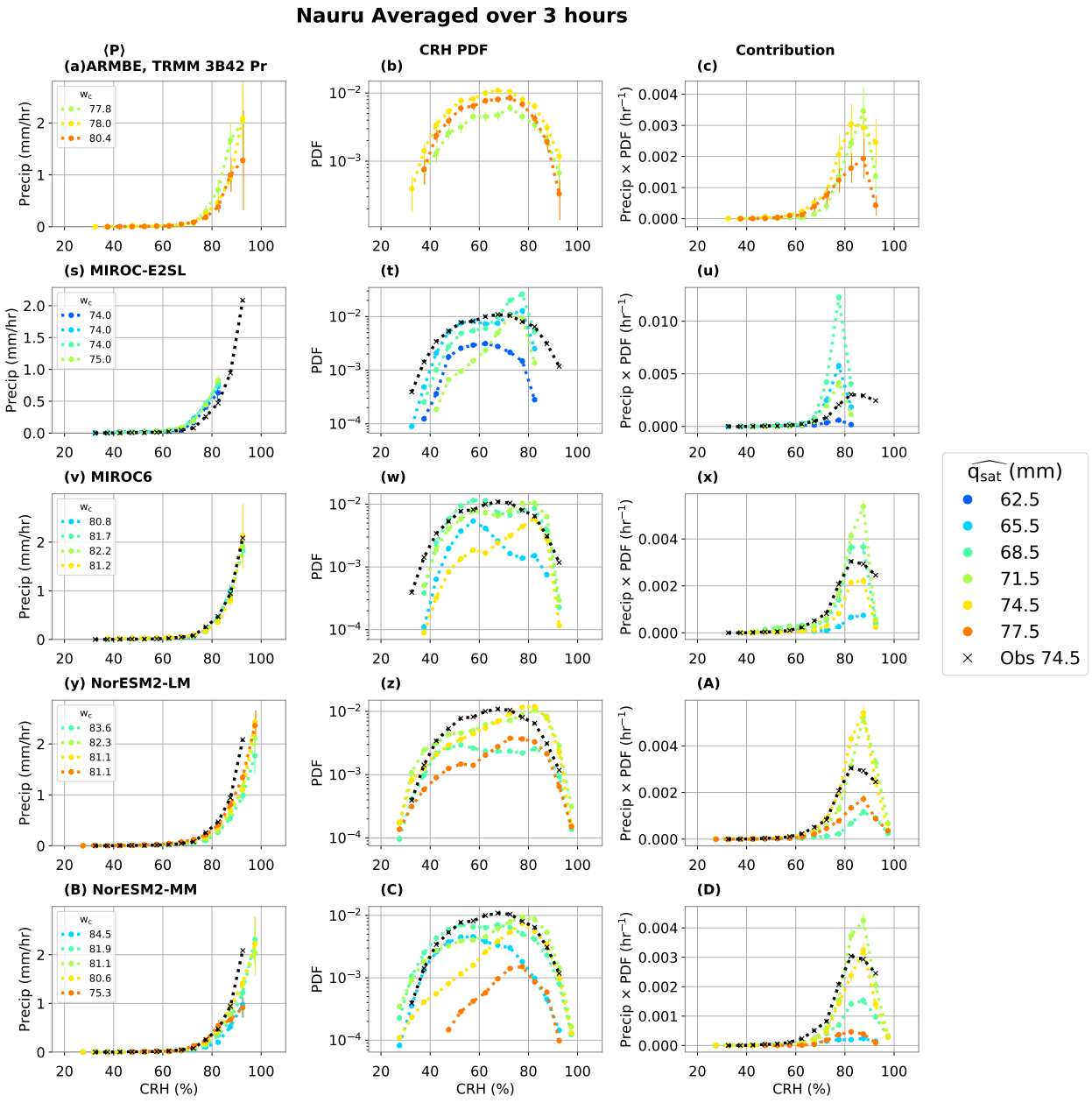

Figure 2.S5: Similar to Figure S4, but the statistics are compiled in CRH.

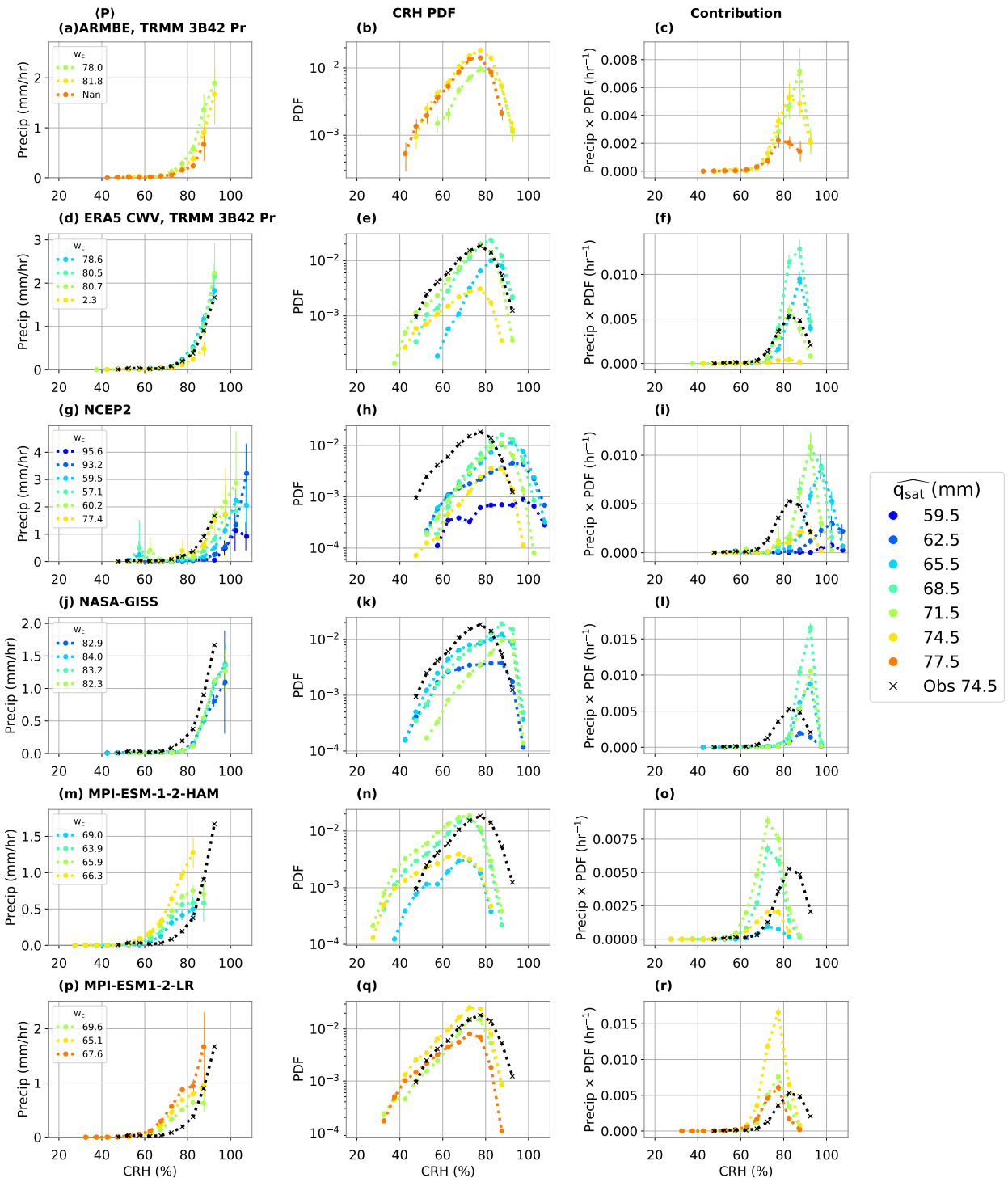
Manus Averaged over 3 hours
⟨P⟩
CRH PDF
Contribution
(a)ARMBE, TRMM 3B42 Pr
(b)
(c)
(d) ERA5 CWV, TRMM 3B42 Pr
(e)
(f)
(g) NCEP2
(h)
(i)
(j) NASA-GISS
(k)
(l)
(m) MPI-ESM-1-2-HAM
(n)
(o)
(p) MPI-ESM1-2-LR
(q)
(r)
Precip (mm/hr)
PDF
Precip × PDF (hr⁻¹)
CRH (%)
w_c
78.0
81.8
Nan
78.6
80.5
80.7
2.3
95.6
93.2
59.5
57.1
60.2
77.4
82.9
84.0
83.2
82.3
69.0
63.9
65.9
66.3
69.6
65.1
67.6
$\widehat{q_{sat}}$ (mm)
59.5
62.5
65.5
68.5
71.5
74.5
77.5
Obs 74.5

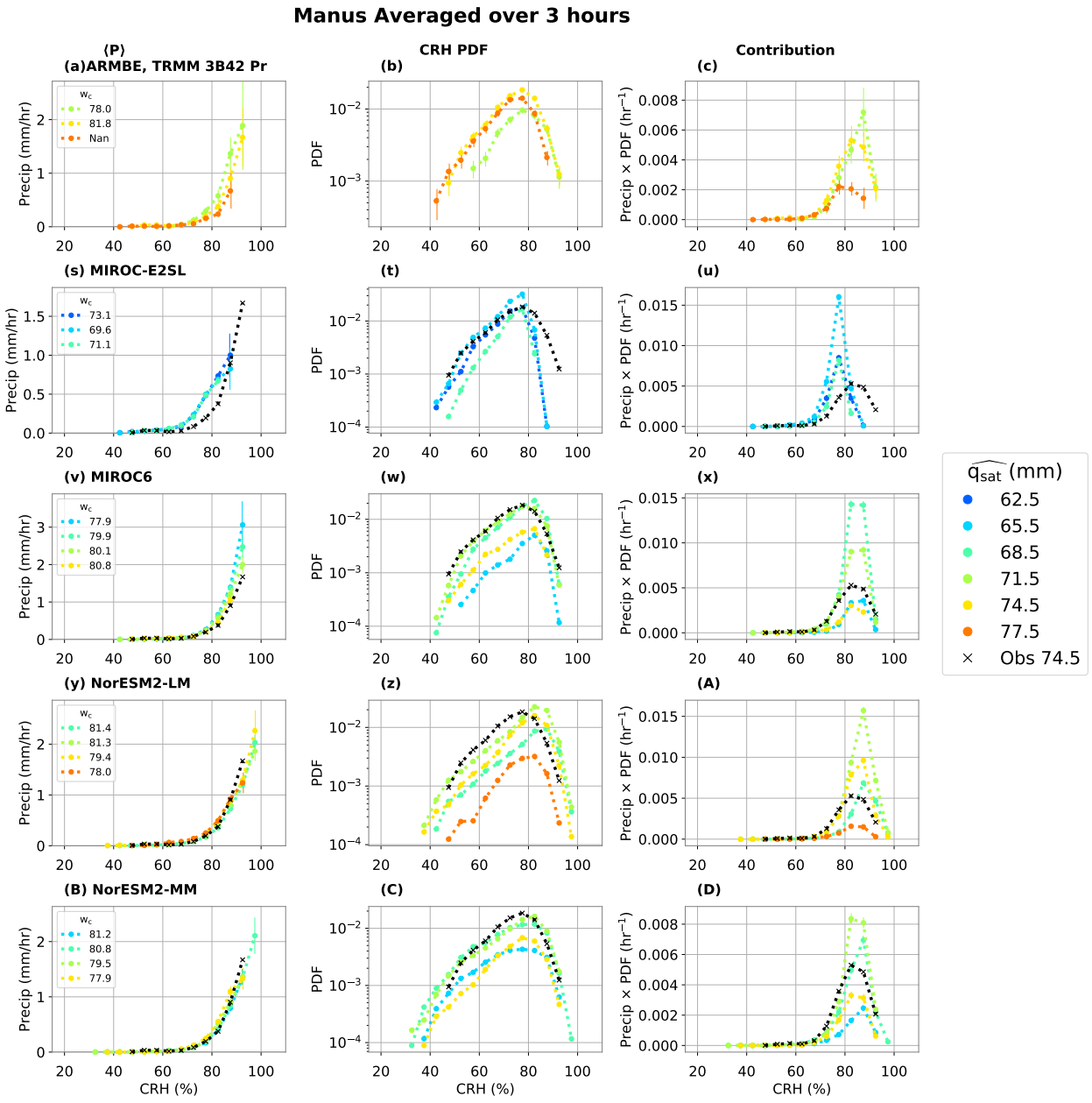

Figure 2.S6: Similar to Figure S5, but the statistics are compiled in CRH.

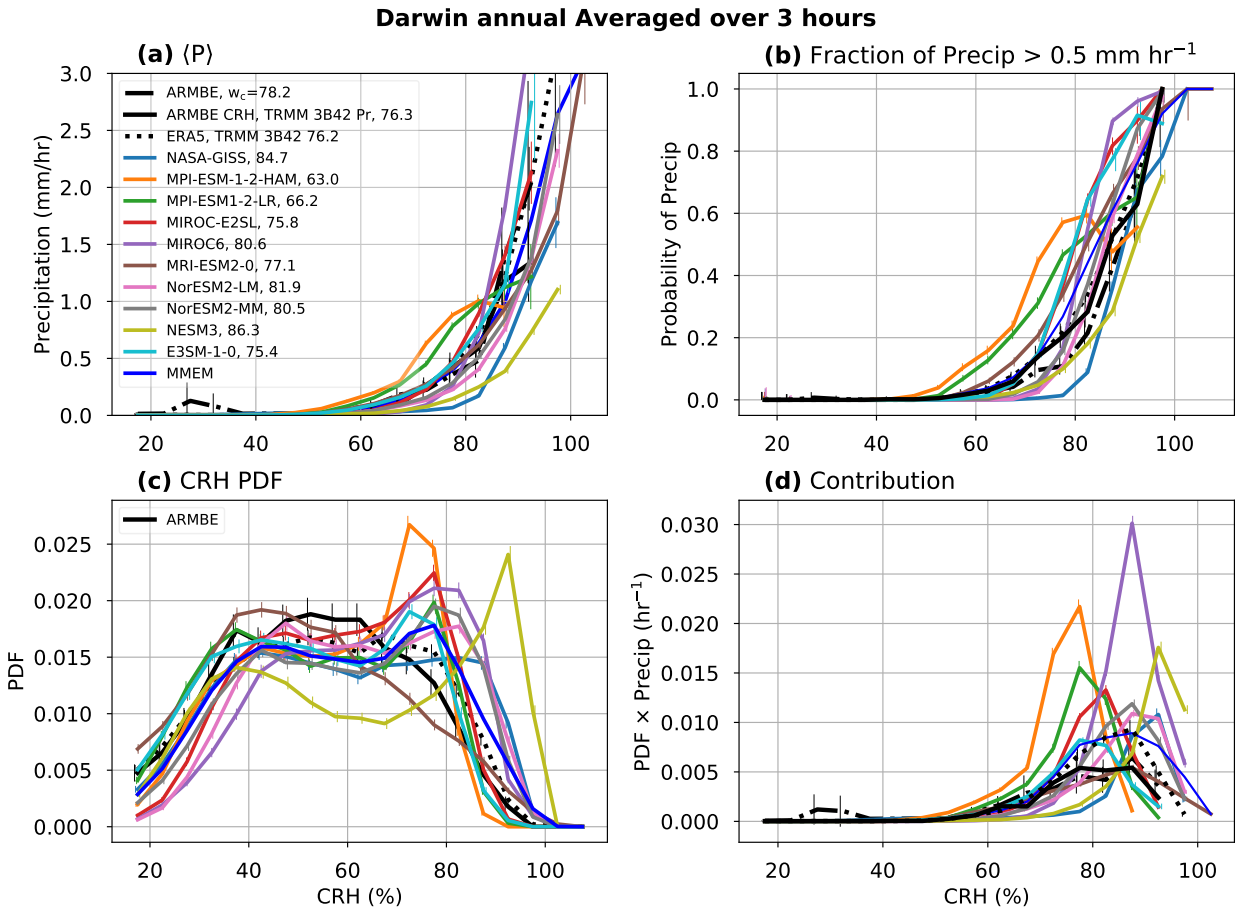

Figure 2.S7: **(a)** $\langle P \rangle$ conditioned on $\widehat{q_{sat}}$, errorbars represent the standard error **(b)** the CRH PDF conditioned on $\widehat{q_{sat}}$with 90% Wald Interval errorbars and **(c)** the precipitation contribution for each $\widehat{q_{sat}}$bin $\langle P \rangle$-weighted PDF with errorbars that represent the error propagation of the weighting (the fractional sum of error of (a) and (b)) for each $\widehat{q_{sat}}$bin for the Darwin Site. The top panel is the ARMBE CRH with TRMM 3B42 precipitation averaged over 1° centered on the nearest spatial point. Three representative models are shown, all with w_c within a close range to that of the observations. The most populated $\widehat{q_{sat}}$ bin for observations (74.5 mm) statistics are overlaid on the model (black x). Statistics are not calculated for bins with less than 10 counts.

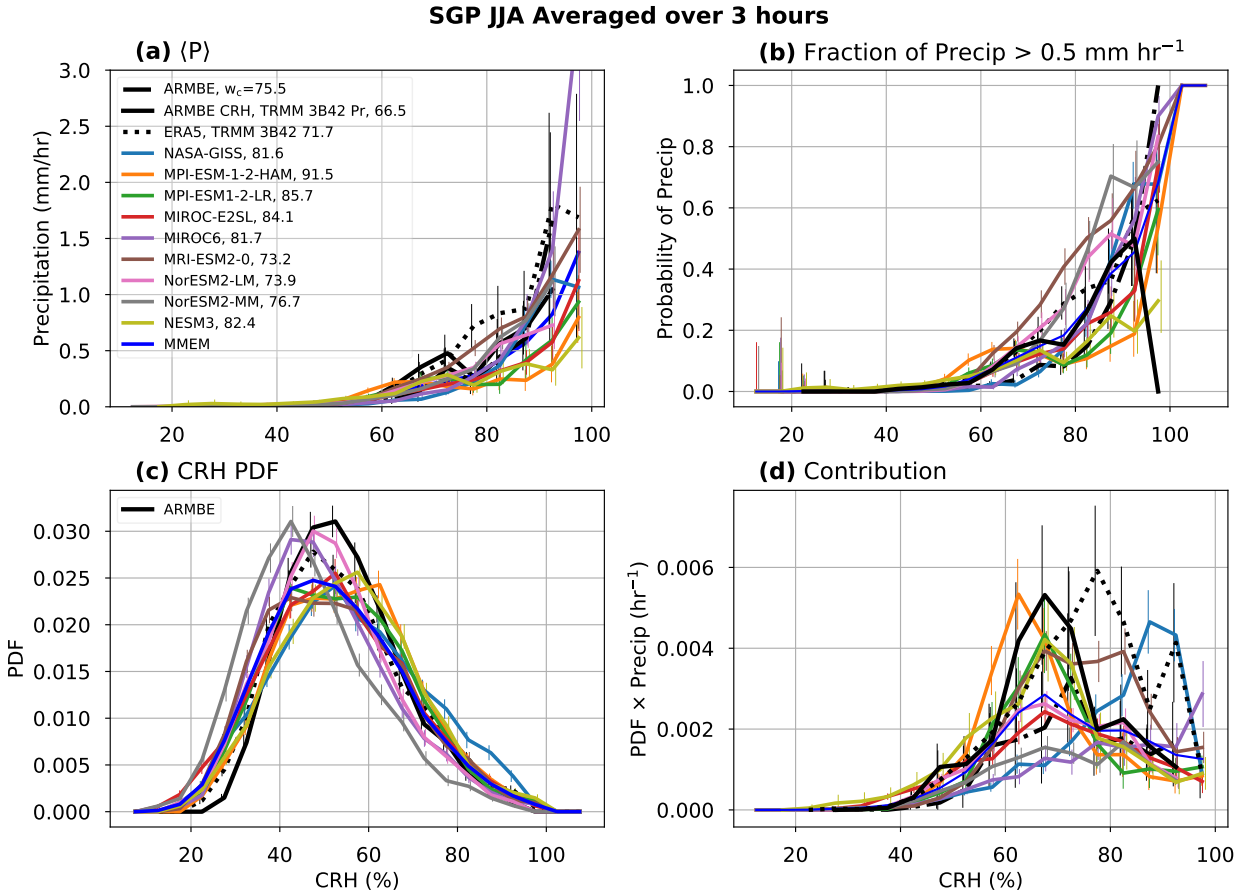

Figure 2.S8: Similar to Figure S7, but data is seasonally filtered to June, July, August as to reduce instances of frontal precipitation.

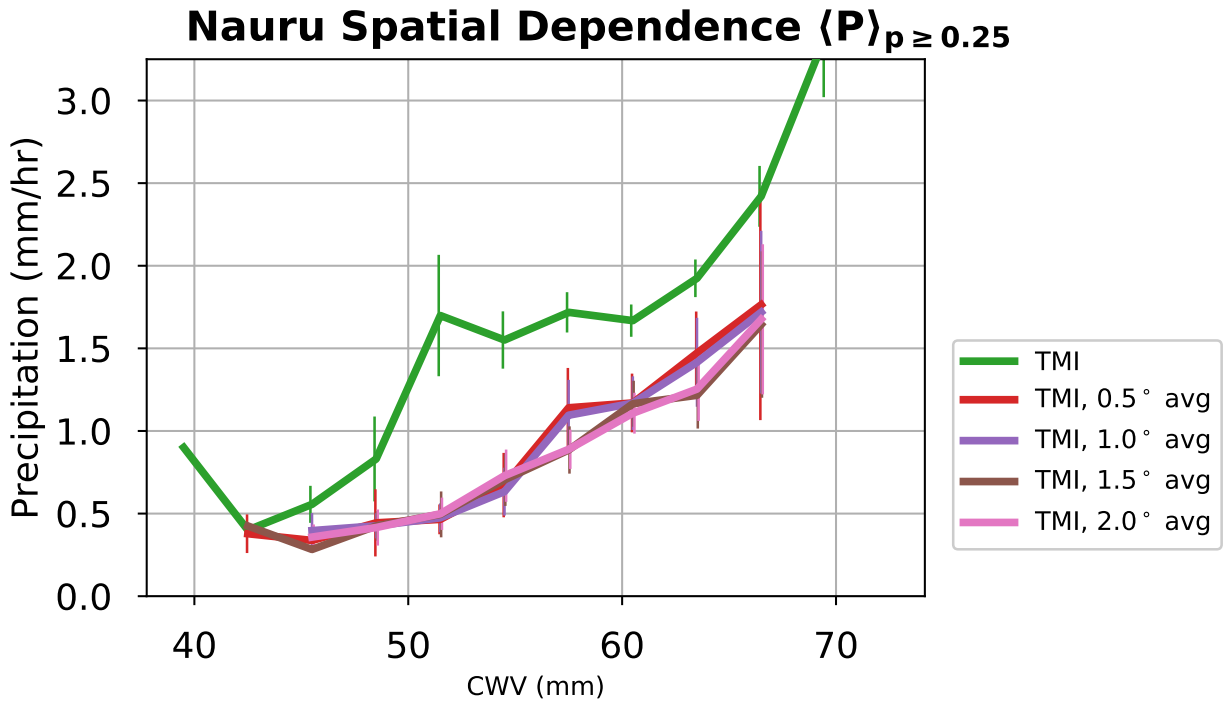

Figure 2.S9: Conditionally averaged precipitation during raining times (defined as precipitation $\geq 0.25\,\mathrm{mm\,h^{-1}}$) for different spatial averages of the TMI data.

Chapter 3

The physics behind precipitation onset bias in CMIP6 models: the pseudo-entrainment diagnostic and trade-offs between lapse rate and humidity

Abstract

Conditional instability and the buoyancy of plumes drive moist convection but have a variety of representations in model convective schemes. Vertical thermodynamic structure information from Atmospheric Radiation Measurement (ARM) sites and reanalysis (ERA5), satellite-derived precipitation (TRMM3b42), and diagnostics relevant for plume buoyancy are used to assess climate models. Previous work has shown that CMIP6 models represent moist convective processes more accurately than their CMIP5 counterparts. However, certain biases in convective onset remain pervasive among generations of CMIP modeling efforts. We

diagnose these biases in a cohort of nine CMIP6 models with sub-daily output, assessing conditional instability in profiles of equivalent potential temperature θ_e and saturation equivalent potential temperature θ_{es} in comparison to a plume model with different mixing assumptions. Most models capture qualitative aspects of the θ_{es} vertical structure, including a substantial decrease with height in the lower free troposphere associated with the entrainment of subsaturated air. We define a "pseudo-entrainment" diagnostic that combines subsaturation and a θ_{es} measure of conditional instability similar to what entrainment would produce under the small-buoyancy approximation. This captures the trade-off between larger θ_{es} lapse rates (entrainment of dry air) and small subsaturation (permits positive buoyancy despite high entrainment). This pseudo-entrainment diagnostic is also a reasonable indicator of the critical value of integrated buoyancy for precipitation onset. Models with poor θ_e/θ_{es} structure (those using variants of the Tiedtke Scheme) or low entrainment runs of CAM5, and models with low subsaturation, such as NASA-GISS, lie outside the observational range in this diagnostic.

3.1 Introduction

3.1.1 Overview

Ill-constrained representations of deep clouds and precipitation are major contributors to uncertainty in Global Climate Model (GCM) projections, including, but not limited to: precipitation extremes (Allen and Ingram, 2002; Meehl et al., 2000; Pall et al., 2007; Schneider et al., 2010; Trenberth et al., 2003), the diurnal cycle of precipitation (Covey et al., 2016; Del Genio and Wu, 2010; Hourdin et al., 2013; Rio et al., 2009; Tang et al., 2021, 2022; Xie et al., 2019), and the Madden-Julian Oscillation (Del Genio, 2012; Kim et al., 2012; Zhu and Hendon, 2015). Entraining plume models and their underlying assumptions serve as the basis of most GCM convective schemes (Arakawa and Schubert, 1974; Chikira and Sugiyama, 2010; Kain and Fritsch, 1990; Schiro et al., 2018b; Zhang and McFarlane, 1995, e.g), oftentimes relying on integrated measures of instability to initiate convective updraft

and subsequent precipitation. The environmental (gridscale) response to this instability is tethered to local convection (subgrid-scale) through large-scale governing equations which are typically consistent with quasi-equilibrium assumptions—instability generated in the large scale is removed by convective heating (Arakawa and Schubert, 1974; Manabe et al., 1965, e.g.).

Thermodynamic profiles from Atmospheric Radiation Measurement (ARM) sites provide valuable information for processes relevant to tropical clouds and their interaction with the large-scale environment. From the vertical structure of temperature and humidity, the potential for moist convection is assessed through relations of the equivalent potential temperature, θ_e, and equivalent saturation potential temperature, θ_{es}. Being a conserved quantity under adiabatic lifting, θ_e profiles provide theoretical buoyancy measures of environments—similar to traditional meteorological metrics such as CAPE—with weighting of height levels emulating the entrainment process undergone by steady-state plumes (more detail provided in section 3.4). This plume formulation, accompanied by simple entrainment assumptions, provides a framework for gauging model biases with respect to the onset of convection. Working towards a process oriented diagnostic of convection—diagnostics which isolate a physical process, target related parameters in GCMs and relay actionable feedback (Maloney et al., 2019)—we seek to condense these vertical structures of moisture and temperature using key metrics of entraining plume buoyancy. We are led to intermodel differences in the relationships among: (i) the decrease with height of θ_{es} in the lower free troposphere (LFT), referred to as the θ_{es} lapse rate for brevity; (ii) the boundary layer θ_e; and (iii) the subsaturation (as measured by $\theta_e - \theta_{es}$) of the LFT. Building on prior theoretical work concerning quasi-equilibrium, we present a "pseudo-entrainment" process-oriented diagnostic. The pseudo-entrainment diagnostic is an estimation of entrainment under the bulk plume formulation that explains tradeoffs between tropical lapse rates (stability) and moisture. We term it the pseudo-entrainment diagnostic because even when assumptions do not hold well, it is a useful large-scale indicator of processes relevant to impacts of entrainment. Additionally,

the pseudo-entrainment diagnostic helps identify convective onset biases—precipitation being initiated too early or late as represented by the 'pickup' of precipitation.

3.1.2 Convective onset and the role of entrainment

The 'pickup' in precipitation statistics first identified on daily (Bretherton et al., 2004) and subdaily (Peters and Neelin, 2006) timescales in which the conditionally-averaged precipitation picks up sharply after a critical value of column relative humidity (CRH) is reached, represents the occurrence of conditional instability in the transition to deep convection (Holloway and Neelin, 2009b; Schiro et al., 2016b). The pickup is observed over tropical land and ocean in observational records (Ahmed and Schumacher, 2017; Neelin et al., 2009; Schiro, 2017) and models (Kuo et al., 2020) and has been used in GCM evaluation in CMIP5 (Rushley et al., 2018) and CMIP6 (Emmenegger et al., 2022) models. The precipitation-CRH relationship reflects the effects of entrainment on the buoyancy of convective plumes (Holloway and Neelin, 2009b). The importance of the lower-free tropospheric (LFT) moisture in this regard is well established and is reflected in the pickup (Ahmed and Schumacher, 2015; Bretherton et al., 2004; Kuo et al., 2018; Neelin et al., 2009).

Considerations of entrainment/dilution of CAPE have led to more realistic representations of convective processes in models (Zhang, 2009); lack of entrainment can render models unable to reproduce convective variability across subdaily to interannual timescales (Del Genio and Wu, 2010; Kim et al., 2012; Neale et al., 2008; Tokioka et al., 1988). More recently, measures of LFT buoyancy have expanded on the relationship between the entrainment process and precipitation (Adames et al., 2021; Ahmed and Neelin, 2018a, 2021a; Wolding et al., 2020, 2022; **?**). Specifically, observed mass flux profiles and vertical velocities imply substantial entrainment of environmental air through the lower free troposphere (Giangrande et al., 2016; Kumar et al., 2015; Schiro et al., 2018b). Observational field campaigns (Yeo and Romps, 2013) and modelling studies (McGee and van den Heever, 2014) point to organized flow in mesoscale convective systems, with a substantial LFT inflow into the convective updraft.

Signatures of heavy entrainment inspired the Deep-Inflow formulation of mixing in Holloway and Neelin (2009b), which has proven useful in estimating convective instability (similar to GCM formulation of entraining CAPE) and is used in this study.

Conditioning precipitation on a form of entraining CAPE (theoretical buoyancy of an entraining plume) proves more successful than the traditional measure of CAPE stemming from the nonmixing assumption in predicting convection (shown in section 3.5.3 and in Adames et al. (2021); Ahmed and Neelin (2021a)). However, estimating the exact degree of entrainment undergone by a convective plume from observational products remains a complex problem. Attempts at estimating entrainment rates often requires knowledge of cloud-top height from observational snapshots (Jensen and Del Genio, 2006; Luo et al., 2010) or additional assumptions of the degree to which the plume is reflected in the environmental profile.

3.1.3 Small buoyancy approximation

Such estimations of plume trajectories depend on the environment, but also interact with it. The concept of convective adjustment posits that convection acts to remove convective instability by adjusting the non-convecting large-scale environment (Arakawa and Schubert, 1974; Manabe and Strickler, 1964), assuming that gravity waves quickly homogenize temperature anomalies in the free troposphere (Bretherton and Smolarkiewicz, 1989; Sobel and Bretherton, 2000) or that the large scale environment adjusts to anomalous temperature introduced by the plume. Convective adjustment is employed as a closure in several convective schemes (Betts, 1986; Betts and Miller, 1986; Keil et al., 2014; Manabe et al., 1965; Manabe and Strickler, 1964) and is generalized as convective quasi-equilibrium (e.g., Arakawa and Schubert, 1974; Emanuel et al., 1994). The adjustment process is assumed to happen instantaneously or with a finite adjustment timescale (Bechtold et al., 2008b; Moorthi and Suarez, 1992; Zhang and McFarlane, 1995; **?**). The exact measure of instability can vary among implementations, with CAPE and the cloud-work function being common choices. A timescale separation

between the slow buildup of instability and fast adjustment by convection results in a state of Quasi-Equilibrium (QE; Neelin et al., 2008a; Yano and Plant, 2012).

With the QE framework in mind, the adjustment of the vertical profile of environmental temperature to that of a bulk convective plume places further emphasis on the entrainment process, mainly that the lapse rate of the environment during raining times reflects the rate of dilution of a bulk plume. In simple terms, whether the entrainment is turbulent or coherent, the effects of entrainment rely on two factors, (1) the fraction of environmental air incorporated into the plume (entrainment rate) and (2) the saturation deficit of the environmental air being entrained (the two factors can compensate to achieve the same amount of dilution of a parcel such as high entrainment of moist air or low entrainment of dry air). QE predicts that the temperature and moisture profiles in the tropics reflect this process of entrainment—not just in strongly convective plumes but in the aggregate effect of the ensemble of all tropical convection (Bao and Stevens, 2021; Bao et al., 2021; Singh and Neogi, 2022; Singh and O'Gorman, 2013; Singh et al., 2019).

The *small buoyancy approximation*—the approximation that buoyancy is minimized as the environment adjusts to anomalous temperatures introduced by the plume—applies if the convective adjustment timescale is sufficiently fast. The leading order approximation has the large-scale temperature and moisture profile adjusted to that of the convection (zero buoyancy), while the precipitation and other convective effects occur due to the small departures from this (e.g., Neelin and Yu, 1994; Neelin and Zeng, 2000). The leading order (small buoyancy) approximation can be used to estimate radiative-convective equilibrium temperature and moisture profiles (Singh and O'Gorman, 2013; Zhou and Xie, 2019) and provides a method for consistently treating departures from zero buoyancy associated with raining events (e.g. **?**). In section 3.7, we derive the "pseudo-entrainment" diagnostic, an estimate of entrainment undergone by a bulk plume through the LFT, by applying the small buoyancy approximation to thermodynamic profiles of the environment.

3.1.4 Diagnostics from moist thermodynamic profiles

Due to this interaction, tropical atmospheric temperature and moisture profiles reflect the processes contributing to plume buoyancy: non-entraining aspects of conditional instability are captured by atmospheric boundary layer (ABL) moist entropy relative to LFT temperature (measured by saturation moist entropy) and dilution and entrainment are seen in the dependence on moistening of the LFT). In convective scheme formulations, the convective trigger requires a degree of preconditioning—moistening and warming of ABL along with moistening and cooling of LFT—and with it, an associated magnitude of instability. For instance, the larger the effect of entrainment, the greater the amount of preconditioning required for convection to initiate, and the larger the convective onset threshold. We build on previous observational work—framed in terms of Deep Convective Inhibition (Fuchs-Stone et al., 2020; Raymond, 2017; Raymond et al., 2003) and the Instability Index (Gjorgjievska and Raymond, 2013; Raymond et al., 2011) that finds relations between measures of LFT lapse rates of saturation moist entropy, boundary layer entropy and precipitation rates. In this study, we explore and quantify the existence of an intricate balance of lapse rates, entrainment, and climatological moisture which coalesce to form the tropical climatology to identify strengths and shortcomings in model representations of these processes.

In section 3.3 we present a measure of LFT buoyancy based the equivalent potential temperature definition. In section 3.4 we describe our plume model which allows us to calculate a scalar quantity of the average LFT parcel buoyancy, B_L, with inputs of vertical profiles of moisture, temperature under various mixing assumptions. The convective transition statistics conditioned on B_L are presented in section 3.5.3. Biases identified here are then further explored in an analysis of the vertical structures associated with different B_L regimes in sections 3.5 and 3.6. In section 3.7, we conclude with the derivation of the 'pseduo-entrainment' diagnostic, a bulk estimation of the entrainment rate from the average raining profiles, and apply this diagnostic to both models and observations.

3.2 Data and Model Descriptions

The thermodynamic structures associated with convection and their representation in global climate models (GCMs) are evaluated at the Nauru ARM site in the tropical western pacific (0°31'S, 166°54'E) for the period 1999-2009. Surface precipitation rate and vertical profiles of humidity and temperature from the ARM Best Estimate dataset (ARMBE; Xie et al., 2010), an hourly integrated product assembled from various in-situ ARM measurements, provides an observational baseline for GCM evaluation. The hourly European Center for Medium-Range Weather Forecasts Reanalysis 5th Generation (ERA5; Hersbach et al., 2020) reanalysis product provides an additional baseline for GCM evaluation. Satellite retrieval Tropical Rainfall Measuring Mission (TRMM) 3b42 version 7 precipitation measurements (Mission, 2011) provide an additional precipitation product to augment with column variables. For the purpose of model evaluation, the TRMM 3B42 precipitation is averaged spatially over 1° from its 0.25°×0.25° resolution, centered on the lat-lon point nearest to the sites.

Output from 9 ocean-atmosphere coupled GCMs' historical experiment of the CMIP6 are analyzed. A summary of each model: its resolution and convective trigger/closure are shown in Table 3.1. For each model, we extract six-hourly vertical profiles of temperature and moisture and three-hourly averaged surface precipitation rate at the nearest grid point to the Nauru site over the years 1995-2015 of the CMIP6 historical experiment. Models were chosen by the availability of subdaily humidity, temperature, and precipitation at the time of the analysis. Precipitation data for NASA-GISS, MPI-ESM1-2-LR, MIROC-E2SL, MIROC6, MRI-ESM2-0, NESM3, is three-hourly averaged, while MPI-ESM1-2-HAM, NorESM2-LM, and NorESM2-MM output is six-hourly averaged. Vertical profiles for both observations and models are instantaneous snapshots. The start of the precipitation averaging window is aligned with these snapshots so that profiles of temperature and moisture lead precipitation. Vertical profiles will be used to calculate measures of lower free tropospheric buoyancy (a measure of instability similar to entraining CAPE) and are considered causal to moist convection and precipitation.

To test the efficacy of the pseudo-entrainment diagnostic, the CMIP6 models are supplemented with an additional set of perturbed-physics experiments using the Community Atmospheric Model Version 5 (CAM5; Neale et al., 2010). Two-year atmosphere-only simulations with fixed sea surface temperatures are run. The entrainment rates in the Zhang-McFarlane cumulus parameterization scheme (Zhang and McFarlane, 1995) are perturbed over a range of values: 0.25 km^{-1}, 0.5 km^{-1}, 0.75 km^{-1}, 1 km^{-1} (control), 1.25 km^{-1}. An additional case where the convective parameterization is turned off is also included

Model name	Institute	Resolution (lon × lat), vertical levels	Convective Trigger/Closure	References
NASA-GISS	Goddard Institute for Space Studies, NASA	2.00° × 2.00°, 40	Higher moist static energy of an adiabat to environment at level above/Cloud-base buoyancy	DelGenio and Yao (1993); NASA Goddard Institute for Space Studies (NASA/GISS) (2018); Schmidt et al. (2014)
MPI-ESM-1-2-HAM	Max Planck Institute for Meteorology	1.85° × 1.88°, 47	Net positive moisture convergence/CAPE	Möbis and Stevens (2012); Wieners et al. (2019a)
MPI-ESM1-2-LR	Max Planck Institute for Meteorology	1.85° × 1.88°, 47	Net positive moisture convergence/CAPE	Möbis and Stevens (2012); Wieners et al. (2019b)
MIROC-E2SL	Japan Agency for Marine-Earth Science and Technology	2.77° × 2.81°, 40	CAPE/Prognostic convective kinetic energy	Ando et al. (2021); Hajima et al. (2019)
MIROC6	Japan Agency for Marine-Earth Science and Technology	1.39° × 1.41°, 81	CAPE/Prognostic convective kinetic energy	Ando et al. (2021); Tatebe and Watanabe (2018)
MRI-ESM2-0	Meteorological Research Institute Japan Meteorological Agency	1.11° × 1.13°, 80	CAPE/CAPE	Yukimoto et al. (2019, 2011)
NorESM2-LM	Norwegian Meteorological Institute	1.89° × 2.50°, 32	CAPE/CAPE	Seland et al. (2020, 2019)
NorESM2-MM	Norwegian Meteorological Institute	0.94° × 1.25°, 32	CAPE/CAPE	Bentsen et al. (2019); Seland et al. (2020)
NESM3	Nanjing University of Information Science and Technology	1.85° × 1.88°, 47	Net positive moisture convergence/CAPE	Cao and Wang (2019); Cao et al. (2018)
CAM5	National Center for Atmospheric Research	0.90° × 1.25°, 27	CAPE/CAPE	Neale et al. (2010)

Table 3.1: List of models analyzed in this study. Table is nearly identical to Table 1 of Emmenegger et al. 2022. The references column gives the data source and the source for the convective trigger/closure.

3.3 A measure of lower free tropospheric buoyancy, B_L

Buoyancy here is written as

$$B = g\left[\frac{\delta\theta_{es}}{\kappa\theta_{es}} + 0.61\delta q_v - \delta q_c\right] \tag{3.1}$$

where θ_{es} is saturated equivalent potential temperature, δ represents the difference between the plume and the environment, with θ_{es}^p that of the parcel and θ_{es} without the superscript is that of the environment; q_v is the water vapor mixing ratio, q_c the condensate mixing ratio, and g is the acceleration due to gravity. The factor

$$\kappa = 1 + \frac{L^2 q_s}{c_p R_v T_0 T} \tag{3.2}$$

arises when converting from the temperature-based form of buoyancy (Adames et al., 2021; Raymond, 1994, and online supplemental material). In Equation (4.2), L is the latent heat of vaporization, q_s is the saturation specific humidity of the environment, c_p is the specific heat of dry air, R_v is the gas constant of water vapor, and T_0 is a constant reference temperature.

The second and third terms represent the contributions from 1) the water vapor effect on density (sometimes called the virtual effect, incorporated in the definition of virtual temperature) and 2) condensate loading.

Rewriting (3.1) provides a convenient way of comparing a slightly modified curve corresponding to θ_{es} from a plume calculation to the θ_{es} of the environment, such that the distance between these curves is proportional to buoyancy, including the virtual effect and condensate loading:

$$B = \frac{g}{\kappa\theta_{es}}\left[\underbrace{\theta_{es}^p + \overbrace{\kappa\theta_{es}(0.61\delta q_v - \delta q_c)}^{\text{Virtual Effect - Condensate Loading}}}_{\text{compare to } \theta_{es}} - \theta_{es}\right] \tag{3.3}$$

Note that virtual effect and condensate loading quantities are not conserved under parcel motion. The measure of plume buoyancy in (3.1) is similar to that used in Raymond (1994)

Variable	Description	Value	Units
g	Acceleration due to gravity	9.8	$\mathrm{m\,s^{-2}}$
L	Latent heat of vaporization	2.5	$\times 10^6\,\mathrm{J\,kg^{-1}}$
c_p	Specific heat capacity of dry air	1005	$\mathrm{J\,kg^{-1}\,K^{-1}}$
R_v	Gas constant for water vapor	461	$\mathrm{J\,kg^{-1}\,K^{-1}}$
T_0	Reference temperature	300	K
p_0	Reference pressure	1000	hPa

Table 3.2: Values of constant used for the buoyancy calculation in Equation (3.1)

and Adames et al. (2021) and differs from the measure used in Ahmed and Neelin (2018a) in that the κ factor is included in the denominator. As noted in Adames et al. (2021), the inclusion of κ does not significantly affect the results of Ahmed and Neelin (2018a) and Adames et al. (2021) but serves to scale the numerator to values $\sim$3 times smaller. Values of the constants used in this study are displayed in Table 4.1. Equivalent potential temperature, θ_e, is the temperature a parcel would attain after a moist adiabatic expansion to a low pressure, followed by an adiabatic compression to a reference pressure. It is approximately conserved in both moist and dry adiabatic reversible processes. Variables based on θ_e are more useful in approximating the conservation properties of a plume than moisture and temperature (Ahmed and Neelin, 2018a).

To interpret Equation (3.1), we now express a typical parcel lifting trajectory using θ_e-based variables. A near-surface unsaturated parcel is lifted and conserves its potential temperature θ, up until it becomes saturated at its lifting condensation level (LCL; where $\theta_e^p = \theta_{es}^p$). The parcel remains saturated in its ascent above the LCL with $\theta_e^p = \theta_{es}^p$.

The level of free convection (LFC) is where $\theta_{es}^p = \theta_{es}$. The lifting condensation level is below the LFC for a lifted parcel with no mixing assumptions, assuming the lapse rate of the environment is less than that of a dry adiabat. In a well-mixed atmospheric boundary layer, there is typically some convective inhibition below the LFC, as noted in Raymond (1994).

3.4 Plume Calculation description

In our plume calculations, we assume the bulk plume undergoes reversible moist-adiabatic transitions allowing for ice, conserving its equivalent potential potential temperature θ_e, calculated according to Equation 2.67 in Stevens and Siebesma (2020), throughout its ascent. Further technical details of mixing may be found in Holloway and Neelin (2009b); we provide a short summary here.

The bulk plume model takes the environmental profiles of temperature and moisture, and mixing coefficients as inputs. Mixing coefficients are prescribed and thermodynamic profiles are spline interpolated to 5 hPa intervals. A parcel originating from (with same temperature and moisture content) a near-surface level of the environment (in our calculations we choose a parcel at 1000 hPa) is lifted, and interacts with the environment according to the prescribed mixing scheme in its ascent.

In the absence of mixing and precipitation, the total water content is conserved and undergoes phase changes when: (1) the parcel reaches saturation below the freezing level (water vapor condenses to liquid), (2) when the freezing level is reached (liquid water is converted into ice)–during the freezing process the temperature is held at the triple-point, allowing liquid and ice to coexist—and (3) above the freezing level, ice is formed via deposition of water vapor (super-cooled water is not permitted in this equilibrium calculation). The total water content is conserved until the condensate reaches a cap of $1\,\mathrm{g\,kg^{-1}}$ and then is lost irreversibly as in Schiro et al. (2018b).

Plume calculations are carried out for two different mixing assumptions: a nomixing case (NMX) and a heavy mixing case, "Deep Inflow B" (DIB; Holloway and Neelin (2009b)) which corresponds to convective plumes which entrain approximately equal amounts of air from each level in the lower troposphere. These two mixing assumptions probe the two extreme possibilities for entrainment behavior. The NMX case plume involves lifting a parcel originating near the surface (in all calculations we assume the plume starts at 1000 hPa) such that it conserves its θ_e throughout its ascent.

The DIB case is calculated by assuming an approximately linearly increasing updraft velocity at low levels which incorporates environmental air such that it can be approximated as an average of the layers below (Adames et al., 2021; Holloway and Neelin, 2009b; Schiro et al., 2018b, 2016b):

$$\theta_e^{DIB}(p) \approx (p_s - p)^{-1} \int_{p_s}^{p} \theta_e(p')dp'. \tag{3.4}$$

From these plume values, we calculate buoyancy as presented in (3.5). To obtain a scalar value for statistical purposes, we average the lower tropospheric average buoyancy, B_L, and define it as

$$B_L = (p_s - p_{LFT})^{-1} \int_{p_s}^{p_{LFT}} B dp, \tag{3.5}$$

where the integrand, B, is determined for plume θ_{es}^{p} from each mixing scenario in (3.1).

The definition of B_L in (3.5) is similar to that previously used (Adames et al., 2021; Ahmed and Neelin, 2018a, 2021a; Wolding et al., 2022), and contains both negative and positive contributions similar to the traditional measure of convective available potential energy (CAPE) and convective inhibition (CIN). Measures of lower tropospheric buoyancy below the freezing level give the leading order behavior of a deep convection, as a convective plume needs to reach the freezing level to initiate deep convection (Ahmed and Neelin, 2018a; Powell, 2022; Stevens et al., 2017). The average in (3.5) is taken from the surface to the top of the lower free troposphere, 600 hPa (just below the freezing level).

The primary difference between earlier uses of B_L and the one we present here is that we account for virtual effects and condensate loading in B. Virtual effects are sometimes neglected, but their contributions to buoyancy are not necessarily small (e.g., Emanuel, 1994; Holloway and Neelin, 2009a; Sarachik, 1985; Yang et al., 2022). From the arguments of the plume model and the definition of buoyancy in Equation (3.1), the virtual contributions of vapor tend towards increasing buoyancy as the plume is at saturation above the boundary layer. Condensate loading effects can likewise be substantial (Bacmeister et al., 2012; Xu and

Randall, 2001), limited by entrainment and by precipitation processes that remove condensate from the parcel. Here the microphysics of precipitation is simplified to a prescribed condensate cap. This limits the condensate loading to realistic values (Neale et al., 2010; Xu and Randall, 2001). The environment can be assumed to be condensate-free, so $\delta q_c \approx q_c$ of the plume. Its maximum contribution to B is gq_c, so that with a condensate cap of $1\,\mathrm{g\,kg^{-1}}$, the condensate contribution to B is approximately -1 $\times$ $10^{-2}\,\mathrm{m\,s^{-2}}$. Increasing the condensate cap can result in a significant drop in B_L. The vapor effect contribution remains relatively small $\sim$ $1 \times 10^{-2}\,\mathrm{m\,s^{-2}}$.

3.5 Key Profile Properties and buoyancy estimation

3.5.1 Example Profile

Plume calculations are applied to all environmental snapshots of temperature and moisture. An example of the plume calculations and the environmental values of equivalent potential temperature are shown in Figure 3.1. The freezing of plume liquid water may be identified by the kink in the trajectory of the plume θ_e (dashed lines) around 500 mbar (more pronounced in the NMX case (orange dashed) in Figure 3.1 in both panels. The gradual increase of θ_e with height in the NMX case in Figure 3.1 occurs due to the loss of condensate (after reaching the $1\,\mathrm{g\,kg^{-1}}$ cap slightly above the LCL). The shedding of condensate lends the parcel a decreased heat capacity, and continued freezing via vapor deposition and latent heat of fusion heat the parcel. The θ_{es} of the plumes (used to calculate buoyancy as in Equation (3.1)), has the virtual and condensate loading contributions of buoyancy added in Figure 3.1 according to the RHS of (3.3). The contributions are net positive for most of the lower troposphere (as seen by the difference between the parcel solid and dashed curves), albeit small ($\sim$ 1 K) and mostly reflect the shape of the θ_e profile of the environment—that is, the effect is greatest in those layers where the θ_e is low.

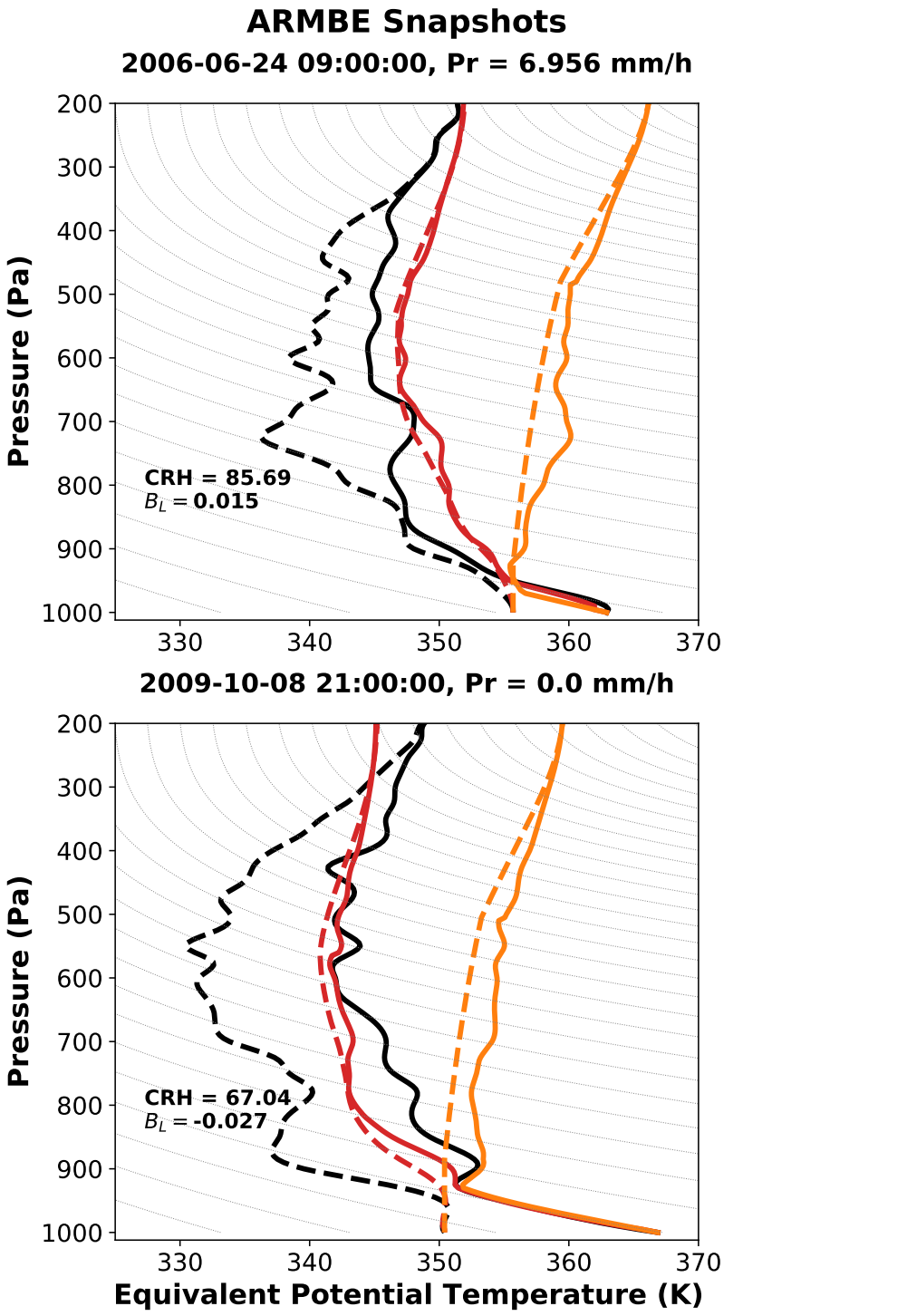
ARMBE Snapshots
2006-06-24 09:00:00, Pr = 6.956 mm/h
Pressure (Pa)
CRH = 85.69
B_L = 0.015
2009-10-08 21:00:00, Pr = 0.0 mm/h
CRH = 67.04
B_L = -0.027
Equivalent Potential Temperature (K)
θ_e
θ_{es}
θ_e^{DIB}
$\theta_{es}^{DIB} + \kappa\theta_{es}[0.61\delta q_v - \delta q_c]$
θ_e^{NMX}
$\theta_{es}^{NMX} + \kappa\theta_{es}[0.61\delta q_v - \delta q_c]$

Figure 3.1: Examples of the plume model calculations in the ARMBE dataset. Dashed lines represent the θ_e of the environment (black), the DIB-mixing plume (red) and the nomixing plume (orange) with a condensate cap of $1\,\mathrm{g\,kg^{-1}}$. The black solid line represents the θ_{es} of the environment, while the solid lines for the plume calculations give $\theta^p_{es} + \kappa\theta_{es}\,[0.61\delta q_v - \delta q_c]$. Parcel buoyancy (including virtual effects and condensate loading) is positive when this exceeds environmental θ_{es} per (3.3). Gray contours are lines of constant potential temperature. The top panel is an example of an individual sounding for a precipitating case, and the bottom for a nonraining case. Note that equivalent potential temperature on the x-axis is defined for reversible processes.

3.5.2 Profiles averaged for raining events

Figure 3.2 shows the plume and environmental profiles averaged over raining events (when precipitation rate$\geq 0.5\,\mathrm{mm\,h^{-1}}$). In ARMBE and ERA5 the average DIB profile (Fig. 3.2a, b; red line) exhibits negative buoyancy throughout the LFT. This is also the case for the MPI models (Fig 3.2d,e), In some models, during a raining event, the DIB profile shows positive buoyancy at a low level ($\sim$900-800 hPa) due to peak in θ_{es} (Fig. 3.2f,g,h,i,j) Only in the NASA-GISS model (Fig. 3.2c) does the DIB plume have positive buoyancy throughout the entire LFT. Nonentraining CAPE can be compared among models by the difference between the NMX plume (Fig. 3.2, orange line) and the θ_{es} (black). This difference compares the boundary layer θ_e and the lapse rate of θ_{es}. The MPI models and NESM3 exhibit small differences between their NMX plume and their θ_{es} profile, while NASA-GISS, MRI-ESM2-0, ad the NorESM2 models show stark differences.

Fig. 3.2 shows that the NMX and DIB profiles bound the model environmental θ_{es} profiles. At the leading order, the plume θ_{es} is expected to set the environmental θ_{es} profile based on convective adjustment arguments [small-buoyancy and WTG as outlined in section 13.1.3; see also (Singh and O'Gorman, 2013; Zhou and Xie, 2019)]. Models with strongly entraining convective schemes are expected to have θ_{es} profiles closer to DIB, while models with weak entrainment are expected to be closer to NMX. Based on this argument, we deduce that the MPI models (Figs. 3.2d and e) have weakly entraining convection, while NASA-GISS (Fig. 3.2c) and MRI-ESM2-0 (Fig. 3.2h) have strongly entraining convection. These patterns are

also consistent with Ahmed and Neelin (2021a), who noted that the MPI models—in contrast to most CMIP6 models—are inadequately sensitive to LFT moisture. Figs. 3.2a and b imply substantial entrainment rates for the observational baseline (but smaller than NASA-GISS and MRI-ESM2-0). If the difference between boundary layer θ_e and the LFT θ_{es} is taken as a measure of convective instability (**?**), it would appear that the MPI models are highly stable to convection when compared to NASA-GISS and MRI-ESM2-0. However, this measure is relevant for non-entraining convection—instead these results imply a tradeoff between model entrainment and model θ_{es} profiles, previously noted in Singh and O'Gorman (2013) and **?**. This tradeoff motivates construction of the pseudo-entrainment metric in section 3.7.

3.5.3 Convective transition statistics stratified by lower tropospheric buoyancy, B_L

The convective transition statistics over tropical oceans for a number of CMIP6 models in B_L were presented in Ahmed and Neelin (2021a), including a baseline of ERA5 B_L matched with TRMM-3B42 precipitation. Similar statistics conditioned on column water vapor (CWV) and column relative humidity (CRH) for the models considered here were presented in Emmenegger et al. (2022), including ARMBE data as an additional measure of an observational baseline. Similar to the conditional-average precipitation rate, $\langle P \rangle$, in CRH and CWV, the precipitation conditioned on B_L presented here in Figure 3.3a, is sharp, or rapidly increases past some critical value of B_L—this rapid increase in $\langle P \rangle$ is referred to as the 'pickup.' The critical value, B_{Lc} is fit to each pickup as in Emmenegger et al. (2022), through finding the B_L value in which a linear fit of monotonically increasing $\langle P \rangle$ crosses $0.25\,\mathrm{mm\,h^{-1}}$. The choice of $0.25\,\mathrm{mm\,h^{-1}}$ instead of $0\,\mathrm{mm\,h^{-1}}$ was chosen to exclude nonzero rates of precipitation at low B_L stemming from the persistent 'model drizzle problem', where models precipitate at low rates too often (Chen and Dai, 2019; Jing et al., 2017; Rushley et al., 2018; Stephens et al., 2010) and other spurious deviations at low B_L (nonzero rates observed in the ARMBE data $\sim -0.075\,\mathrm{m\,s^{-2}}$). The B_{Lc} is listed in the legend of Figure 3.3.

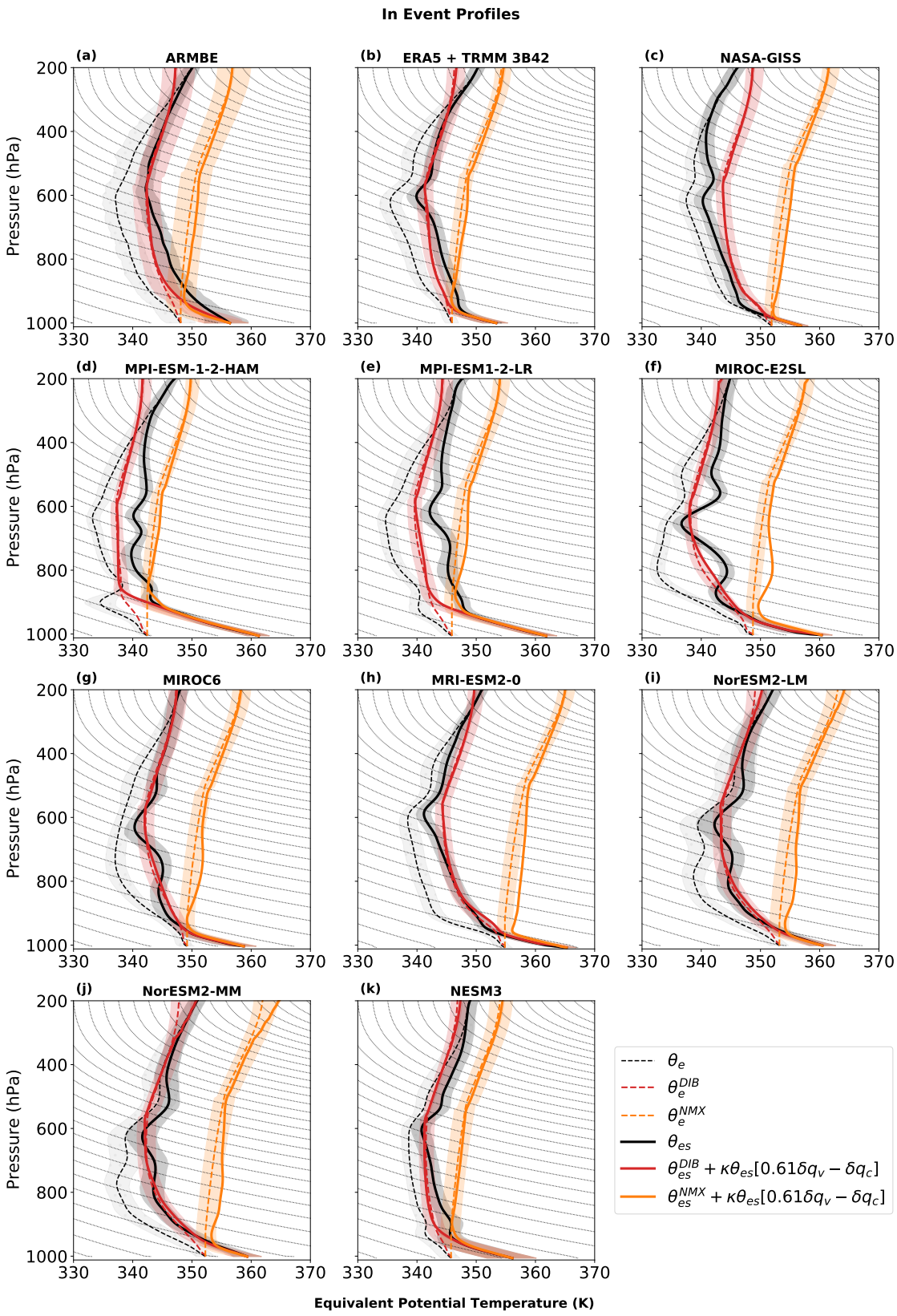
In Event Profiles
(a) ARMBE
(b) ERA5 + TRMM 3B42
(c) NASA-GISS
(d) MPI-ESM-1-2-HAM
(e) MPI-ESM1-2-LR
(f) MIROC-E2SL
(g) MIROC6
(h) MRI-ESM2-0
(i) NorESM2-LM
(j) NorESM2-MM
(k) NESM3
Pressure (hPa)
200
400
600
800
1000
330
340
350
360
370
Equivalent Potential Temperature (K)
θ_e
θ_e^{DIB}
θ_e^{NMX}
θ_{es}
$\theta_{es}^{DIB} + \kappa\theta_{es}[0.61\delta q_v - \delta q_c]$
$\theta_{es}^{NMX} + \kappa\theta_{es}[0.61\delta q_v - \delta q_c]$

Figure 3.2: Average profiles during raining times (precipitation rate $\geq 0.5\text{mm}\,\text{h}^{-1}$) for environmental θ_e (black-dashed), θ_{es} (black-solid) and plume trajectories, Deep-Inflow B (DIB, red) and Nonmixing (NMX, orange). For the plume trajectories, solid lines show $\theta_{es} + \kappa\theta_{es}(0.61\delta q_v - \delta q_c)$ to evaluate buoyancy with condensate loading and water vapor effects included following (3.3), such that comparison to environmental θ_{es} is proportional to buoyancy, as in Fig. 1. Shading corresponds to 25th to 75th percentiles. Contours are lines of constant potential temperature. Note that the nonmixing case θ_e profile is not constant in the vertical due to loss of condensate, since the x-axis is reversible equivalent potential temperature.

Results of the convective-onset statistics conditioned on B_L are similar to those reported in Emmenegger et al. (2022): most models pickup at slightly higher B_L than the baselines (the baselines are ARMBE and ERA5; 3.3a) and increase their probability of raining too quickly (3.3c). In particular, the MPI models pickup early while NASA-GISS picks up noticeably late. Additionally, model pickups are driven primarily by an increasing probability of precipitation, that is, model precipitation rates in the raining state are not sufficiently sensitive to B_L.

It is important to note that differences are observed between the statistics of ERA5 and ARMBE. These arise from the same biases reported in Emmenegger et al. (2022)—ERA5 exhibits a cold-bias in temperature with slightly lower humidity in the LFT, leading ERA5 to have a B_L-PDF shifted towards higher values. The biases in ERA5 can be seen in the mean profiles of θ_{es} and θ_e (3.5 and 3.6 panel l respectively).

The PDFs of B_L (Fig. 3.3b) exhibit features similar to their counterparts in CRH and CWV (not shown, see Figures 1-4 of Emmenegger et al. (2022)), in that the gradual slope of probability on left side of he PDF is limited by dry regime dynamics while sharp decrease in probability on right side of the PDF, or 'drop-off' is limited by precipitation; that is, past the critical value of the pickup, precipitation becomes an effective moisture (hence B_L) sink. **?** and Wolding et al. (2022) interpret the B_L PDFs from a QE perspective—convection relaxes a perturbed thermodynamic profile to an adjusted state—remarking that the peak of the PDF at B_{Lc} implies that B_{Lc} is the adjusted QE state. Excursions above B_{Lc} are consumed rapidly by convection while excursions below are consumed at a slower rate, as indicated by the slopes of the drop-off. More specifically—in the QE sense—the adjusted state represented

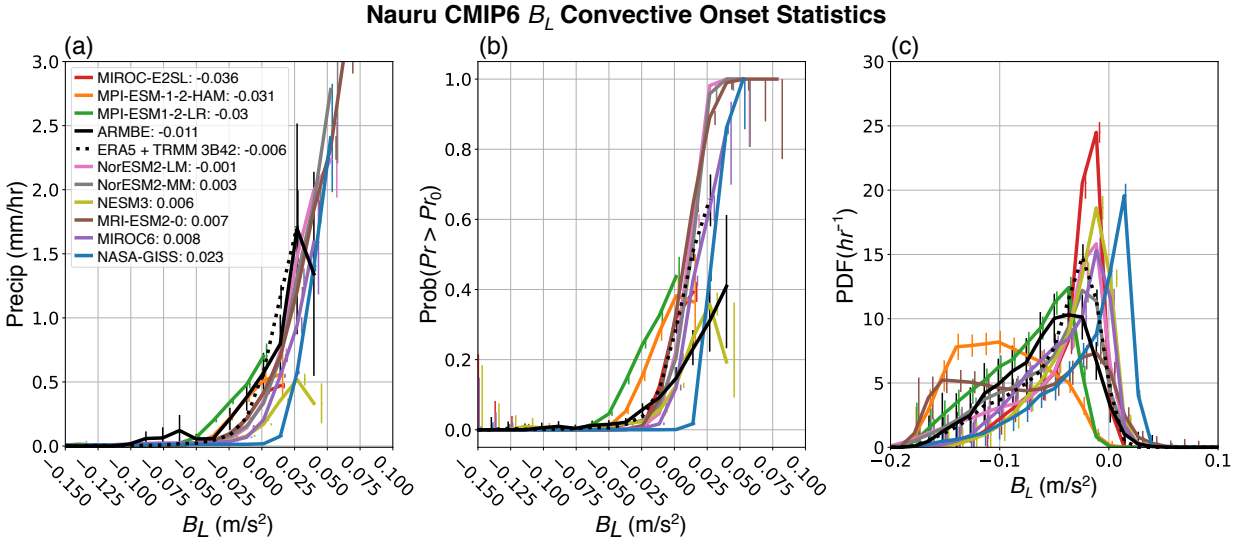

Figure 3.3: The convective onset statistics for the observational and reanalysis products (black, ARMBE [solid] and ERA5 [dotted]) and the CMIP6 model cohort (colors) conditioned on a measure of lower tropospheric buoyancy, B_L, for the DIB-mixing plume model. (a) The conditional average precipitation with the legend in ascending order of a linear fit estimation of the critical B_L value of the pickup, errorbars represent the standard error. (b) The conditional probability of precipitation (for precipitation rate $\geq 0.5\text{mm}\,\text{h}^{-1}$); errorbars are the Wilson Score Interval for 95% confidence. (c) The PDFs of B_L; with 95% Wald Interval errorbars.

by B_{Lc} represents a near-zero buoyancy state by which buoyancy generation via large-scale forcing is balanced by the convective consumption of buoyancy (Arakawa, 2004; Neelin et al., 2008b; Peters and Neelin, 2006; Wolding et al., 2022; **?**). Relationships between the QE state and adjustment process and convective instability as seen in vertical thermodynamic structures in observations and models are expanded on in Sections 5d and 6. Building on **?**, we further explore the QE-state and its trade-offs between moisture and temperature induced by the variety of representations of entrainment in GCMs in Section 7.

3.5.4 Vertical profiles across the convective transition

Figure 3.4 shows profiles conditioned on B_L for ERA5 and ARMBE. Figures 3.4a and e shows the profiles of buoyancy, B, according to Equation (3.1). The B_L binning is performed according to the average of these profiles from the surface to 600 hPa. Buoyancy remains

close to zero through the boundary layer. At low (high) B_L, the B profiles decrease (stays relatively constant) throughout an intermediate layer from 900 to 700 hPa and flatten out until reaching the upper troposphere around 500 hPa. A kink in the profiles is apparent at high B_L bins due to contribution in temperature of freezing in the plume model.

Equivalent potential temperature, θ_e increases throughout the column as B_L increases (Fig 3.4a and e). At lower B_L bins, the θ_e profile decreases rapidly just above the boundary layer up to a minimum near the 850 hPa level before increasing up through the rest of the column. As B_L increases, θ_e begins to flatten out, the decrease of θ_e from the boundary layer lessens. The θ_e profile is more closely related to variations in the moisture content of the column as opposed to temperature (Ahmed and Neelin, 2018a). This can also be inferred from the θ_{es} structure (figures 3.4b and f), which is solely a measure of temperature in that higher B_L values are associated with a cooler column but exhibit a higher θ_e.

For both ARMBE and ERA5, higher buoyancy is achieved through a noticeable cooling and moistening in the LFT. At lower B_L, the θ_{es} (figures 3.4b and f) profile shows a decrease from the surface roughly along a line of constant potential temperature up until just below the 900 hPa level from where θ_{es} increases until reaching a maximum in the LFT at around the 800 hPa level in ARMBE and just below the 800 hPa level in ERA5, then gradually decreases with height. Higher B_L profiles continue to decrease their θ_{es} throughout the LFT, and are cooler through the LFT than lower B_L profiles. Both tendencies of moisture and temperature in increasing B_L contribute to large differences in the subsaturation of the column in different B_L regimes as observed in Figure 3.4c and g.

Higher B_L profiles associated with higher rates of conditionally-averaged precipitation reflect parcels that are less diluted (less mixing) due to higher θ_e environments, as shown in Figure 3.4a,e. The raining (solid; precipitation rate ≥ 0.50 mm/h) and nonraining cases (dashed) in Figure 3.4 follow the trends of θ_e (Fig. 3.4a,e) and θ_{es} (Fig. 3.4b,f) noted above with increasing B_L—cooling and moistening of the LFT. In the case of precipitation in ARMBE, the boundary layer is cooler than the highest B_L bin and follows the trend of higher

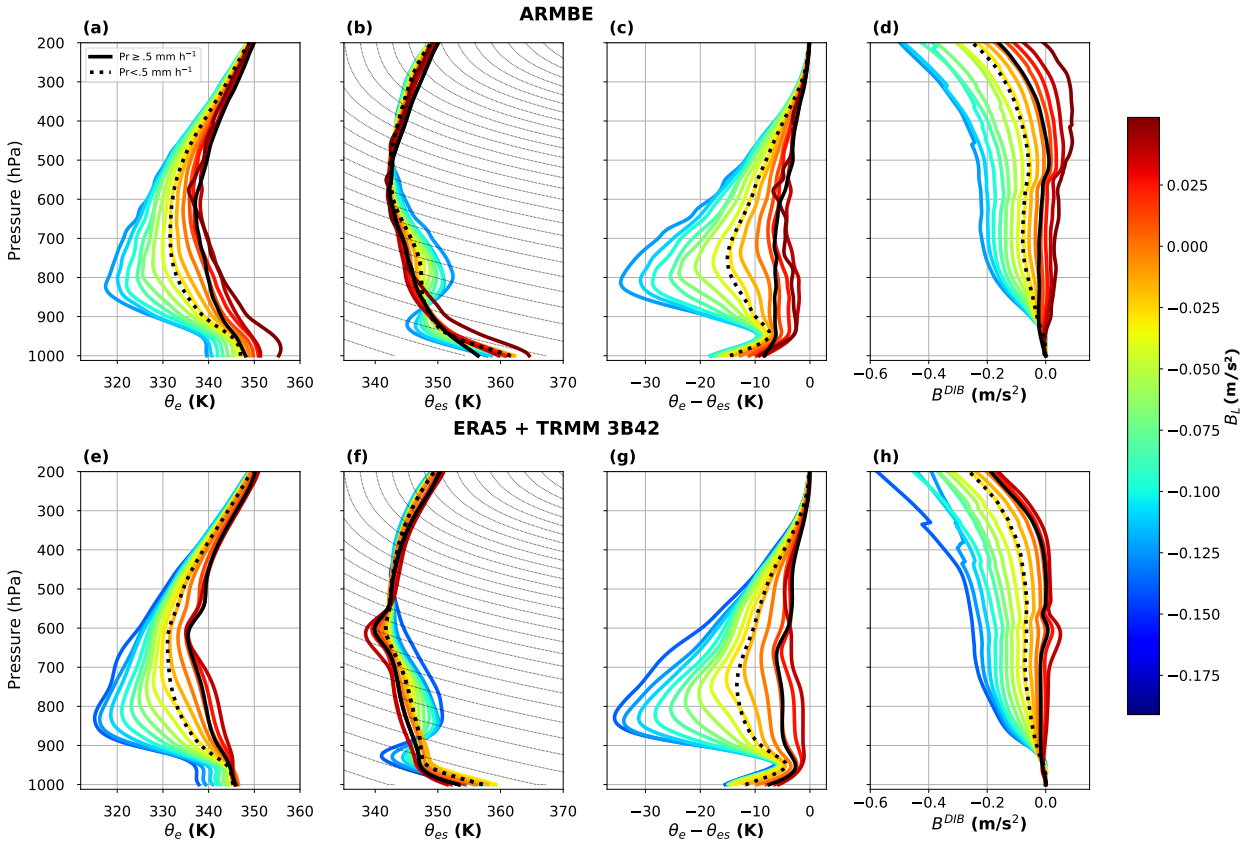

Figure 3.4: Conditional-average profiles of (a,e) θ_e on B_L, (b,f) θ_{es}, subsaturation (c,h), and buoyancy (d,i) for ARMBE (a-d) and ERA5 (e-i). Contours for θ_{es} are lines of constant potential temperature. Average over raining times (precipitation rate $\geq 0.5\text{mm}\,\text{h}^{-1}$) is represented by solid black lines, average over nonraining times is represented by dotted black line (precipitation rate $< 0.5\text{mm}\,\text{h}^{-1}$)

B_L through the rest of the column. The raining case in ERA5 does not display significant differences from the higher B_L bins across the environmental variables in Figure 3.4.

The convective boundary layer lapse rate can be inferred from Figure 3.4, a parcel travels along a line of constant potential temperature up to its LCL; departures from a line of constant potential temperature are analogous to departures from a dry adiabatic lapse rate. In the ARMBE θ_{es} case (Fig. 3.4b) the binned profiles follow the trajectory of a dry adiabat (contours) through the boundary layer, regardless of their B_L value. Only in the raining case (solid-black) does the boundary layer lapse rate deviate, starting from a cooler surface value with a shallower lapse rate than that predicted from a dry adiabat. The boundary layer follows a dry adiabat accross all B_L and non-raining and raining regimes for ERA5 (Fig. 3.4f). Below the LCL, in the raining regime, the temperature is set by convective downdrafts associated with evaporative cooling. Just above the LCL, the temperature profiles for both ARMBE and ERA5 show an inversion at low-B_L bins. The inversion is eroded away as B_L transitions into higher values, and the lapse rate becomes steeper.

An additional note should be made on the virtual effect, and its contribution across different B_L regimes. With sufficiently unsaturated LFT, water vapor differences between the boundary layer and the LFT are large, leading to an increased virtual effect on buoyancy in low-B_L regimes. Vapor virtual effect contributions are found to be larger on average during nonraining times than raining times as the LFT is more moist during raining times, permitting less dilution of ascending convective elements. Additionally, from Equation (3.5), the buoyancy effects from the condensate in the plume model nearly cancels out the contribution from water vapor. In the case in which the condensate cap is set greater than $1\,\mathrm{g\,kg^{-1}}$, the condensate contribution to buoyancy is greater than the vapor. Similar findings pointing to nonnegligible effects of condensate loading were explored in Xu and Randall (2001) and Bacmeister et al. (2012).

3.6 Intermodel differences in vertical thermodynamic structure

3.6.1 θ_e and θ_{es} vertical structures

Figure 3.5 displays the B_L-binned θ_{es} for the model cohort. With the exception of NASA-GISS, LFT θ_{es} decreases as B_L increases. A notable feature of Figure 3.5 are the peaks in the vertical structures of θ_{es} of the models. The peaks of the MIROC models are described in Chikira and Sugiyama (2010) and attributed to thermodynamic variations associated with different cumulus convection regimes: 850, 650, and 350 hPa corresponding to three major regimes of cumulus convection—trade cumulus, cumulus congestus, and cumulonimbus. The peaks of the θ_{es} profiles of some models (especially MIROC-E2SL and MIROC6 [Figure 3.5f and g]) in Figure 3.5l—which lie close to corresponding θ_e profile in Figure 3.6l—could represent large-scale clouds in the domain as described by Chikira and Sugiyama (2010). Another complication these peaks introduce are biases in our calculation of B_L. These peaks are not visible in observations and reanalysis products, nor is it a robust feature across models.

The behavior of the NASA-GISS model's θ_{es} in transitioning from low to high B_L indicates the model as an outlier among the cohort—observations and the majority of models exhibit LFT cooling while NASA-GISS shows warming (Fig 3.5c).

Figure 3.6 shows the θ_e profiles binned by B_L, similar to Figure 3.5. Observations and models show a similar trend in increasing B_L with respect to moistening: a lower tropospheric minimum between 900-800 hPa which begins to flatten and shift towards higher θ_e as B_L increases. An inversion is observed in θ_{es} profiles in the layer just above the ABL in Figs. 3.4b and f. This inversion has been previously observed using dropsondes from the Eastern Pacific in Raymond et al. (2003) and the authors note the inversion most likely arises from large-scale subsidence.

Spatial resolution considerations and their effect on the precipitation pickup for this model

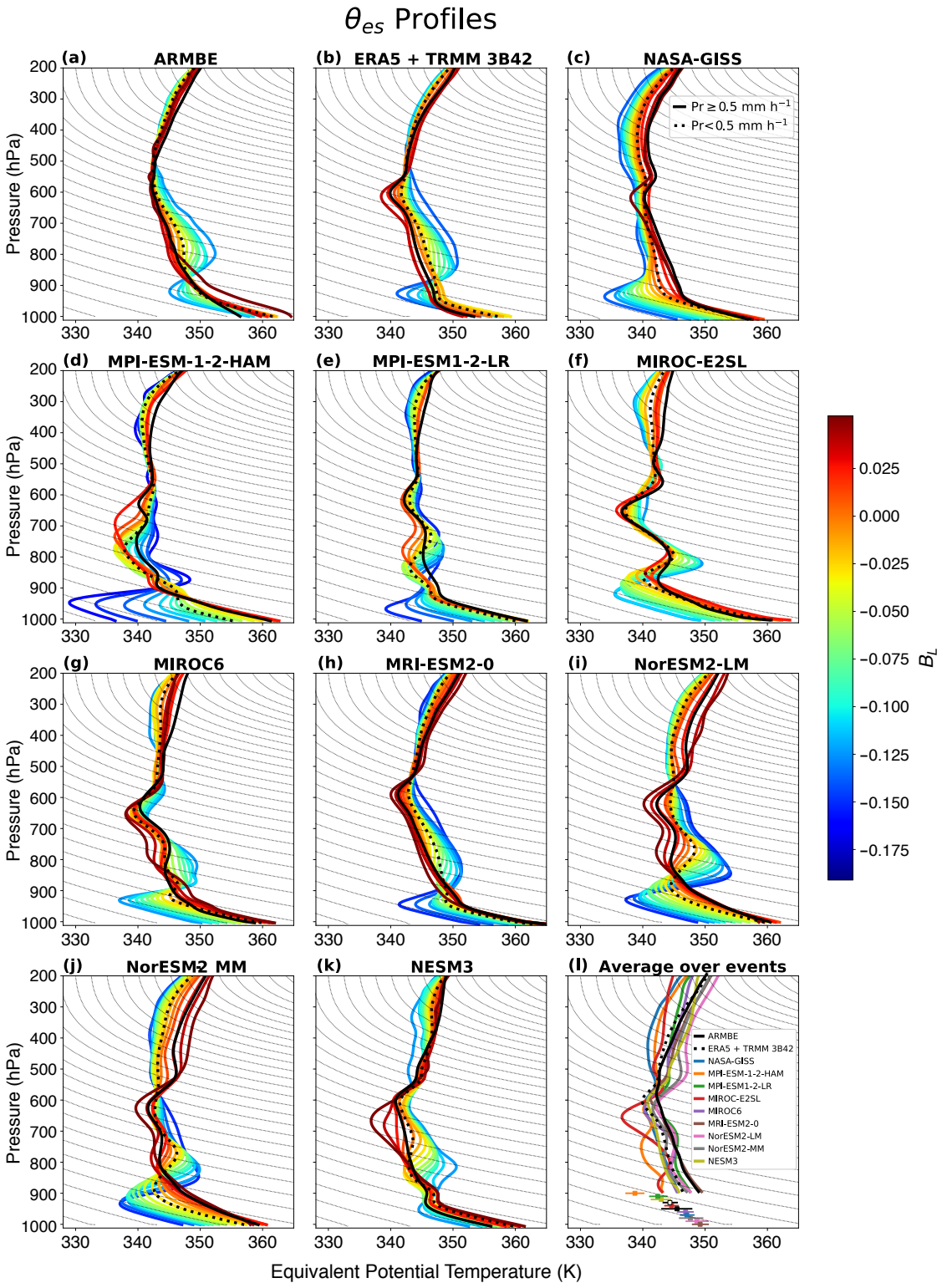

Figure 3.5: Binned profiles of θ_{es} according to B_L similar to Figure 3.4b and f. Solid black represents the average profile over raining times, while the dotted black line represent the average dry profile. Panel l shows the average θ_{es} over raining events of the cohort (black solid lines in each panel) and the average θ_e of the boundary layer during raining events (dots) with 25th to 75th confidence intervals.

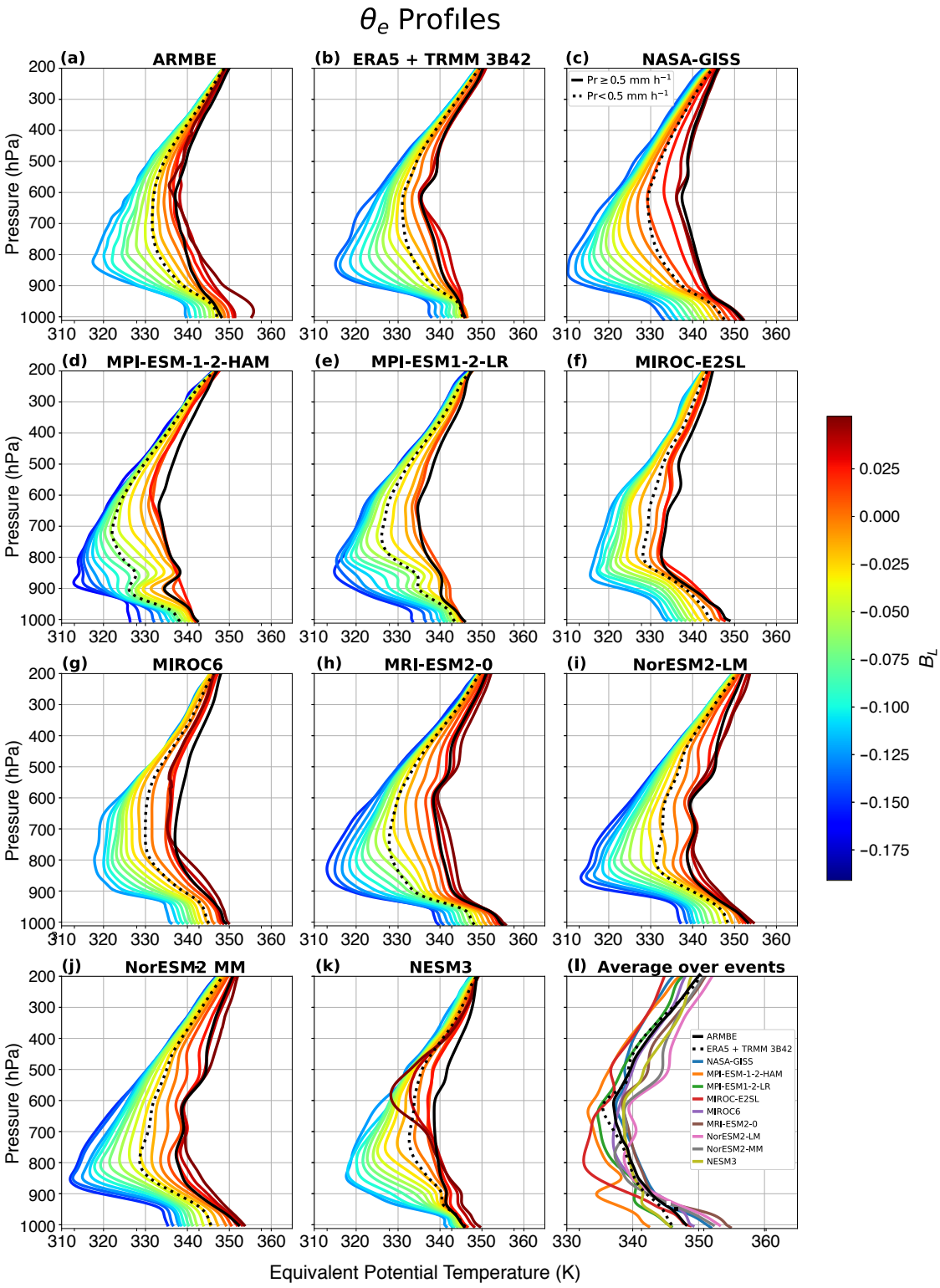

Figure 3.6: Similar to Figure 3.5 but for θ_e profiles

cohort were explored in Emmenegger et al. (2022) concluding that the convective transition statistics remain insensitive to spatial averaging. This insensitiviy to stems from the large spatial autocorrelation of of moisture and temperature (Abbott et al., 2016; Holloway and Neelin, 2010; Kuo et al., 2018).

3.6.2 Preconditioning of the convective environment

The trend in the θ_e profiles in Figure 3.6 where the LFT moistens as B_L increases is possibly a result of detrainment from shallow cumulus. The deepening of cumulus congestus in the LFT and its detrainment of moisture preconditions the free troposphere for convection, as entrainment of moister air in a rising plume does not dilute buoyancy as much (Waite and Khouider, 2010). Sensitivity tests in a cloud-resolving numerical experiment by Waite and Khouider (2010) found the moistening of the LFT to be the leading factor to the transition to deep convection, while the cooling of the troposhere and moistening of the ABL to be less important. An analysis by Hohenegger and Stevens (2013) found preconditioning by cumulus congestus to not be a dominant factor in the transition to deep cumulonimbus—the slow timescale of moistening by congestus is not consistent with the observed rapid transition to deep convection. Moreover, their results suggest moisture convergence to be the driving factor forced through mechanisms such as large-scale disturbances, waves, etc.

If the event is preceded by stratocumulus clouds, the cooling of the drizzle below the cloud base can lead to localized cooling and moistening below, destabilizing and moistening the subcloud layer, setting the environment to more favorable conditions for moist convection (Zuidema et al., 2017). In a scale analysis of contributions to plume buoyancy, Adames et al. (2021) found that largest source to be adiabatic moistening and cooling in the LFT.

Subsaturation, $\theta_e - \theta_{es}$, is perhaps the most important factor in the trajectory of a mixing plume, particularly the subsaturation of the LFT. This measure represents the additional moist entropy needed to bring the environment to saturation and determines the dilution of the rising plume Ahmed and Neelin (2018a). The convective transition statistics compiled

in subsaturation are displayed in the Supplemental Material, Figure S1. The conditional-average precipitation rate also exhibits a sharp pickup when conditioned on subsaturation of the environment (Figure S1). This illustrates the importance of this component of B_L, capturing the effect of entraining relatively moist versus relatively dry LFT air. Note that the subsaturation of the LFT takes two preconditioning effects (Zhang and Klein, 2010) into account—in addition to moisture, the variations in temperature measured by θ_{es} can contribute.

Adames et al. (2021) found the fast time-scale in which the cooling and moistening of the LFT occurs is consistent with inertio-gravity waves. With this in mind, a sufficiently moist column may be driven to saturation and convection. As noted in Raymond (1995), a marginally subsaturated column within a few Kelvin to zero are convective, as a transient gravity wave can lower the θ_{es} of the environment. Another large contribution to buoyancy generation and destabilization is vertical advection of moisture. Convection moistens the LFT if moistening from updraft detrainment exceeds drying from downdraft detrainment (Adames et al., 2021).

3.7 The Pseudo-entrainment diagnostic

Examination of observed and model θ_e and θ_{es} profiles in Fig. 3.2 suggested a decrease in θ_{es} through the lower free troposphere that is likely associated with entrainment interacting with the lower free tropospheric humidity. We now construct a pseudo-entrainment metric, in which bulk entrainment is estimated using θ_e and θ_{es} profiles.

3.7.1 Derivation

Assuming that the plume entrains environmental air from some combination of levels below, or that there exists some influence function (Ahmed and Neelin, 2018a; Schiro et al., 2018b),

the relationship of the estimated updraft θ_e has the form:

$$\theta_e^p = \int_p^{p_s} I(p, p`)\theta_e(p`)dp` \tag{3.6}$$

where

$$I(p, p`) = \frac{1}{M(p)}\frac{dM(p`)}{dp`}$$

is the influence function with M is the upward mass-flux. Differentiating (3.6) with respect to p gives the simple plume equation,

$$\frac{d\theta_e^p}{dp} = \epsilon\left[\theta_e - \theta_e^p\right] \tag{3.7}$$

where

$$\epsilon = \frac{1}{M(p)}\frac{dM(p)}{dp} = I(p, p)$$

is the entrainment coefficient and detrainment is neglected.

To a first approximation using the zero buoyancy assumption (Singh and O'Gorman, 2013) and taking $\theta_{es} = \theta_e^p$ in (4.3.1) gives:

$$\frac{d\theta_e^p}{dp} = \epsilon\left[\theta_e - \theta_{es}\right]. \tag{3.8}$$

The right hand side of (3.8) is the environmental subsaturation, a measure of environmental dryness. Assuming now that the entrainment is constant through the LFT and integrating (3.8) from the top of the boundary layer (900 hPa) to 600 hPa gives:

$$\epsilon \approx \tilde{\epsilon} = \frac{\theta_{es}^{600} - \theta_e^{BL}}{\langle\theta_e^-\rangle} \tag{3.9}$$

where $\tilde{\epsilon}$ is termed the pseudo-entrainment, a bulk measure of entrainment in the LFT and $\langle\theta_e^-\rangle$ is the vertically integrated subsaturation from 900 to 600 hPa. In deriving (3.9), we have assumed that the plume leaves the boundary layer with the average θ_e of the boundary layer,

θ_e^{BL}. At 600 hPa, the plume θ_e is assumed equal to the environmental saturated θ_e ($=\theta_{es}^{600}$). The upper limit of the integral in (3.9) is restricted to 600 hPa for the following reasons: (i) the plume properties below the freezing layer are found to have the strongest relationship to precipitation (Ahmed and Neelin, 2021b; Holloway and Neelin, 2009b; Schiro et al., 2018b) and (ii) 600 hPa lies below the tropical freezing layer, so ice transformation effects can be neglected when formulating (3.9). The pseudoentrainment diagnostic is a function of the environmental stability—the numerator in (3.9)—and subsaturation—the denominator in (3.9).

A similar derivation for a Zero-Buoyancy Entraining Plume Model was used in Singh and O'Gorman (2013); in their model, the entrainment rate is prescribed as the $\epsilon(z) = \hat{\epsilon}/z$ case (the same scheme used in our Deep-Inflow B calculations) where $\hat{\epsilon}$ is a constant. Deep-Inflow B considerations can be applied to Equation 3.9, by substituting $\epsilon = \hat{\epsilon}(p - p_0)^{-1}$ which applies weighting to the isobaric layers of integrated subsaturation profile over the entraining layer. The main results remain unchanged. For simplicity, we stick to our formulation in 3.9.

We wish to emphasize that pseudo-entrainment and entrainment in a model convective scheme are not interchangeable. First, the pseudo-entrainment similarity to entrainment in (3.8) applies in the limit of small buoyancy, which is often violated at short timescales, hence the choice to diagnose the pseudo-entrainment from the average conditions over raining events. Second, models often produce some deep convection at the grid scale (e.g., **?**). The pseudo-entrainment includes effects of such events, for which entrainment is by the flow into the grid cell from neighboring non-convecting grid cells, as elaborated below. Overall the large-scale pseudo-entrainment measure aims to capture the aggregate effect of an ensemble of convective entities originating at any level in the LFT (below 600 hPa), not the entrainment rate that would apply during a particular convective event or in a specific parameterization. In the following section, we will be applying the pseudo-entrainment estimation to the environmental profiles at the Nauru site.

3.7.2 Model diagnosis

The pseudo-entrainment diagnostic is now applied to constrain climate model entrainment-stability tradeoffs. For this we use nine CMIP6 models along with six CAM5 parameter perturbation runs. Note that (3.9) is only applicable during convecting times since it is derived from an entraining plume equation (3.6). We therefore estimate all the environmental θ_e-based variables (θ_e^{BL}, θ_{es}^{600} and $\langle\theta_e^-\rangle$) as averages during times in which the precipitation rate exceeds $0.5\,\mathrm{mm\,h^{-1}}$. Figure 3.7 shows θ_e^{BL} and the θ_{es}^{600} of each model computed this way, along with comparisons to ARMBE and ERA5 data. Confidence ellipses are computed from 1000 bootstrap realizations of the average raining profile (sampled with replacement from the raining events in each data set), using the covariance matrix to fit an ellipse that would contain 95% of the samples if the distribution were Gaussian. For models and ERA5, the ellipses are smaller than the symbols due to large number of soundings, but may be seen for ARMBE and the CAM5 runs due to smaller sample size. A related measure for regional representativeness is discussed below.

Under QE assumptions, the instability measure, $\theta_e^{BL} - \theta_{es}^{600}$, may be regarded as a "plume lapse rate" relative to that of a non-entraining parcel through the LFT if $\theta_e^{BL} \sim \theta_{es}$ at the top of the boundary layer (i.e. the level of free convection is near 900 hPa). We use this term for brevity, noting that it would be zero for an environmental profile neutral to nonentraining, reversible plumes. The DIB plume in Figure 3.2 (θ_e^{DIB}; red curve) is approximated by the average of levels below; its θ_e at the top of the boundary layer (900 hPa) is equivalent to the θ_e^{BL} value displayed in Figure 3.7. At the top of the boundary layer, the DIB plume lies close to its environmental θ_{es} for NASA-GISS, the MIROC models, MRI-ESM2-0, and the NorESM2 models (comparison of red to solid black curves in Fig. 3.2c,f,g,h,i,j). ARMBE, ERA5, the MPI models, and NESM3 environmental θ_{es} is more similar to the NMX plume at the top of the boundary layer (comparison of orange to black curve in Fig. 3.2a,b,d,e,k). The estimation of the boundary layer θ_e depends on boundary layer mixing assumptions, which may be different among model convective schemes (and varying in observations). Surface

boundary layer values for those models which appear to experience less mixing out of the boundary are included in Fig. 3.7 (open circles) for reference.

As an indicator of how well values at Nauru represent the region, we also include an ellipse, similar to a 95% confidence ellipse, for the for the ERA5 Western Pacific (5°S-5 °N, 100°E - 180 °E) averaged profiles over raining times in 2006. This ellipse is fit such that it contains 95% of the samples from the distribution over this region. In addition to sampling error (relatively small) it includes variations due to point to point differences within the region. For the ERA5 Western Pacific, this ellipse is elongated in a direction corresponding to constant lapse rate, i.e., θ_e^{BL} increases are aligned with θ_{es}^{600} increases, parallel to the one-to-one line in Figure 3.7.

Models which use the Tiedtke-type convective parmeterization—which use moisture convergence in the convective trigger—the MPI models and NESM3, are more stable than observations, while other models in the cohort—the majority of which use a CAPE-based triggers and closures—look to exhibit less stability (convective parametrization assumptions are listed in Table 3.1).

The total dilution of the bulk plume is characterized by $\theta_e^{BL} - \theta_{es}^{600}$, often discussed as an instability measure since positive values would yield convective instability for nonentraining plume— noting that here the interpretation is as a profile that is typically only marginally unstable to entraining plumes. This measure is similar to the Deep Convective Inhibition quantity introduced in Raymond et al. (2003) where the authors showed a correlation between larger differences between boundary layer moist entropy and an intermediate layer (810 - 830 hPa) and deep convection.

The environmental subsaturation in the intermediate layer plays a defining role and acts with entrainment in determining the degree to which the bulk plume is diluted in its ascent. Consider the scenario where the entrainment among a model cohort is fixed. In our formulation, if the stability differs, the conclusion is that the subsaturation of the environments differ—larger (smaller) lapse rates are the result of a more (less) subsaturated

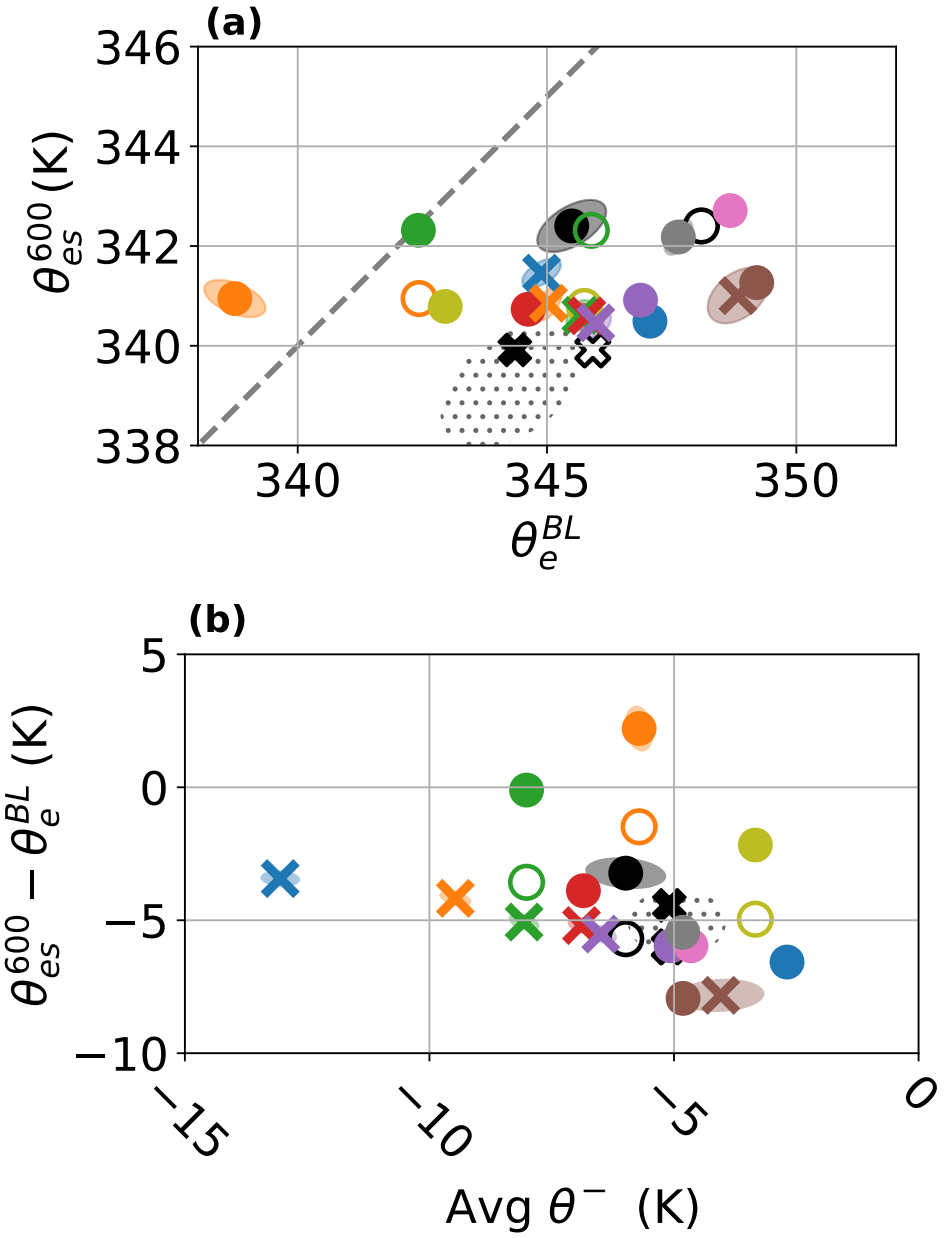
(a)
346
344
342
340
338
340
345
350
θ_{es}^{600} (K)
θ_e^{BL}
(b)
5
0
−5
−10
−15
−10
−5
0
$\theta_{es}^{600} - \theta_e^{BL}$ (K)
Avg θ^- (K)
ERA5 W. Pac. 95th
ARMBE
ARMBE sfc
ERA5 + TRMM 3B42
ERA5 + TRMM 3B42 sfc
NASA-GISS
MPI-ESM-1-2-HAM
MPI-ESM-1-2-HAM sfc
MPI-ESM1-2-LR
MPI-ESM1-2-LR sfc
MIROC-E2SL
MIROC6
MRI-ESM2-0
NorESM2-LM
NorESM2-MM
NESM3
NESM3 sfc
cam5_dmpdz=0.25
cam5_dmpdz=0.5
cam5_dmpdz=0.75
cam5_dmpdz=1.0
cam5_dmpdz=1.25
cam5_zm_off

Figure 3.7: (a) Average atmospheric boundary layer (ABL defined as 1000 - 900 hPa; closed-markers) with surface θ_e values (open-markers) plotted against the θ_{es} at the 600 hPa level of the average raining profiles, the one-to-one line is plotted as a reference (gray-dashed) and (b) the average LFT subsaturation (900 - 600 hPa) during raining times plotted against the theoretical plume lapse rate ($\theta_{es}^{600} - \theta_e^{BL}$; subtracting the two quantities plotted in (a)) of the average raining profile. Quantities are calculated from the profiles displayed in Figure 3.2. Shaded regions are 95% confidence ellipses (in most cases these are smaller than the marker) which contain 95% of the samples from the underlying Gaussian distribution. Dotted region indicates the Western Pacific regional spread in ERA5 (see text). CAM5 perturbed-physics experiments are included with varying entrainment rates, dmpdz, of 0.25 km^{-1}, 0.50 km^{-1}, 0.75 km^{-1}, 1.0 km^{-1} (control), 1.25 km^{-1}, and a case where the subgrid convective parameterization is turned off (zm_off) as colored x markers.

environment due to the incorporation of drier (moister) air into the plume. Figure 3.7b shows the average subsaturation of the intermediate layer (900-600 hPa) to the lapse rate of the environment. The subsaturation-instability relationship of the model cohort is much more complicated than this as observed in Figure 3.7b—models exhibit varying degrees of subsaturation and lapse rates. We can tie these two environmental factors together and derive a single quantitative diagnostic, the 'pseudo-entrainment' diagnostic, as an estimator of the bulk entrainment rate. The pseudo-entrainment diagnostic is, more succinctly, the ratio of the instability to the subsaturation of a raining column.

The pseudo-entrainment formulation illustrates the trade-off between the subsaturation and the lapse rate; in order for a model with a high-bias (low) prescribed entrainment to replicate the observed lapse rate, it must compensate with higher (lower) subsaturation. This trade-off has been explored in previous studies: (Kim et al., 2013, 2012; Mapes and Neale, 2011; **?**), increasing entrainment increases the influence of the ambient subsaturation at the expense of the LFT stratification. Buoyancy-based cumulus parameterizations (those with considerations of CAPE or cloud-work) adjust precipitating environments to near-zero buoyancy measures; the quasi-equilibrium (QE) state in models with low entrainment is characterized by neutral lapse rates while the QE state of models with high-entrainment is LFT saturation (**?**).

We calculate $\tilde{\epsilon}$ with the average profile over raining times for each model. Figure 3.8

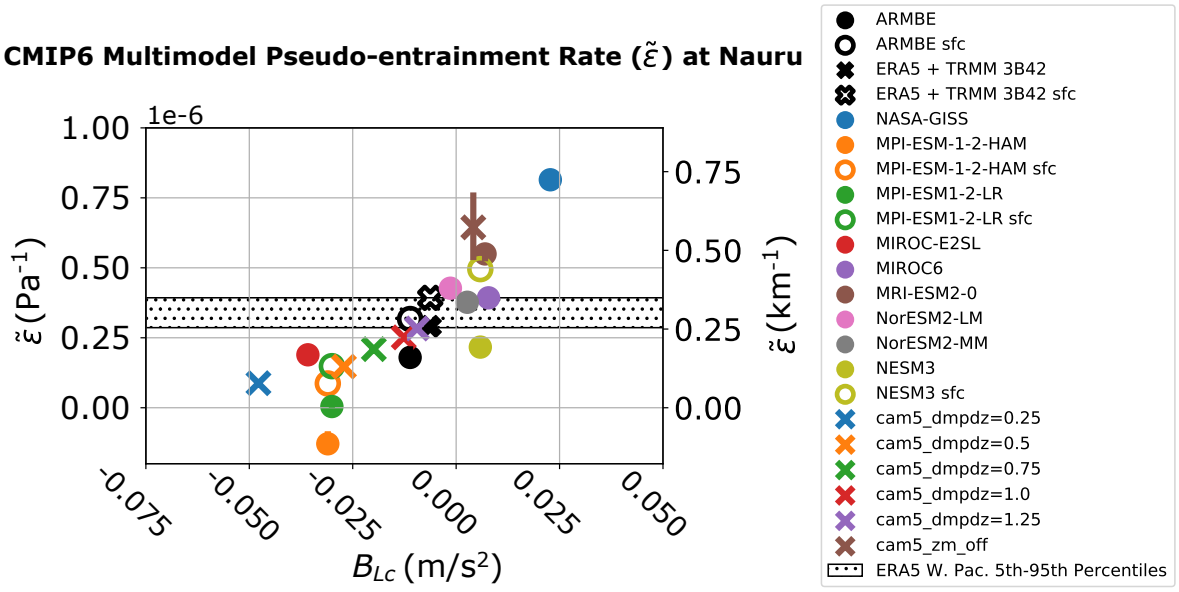

Figure 3.8: The pseudo-entrainment rate, $\tilde{\epsilon}$ plotted against the critical value of the B_L pickup. Vertical bars show the 5th-95th confidence interval, but are only visible for CAM-ZM-OFF. The dotted area shows 5th-95th range from the Western Pacific, similar to Fig. 7, i.e., a measure of regional variations in the pseudo-entrainment.

shows the results of the pseudo-entrainment rate, plotted against the critical value of the precipitation pickup, B_{Lc}, the B_L value where the precipitation pickup begins to increase rapidly.

A near linear relationship is observed between B_{Lc} and $\tilde{\epsilon}$, models with a higher pseudo-entrainment tend to exhibit a pickup at higher B_L. The pseudoentrainment estimation is able to discern between those environments resulting from an increasing entrainment parameter within a convective scheme—increasing the entrainment rate in the CAM5 model leads to a higher $\tilde{\epsilon}$ and a higher-B_L pickup (color x-markers in Fig. 3.8). As a model entrainment parameter is decreased, the threshold for the convective trigger (such as CAPE) is met in drier environments, and models with lower entrainment have drier and warmer columns during convection. We underline that the pseudo-entrainment estimator is for an overall effect of entrainment. This could include contributions from more than one entrainment scheme if present; more importantly, when grid-scale convection occurs in the model, which is not infrequent, the overall entrainment includes grid scale inflow with neighboring cells

serving as the environment. This may be seen with the ZM-OFF experiment, for which deep convection happens entirely at the grid scale and which thus has a high pseudo-entrainment.

The pseudoentrainment diagnostic, being a function of temperature lapse rate and subsaturation, presents a contraint on model behavior if entrainment is not correctly represented. For instance, if a model's convective scheme entrains too heavily, the bulk plume dilutes quickly, and this is reflected in the environmental θ_{es} as a steeper lapse rate and a higher measure of instability. In this high (low) entrainment case, to counter the production of large and too unstable (small and too stable) lapse rates, the bulk plume would need to mix with less (more) subsaturated air, or the column would need to moisten to a sufficient degree.

Model moisture biases are often framed with the consideration of the convective trigger (e.g. models with lower entrainment may reach their threshold for convection in drier environments Ahmed and Neelin (2021a)). The components of the pseudoentrainment diagnostic—the instability and subsaturation—provide another, perhaps more consequential, view of how entrainment biases affect environmental behavior during convective events. Models with pseudo-entrainment rates that are too large must produce a higher moisture bias to accurately represent the stability of the environment.

This is shown in Figure 3.9, which displays the pseudo-entrainment against the instability of the observations and model cohort. The reference line (black-dotted) shows the values of pseudo-entrainment and the instability needed to replicate the subsaturation of the ARMBE data—higher $\tilde{\epsilon}$ implies a higher stability if the subsaturation is constant. Models which lie to the right (left) of the reference line have a high (low) moisture bias. Most notably in Figure 3.9, NASA-GISS model must have a high moisture bias, given that its pseudo-entrainment is so large. A major implication of Figure 3.9 is that if NASA-GISS moisture were not compensating for its high $\tilde{\epsilon}$, its instability would be too large compared to observations (-15 K).

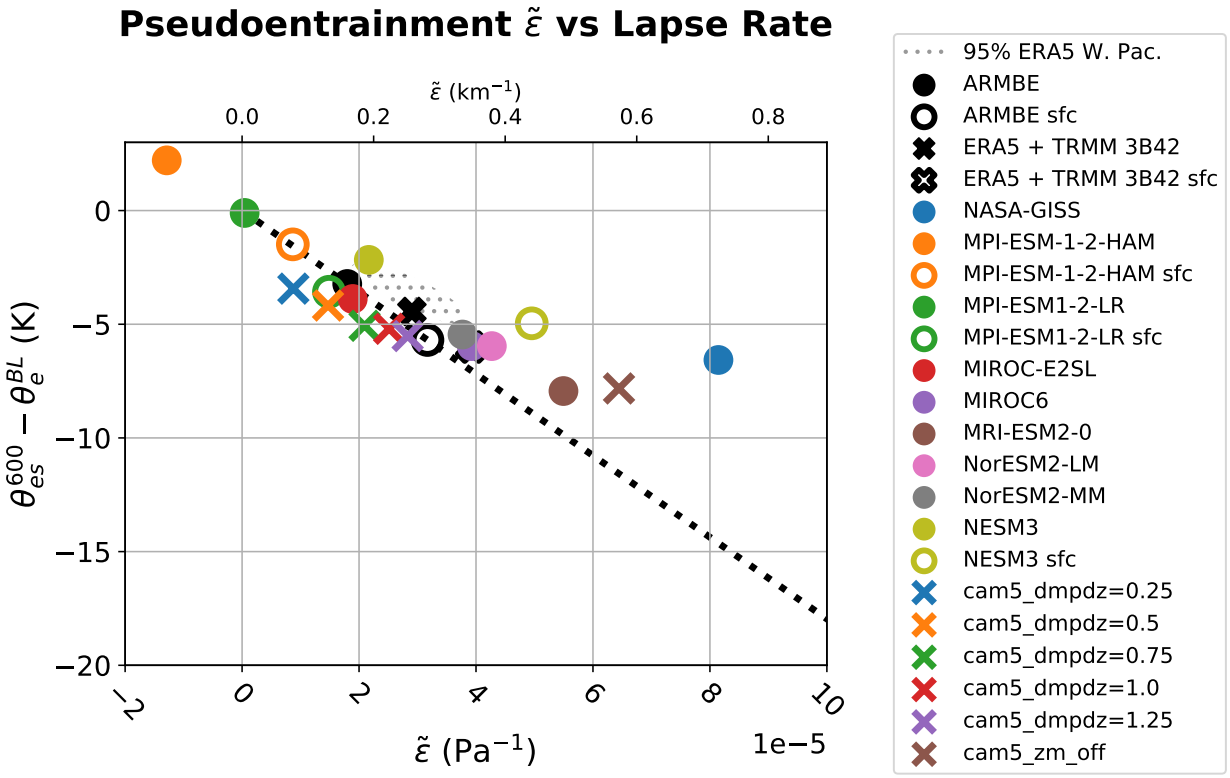

Figure 3.9: The pseudo-entrainment, $\tilde{\epsilon}$, plotted against the theoretical plume lapse rate (calculated from the average profiles during raining times). The reference line refers to the ARMBE LFT subsaturation; models which lie to the right (left) of this line have a moisture (dry) bias for their given lapse rate. Dotted region shows Western Pacific regional variations in ERA5 as in Figs. 7 and 8.

3.8 Conclusions

A simple plume model based on the conservation of equivalent potential temperature, θ_e, allows for estimations of instability similar to measures of CAPE from snapshots of vertical thermodynamic structures. The θ_e definition of buoyancy provides a favorable framework for tropical climatologies that are shaped by moist convection driven by the onset of conditional instability. The presence of a rapid increase in precipitation conditioned on heavily-entraining plume buoyancy, $\langle P \rangle$, across the cohort of CMIP6 models indicates a high degree of correlation between heavy lower-free tropospheric (LFT) mixing and the onset of convection in model convective schemes. Binning the thermodynamic environments by a theoretical value of LFT buoyancy, B_L, shows the environment generates buoyancy through the combination of LFT cooling and moistening. Most models qualitatively capture this cooling and moistening behavior, the exception being the NASA-GISS model which warms in addition to moistening. Contrary to previous work which points to insufficient sensitivity of the prior (CMIP5) generation of GCMs to LFT moisture (Rushley et al., 2018), the proximity of the critical values of $\langle P \rangle$ between CMIP6 models and observations suggests the majority of CMIP6 models perform fairly well in their sensitivity to environmental moisture through the mixing process.

Emmenegger et al. (2022) showed that a cohort of CMIP6 models perform relatively well in replicating the statistics of column-integrated measures such as column relative humidity (CRH) and column water vapor and precipitation. The analysis presented here dissects the vertical thermodynamic structures of the model cohort, concluding that models perform well with respect to CRH but at the expense of their climatological stability due to the constraint presented by inaccurate representation of the entrainment process. A few models in this cohort, NASA-GISS and MRI-ESM2-0, are shown to exhibit environments consistent with too much entrainment in their convective schemes and must compensate with a wetter column during convection in order to keep their column at a realistic level of stability (as determined by the difference between θ_{es} of the LFT and θ_e of the boundary layer).

These conclusions are reached through the derivation of the pseudo-entrainment diagnostic, an estimation of an entrainment rate undergone by a bulk plume between the boundary layer and the freezing level. The pseudo-entrainment is the ratio of the bulk plume lapse rate (the expected change a parcel undergoes in its ascent, estimated by difference of the freezing level θ_{es} and boundary layer θ_e) and the integrated subsaturation (the expected properties of the air the parcel mixes with) of the average raining environment. It is shown in Figure 3.8 that the pseuedo-entrainment serves as a reasonable indicator of the critical value of the pickup, with a higher pseudo-entrainment diagnostic predicting pickup at a higher B_L value. These results are consistent with our postulate that larger measures of apparent convective instability on average during raining events are a consequence of too heavy entrainment. In Section 3.7, the consequences of the incorrect treatment of the entrainment process in the climatological structures of humidity and instability are assessed. Figure 3.9 displays the constraint in which CWV and CRH statistics may be accurately represented by models with incorrect entrainment, but only so at the expense of climatological instability—models with higher (lower) entrainment must accommodate with higher (lower) climatological instability to accurately represent environmental moisture. In the case that entrainment is too high, models must sufficiently saturate to keep climatological instability at some reasonable range to that of observations. Such is the case for the NASA-GISS model; it shows a significantly higher measure of pseudo-entrainment, and to keep its stability within a reasonable range of observations, it compensates with higher climatological moisture. The pseudoentrainment diagnostic shows models that use variants of the Tiedtke convective scheme and low entrainment runs of CAM5 display environments consistent with small entrainment—small plume lapse rates and larger subsaturation which lead to early pickups in B_L. Furthermore, some models that behave reasonably in terms of bulk entrainment effects exhibit variations in vertical structure even for averages over raining events that do not correspond to observations. We postulate that the factors of the pseudo-entrainment diagnostic analyzed here likely shape features of CMIP6 warming scenario experiments,

given the delicate balance between lapse-rate (instability) and water vapor (subsaturation) feedbacks which shape the structure of warming (Bao et al., 2021).

3.9 Supplemental Material

Equivalent Potential Temperature Definition of Buoyancy

The following derivation closely resembles that of Adames et al. (2021) Appendix A, but uses a constant reference in it θ_{es} approximation. A more detailed derivation of Equivalent Potential Temperature and parcel buoyancy may be found in Raymond (1994) Section 2 - 2.1.

We begin with the approximation to virtual temperature, T_v,

$$T_v \approx (1 + 0.61q_v - q_c)T$$

where T is the temperature, and q_v and q_c are the vapor and condensate mixing ratios respectively. We write a small change in T_v as

$$\delta T_v \approx (1 + 0.61q_v - q_c)\delta T + (0.61\delta q_v - \delta q_c)T \tag{3.10}$$

We can rewrite the virtual temperature definition of buoyancy,

$$B = g\left[\frac{\delta T_v}{T_v}\right]$$

using 3.10 as

$$B = g\left[\frac{\delta T}{T} + \frac{0.61\delta q_v - \delta q_c}{1 + 0.61q_v - q_c}\right] \tag{3.11}$$

With $0.61q_v - q_c << 1$, $(1 + 0.61q_v - q_c)^{-1} \approx 1 - 0.61q_v + q_c$, the expression for buoyancy is simplified to

$$B = g\left[\frac{\delta T}{T} + 0.61\delta q_v - \delta q_c\right] \tag{3.12}$$

where second-order terms have been dropped.

We will rewrite the fractional temperature difference of B in terms of a equivalent

saturation potential temperature, θ_{es}, a variable conserved in a saturated parcel with respect to moist adiabatic motions. Consider the approximate definition of equivalent potential temperature, θ_{es}:

$$\theta_{es} = \theta \exp\left[\frac{Lq_s}{c_p T_0}\right]$$

where θ is the potential temperature, L is the latent heat of vaporization, q_s is the saturation mixing ratio, c_p is the specific heat capacity of dry air, and T_0 is a reference temperature.

For simplicity, define θ_{es} as functional:

$$\theta_{es} \equiv \theta_{es}[\theta(p,T), \xi(q_s(T); T_0)] = \theta\xi$$

where

$$\xi = \exp\left[\frac{Lq_s}{c_p T_0}\right]$$

.

Differentiating,

$$\delta\theta_{es} = \frac{\partial\theta_{es}}{\partial\theta}\frac{\partial\theta}{\partial T}\delta T + \frac{\partial\theta_{es}}{\partial\xi}\frac{d\xi}{dq_s}\frac{dq_s}{dT}\delta T$$

$$= \frac{\xi\theta}{T}\delta T + \theta\xi\frac{L}{c_p T_0}\frac{Lq_s}{R_v T^2}\delta T$$

then,

$$\frac{\delta\theta es}{\theta_{es}} = \frac{\delta T}{T}\left(1 + \frac{L^2 q_s}{c_p R_v T_0 T}\right)$$

$$\frac{\delta\theta es}{\kappa\theta_{es}} = \frac{\delta T}{T} \tag{3.13}$$

Using (3.13) in the virtual temperature definition of buoyancy, (3.12) gives the final form of buoyancy used in the manuscript,

$$B = g\left[\frac{\delta\theta es}{\kappa\theta_{es}} + 0.61\delta q_v - \delta q_c\right]$$

Convective onset statistics as a function of LFT subsaturation

Figure 3.S1 is provided for comparison to Fig. 3 in the main text which shows convective onset statistics as a function of B_L. Similarities between these figures illustrate the importance of lower free troposphere (LFT) subsaturation to the convective onset.

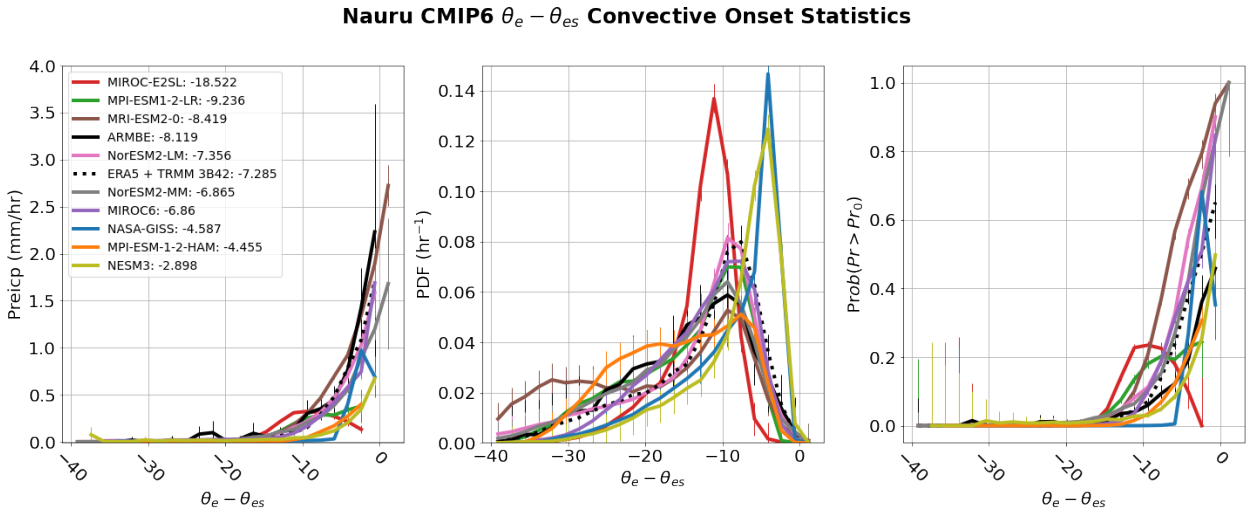

Figure 3.S1: Similar to Figure 3 of the main text but statistics are conditioned on average LFT subsaturation, $\theta_e - \theta_{es}$ averaged over 900 - 750 hPa.

Chapter 4

Assessing relative contributions of instability and lower-free tropospheric moisture to precipitation onset in obervations and reanalysis

Abstract

In the bulk plume framework of convection, the convective updraft is initiated by warm and moist air rising out from the boundary layer into the free troposphere. The convective entity mixes with the ambient air in its ascent, diluting its buoyancy and bringing qualities of the plume, such as its humidity and temperature, closer to those of the environment. Framing plume buoyancy as a combination of these factors poses buoyancy as a weighting between undilute instability (a CAPE-like quantity, C_L) and the state of the ambient environmental air (a subsaturation-like quantity, S_L). The weighting between these quantities is determined by the mixing rate—more mixing necessitates more humid ambient air or a stronger initial instability for the updraft to remain buoyant. Previous studies seek a value of this weighting that gives a strong relationship of this estimate for buoyancy to precipitation, finding which combination of C_L and S_L most accurately describes increases in precipitation (Ahmed and Neelin, 2021a) or the precipitating state (Emmenegger et al., 2024). However, the evolution of convection and its feedback to the environment complicates the estimations of this weighting. Using a combination of reanalysis and observational products (ARMBE, COSMIC2, and ERA5) we distinguish between aspects of the convective time evolution, showing that buoyancy with C_L and S_L contributions evolves into a state with subsaturation components later.

4.1 Introduction

Biases in the moisture-precipitation relationship are major contributors to uncertainty in future projections of climate under warming. The variance of climatological buoyancy is determined by the slow timescale at which instability is generated on the large scale and its fast consumption through local-scale convection and precipitation. The point at which convection is initiated, represented by a convective trigger function in GCMs, controls the mode of the distribution of buoyancy, referred to as the critical point (Adames et al., 2021;

Ahmed and Neelin, 2018a; Emmenegger et al., 2024). If the convective onset is ill-constrained, it can lead to biases in the radiative equilibrium state and its associated feedbacks (Bao et al., 2021; Yang and Seidel, 2020).

In the bulk plume framework of convection, buoyancy is represented by an entraining plume which originates in the boundary layer and mixes with ambient environmental air in its ascent. The mixing process dilutes the initial updraft buoyancy and brings its temperature and moisture closer to that of the environment. Utilizing the precipitation-buoyancy relationship with empirical mixing schemes permits estimates for constraining mixing rates in GCMs as in Ahmed and Neelin (2021a) and Emmenegger et al. (2024).

There is much room for improvement on these estimations. Additional effects of vapor buoyancy and condensate loading have been shown to have significant effects on buoyancy (Bacmeister et al., 2012; Xu and Randall, 2001; Yang and Seidel, 2020). Additionally, the time evolution of the convection and its feedback on the environment can bias these estimates. We begin by introducing our data from which we combine theoretical aspects of convection with empirical data to estimate the relative importance of convective available potential energy (CAPE) and subsaturation (similar to the relative humidity of an atmospheric column) to initiate convective updraft in section 4.2. Using a mass-flux profile informed by observations (Schiro et al., 2018b), we recast lower-free tropospheric (LFT) buoyancy as a weighting of CAPE-like and subsaturation-like factors, while retaining microphysical effects of vapor and condensate in section 4.3.1. The time evolution of convection is explored in 4.3.3, where we identify the feedback of convection on the environment. In section 4.3.4, we introduce methods to estimate the relative weighting of the factors.

4.2 Data

Surface precipitation rate and vertical profiles of humidity and temperature from the ARM Best Estimate dataset (ARMBE; Xie et al., 2010), an hourly integrated product assembled

from various in-situ ARM measurements at two tropical western pacific sites, Manus and Nauru are used. The hourly European Center for Medium-Range Weather Forecasts Reanalysis 5th Generation (ERA5; Hersbach et al., 2020) reanalysis product across the tropical pacific (15°S - 15 °N, 155°E - 95 °W) for the year 2008 is included. Formosat-7 Constellation Observing System for Meteorology, Ionosphere, and Climate (COSMIC-2) between October 2019 and July 2022 radio provides a novel dataset, producing 5,000 high resolution vertical profiles per day in the subtropics and tropics. We extract tropical information from COSMIC-2 (within 15°S - 15 °N, 155°E - 95 °W) and augment it with the nearest 30-min Global Precipitation Measurement (GPM) Integrated Merged (IMERG) precipitation products (Tan et al., 2017).

4.3 Recasting buoyancy as a weighting between CAPE-like and subsat-like quantities

The equivalent potential definition of buoyancy that includes contributions from the virtual effect and condensate is,

$$B = g\left[\frac{\delta\theta_{es}}{\kappa\theta_{es}} + \alpha_v\delta q_v - \alpha_c\delta q_c\right] \tag{4.1}$$

where θ_{es} is saturated equivalent potential temperature, δ represents the difference between the plume and the environment, with θ_{es}^{p} that of the parcel and θ_{es} without the superscript is that of the environment; q_v is the water vapor mixing ratio, q_c the condensate mixing ratio, and g is the acceleration due to gravity. The second and third terms represent the contributions from 1) the water vapor effect on density (sometimes called the virtual effect, incorporated in the definition of virtual temperature) and 2) condensate loading. The coefficients, α_v and α_c in front of these terms represent parameters in which the virtual effect can be turned on or off (where α_v takes on the value of 0.61, or 0 to omit this effect) and the condensate fallout ratio, where α_c takes on a value between 0 (all condensate falls out of the plume) and 1 (no

Variable	Description	Value	Units
g	Acceleration due to gravity	9.8	$\mathrm{m\,s^{-2}}$
L	Latent heat of vaporization	2.5	$\times 10^6 \mathrm{J\,kg^{-1}}$
c_p	Specific heat capacity of dry air	1005	$\mathrm{J\,kg^{-1}\,K^{-1}}$
R_v	Gas constant for water vapor	461	$\mathrm{J\,kg^{-1}\,K^{-1}}$
T_0	Reference temperature	300	K
p_0	Reference pressure	1000	hPa

Table 4.1: Values of constant used for the buoyancy calculation in Equation (3.1)

condensate falls out of the plume). The factor

$$\kappa = 1 + \frac{L^2 q_s}{c_p R_v T_0 T} \tag{4.2}$$

arises when converting from the temperature-based form of buoyancy (Adames et al., 2021; Raymond, 1994). In Equation (4.2), L is the latent heat of vaporization, q_s is the saturation specific humidity of the environment, c_p is the specific heat of dry air, R_v is the gas constant of water vapor, and T_0 is a constant reference temperature.

This definition of buoyancy is the exact one used in Emmenegger et al. (2024) and is similar to that used in Raymond (1994) and Adames et al. (2021). Values of the constants used in this study are displayed in Table 4.1. The advantage of using equivalent potential temperature, θ_e, is that it is approximately conserved in both moist and dry adiabatic reversible processes and is more feasible to construct analytic formulations for plume quantities as we will do in the following section.

4.3.1 Derivation

We begin with the simple plume equation for some convserved quantity A with superscript p for 'plume,'

$$\frac{\partial A^p}{\partial p} = \epsilon \left[A - A^p \right] \tag{4.3}$$

where ϵ is the mixing, or entrainment rate. Noting that $\epsilon = M^{-1}\frac{dM}{dp}$ where M is the mass flux, we can apply mass flux cases to solve (4.3.1). The solution to (4.3.1) is

$$A^p(p) = M(p)^{-1} \int_{p_s}^{p} \frac{dM}{dp`} A dp`$$

where we have assumed that $M = 0$ at p_s (Holloway and Neelin, 2009b). Empirical estimates of mass-flux associated with deep convection indicate a roughly linear increase in the lower troposphere (Schiro et al., 2018b). For purposes here, distinguishing between effects from air entrained in the lower free troposphere compared to contributions to the plume from the boundary layer, we represent the mass-flux as the following piecewise formulation

$$M(p; m_1, m_2) = \begin{cases} m_1(p - p_s) & p_B < p \leq p_s \\ m_2(p - p_B) + m_1(p_B - p_s) & p_L < p \leq p_B \end{cases}$$

where $p_B = 900$hPa and $p_L = 600$hPa as the layer boundaries. Plugging in this piecewise form into the plume equation and averaging over the LFT gives

$$A^{pL} = \Delta p_L^{-1} \int_{p_B}^{p_L} A^p dp = w_B A^B + w_L A^L$$

where

$$w_B = \frac{m_1 \Delta p_B}{m_2 \Delta p_L} \ln \frac{m_1 \Delta p_B + m_2 \Delta p_L}{m_1 \Delta p_B}$$

and

$$w_L = 1 - w_B$$

In the case where $m_1 > 0, m_2 = 0$, $w_B = 1$ (no influence from LFT), whereas if $m_1 = 0, m_2 > 0$, $w_B = 0$. The resulting formulation for the conserved quantity of the plume in the LFT A^{pL} in terms of w_B

$$A^{pL} = A^L + w_B(A^B - A^L)$$

The total moisture, q^p_{tot}, is partitioned between condensate and vapor as $q^p_c = q^p_{tot} - q^p_s$, where q_s is the saturation vapor pressure. To find the value of q^p_s, we linearize the Clausius-Clapeyron equation for q_s at the environmental temperature,

$$q^p_s(p_L) = q^L_s + \frac{Lq^L_s}{R_v T^L_0 \kappa \theta^L_{es}}(\theta^L_e - \theta^L_{es} + w_B \left[\theta^B_e - \theta^L_e\right]) \tag{4.4}$$

With

$$\gamma = \frac{Lq^L_s}{R_v T^L_0}$$

Plugging the conserved solutions into (4.3) for the LFT gives:

$$g^{-1}\kappa_0 \theta^L_{es0} B = w_B C_L + (1 - w_B)\, S_L \tag{4.5}$$

C_L and S_L are CAPE-like and subsaturation-like quantities respectively, defined below. We have divided through by $\kappa\theta^L_{es}$ and multiplied by reference values $\kappa_0\theta^L_{es0} = 850\text{K}$ so that C_L and S_L are in K for ease of interpretation

The contribution C_L is undilute buoyancy, corresponding to that of a plume which rises from the boundary layer and undergoes no mixing in the LFT:

$$C_L = \frac{\theta^B_e - \theta^L_{es}}{\kappa\theta^L_{es}} + \alpha_v \left(q^B_s - q^L\right) - \alpha_c \left(q^B - q^B_s\right) \tag{4.6}$$

where q^B_s is the saturation vapor pressure of the boundary layer air (setting $w_B = 1$ in (4.3.1)). The contribution S_L is due to dilution of the plume by incorporation of LFT air:

$$S_L = \frac{\theta^L_e - \theta^L_{es}}{\kappa\theta^L_{es}} + \alpha_v \left(q^*_s - q^L\right) - \alpha_c \left(q^L - q^*_s\right) \tag{4.7}$$

where q^*_s is the saturation vapor pressure of a plume such that $\theta^p_{es} = \theta^L_e$. It is the sole

contribution in the limit where the plume mixes so heavily that it takes on values of the LFT environment ($w_B = 0$ in (4.3.1)).

A key property of (4.5), with (4.6)-(4.7) is that C_L and S_L are independent of entrainment. The effects of entrainment appear entirely as w_B in (4.5). This determines the way that α_v and α_c terms appear in C_L and S_L. It has the very useful property that plots of C_L and S_L do not depend on entrainment, and a line in the C_L- S_L plane corresponds to a particular value of w_B in determining buoyancy. When the coefficients representing the vapor and condensate buoyancy effects α_v and α_c are both zero, buoyancy is a combination of the CAPE and subsaturation measures as used in Ahmed and Neelin (2021a).

4.3.2 Effects of varying w_B on updraft properties

The set of equations above allows us to explore the impact of entrainment on buoyancy and plume components by defining w_B values. For example, Figure 4.1 shows the probability density functions for condensate produced by the environment during raining times for tropical western pacific ARMBE sites at Manus and Nauru. On the upper end where the plume undergoes no dilution, $w_B = 1$, the updraft produces a distribution with a mode greater than 4 $\mathrm{g\,kg^{-1}}$. The fallout parameter, α_c, should produce some fraction of the condensate carried by the updraft in line with observational or modelling condensate loading. We plot the same distributions with a fallout parameter of 0.5 (half the condensate falls out of the updraft; dashed lines) for reference in Figure 4.1. A natural constraint that arises from our formulation is that condensate loading should not overwhelm buoyancy. With our formulation, we can track condensate effects easily, and test the effects of altering α_c in our estimation for the weighting.

The effect of different assumptions on including or omitting the water vapor effect on buoyancy and different values of the condensate fallout ratio α_c on buoyancy contributions C_L and S_L is shown in Fig. 4.2. Recall that C_L and S_L are independent of w_B. In C_L, both effects are substantial, with condensate loading tending to decrease and the water vapor

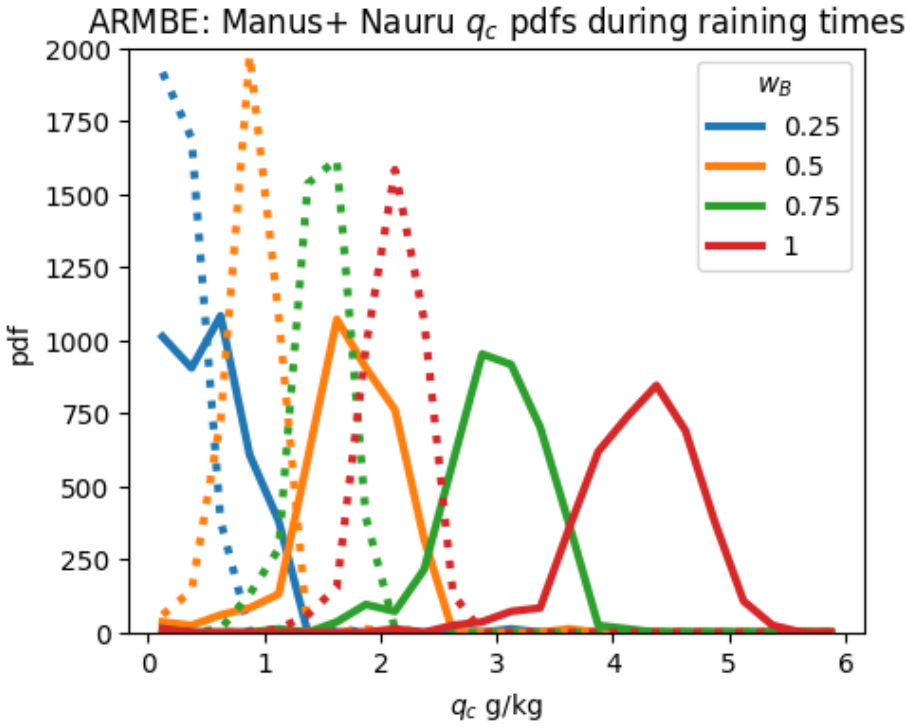

Figure 4.1: Distributions of condensate, q_c, produced with varying w_B rates (solid) during raining times (precipitation $\geq 0.5\text{mm}\,\text{h}^{-1}$) at the ARMBE tropical western Pacific sites, Nauru and Manus. Dashed lines represent the distribution of condensate carried by the plume when the fallout ratio, $\alpha_c = 0.5$.

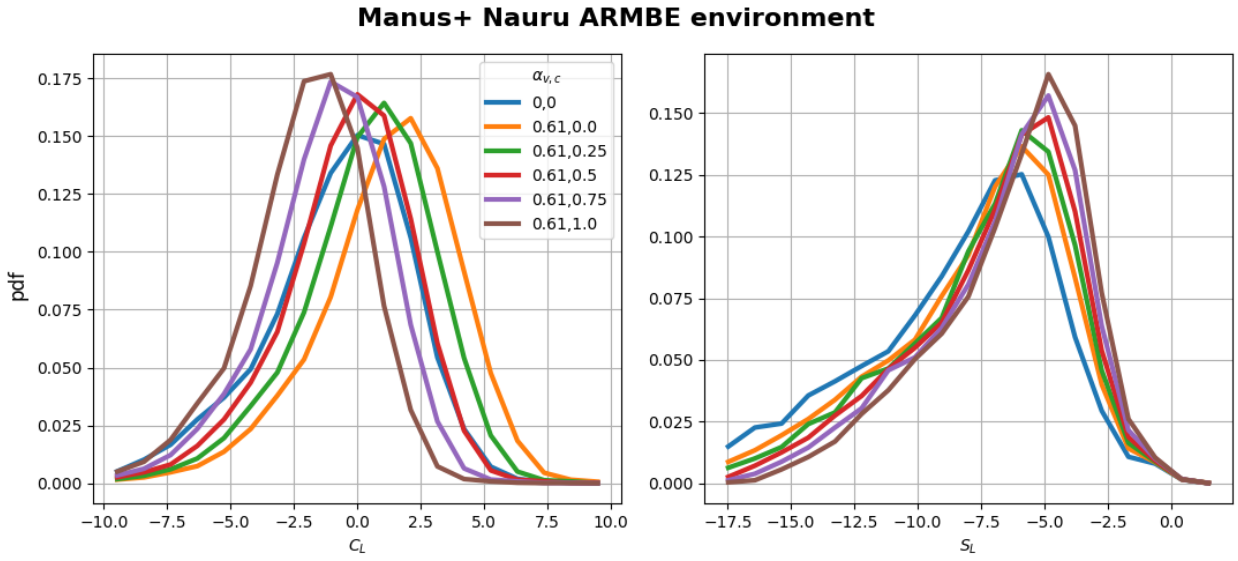

Figure 4.2: Distributions of C_L (left) and S_L (right) with water vapor effect on buoyancy on or off (α_v=0.61 or 0) and varying the microphysical parameter condensate fallout ratio α_c from 0 to 1. Computed over all times for ARMBE data.

buoyancy effect tending to increase the CAPE-like contribution. These effects tend to balance each other for realistic condensate fallout ratio values—for α_c=0.5 (red curve), condensate loading almost perfectly compensates for the water vapor effect, so the PDF looks like the (0,0) case (blue curve) with both effects turned off. In S_L, the overall effect is to move the PDFs modestly toward apparent saturation.

4.3.3 Time evolution of convection and its feedback on the environment

An important consideration for the precipitation onset is the causal relationship of buoyancy to convection. Convection reorganizes the environment, to minimize buoyancy, ultimately altering the C_L and S_L factors of the environment. In theory, during convection the LFT is warmed by the introduction of buoyant air by plumes as the boundary layer is cooled by downdrafts and precipitation. The presence of cloudy air in the LFT leads to moistening, detrainment and evaporation of raindrops that have the potential to further moisten the LFT, while some moisture is lost to precipitation. Increasing buoyancy at the Nauru ARM site is shown to be the result of simultaneous cooling and moistening of the LFT (Emmenegger et al., 2024) attributed to moisture convergence forced by large-scale disturbances (Adames et al., 2021; Hohenegger and Stevens, 2013)

A useful first glance of the evolution of the environment during convection is accomplished by partitioning the life-cycle into three phases of convection: environment at the transition to convection, mature convection, and termination. Distributions for these life-cycles are displayed in Figure 4.3.

A significant feature of Figure 4.3 is the feedback of convection, leaving the environment in a different state than before as determined by the difference between the transition (blue) and termination (red) PDFs. In all cases for C_L, the transition of convection occurs ar higher C_L (blue) before its depleted and returns to a slightly lower value at its termination (red). In every case, S_L increases from the transition to the mature phase, before going back to lower

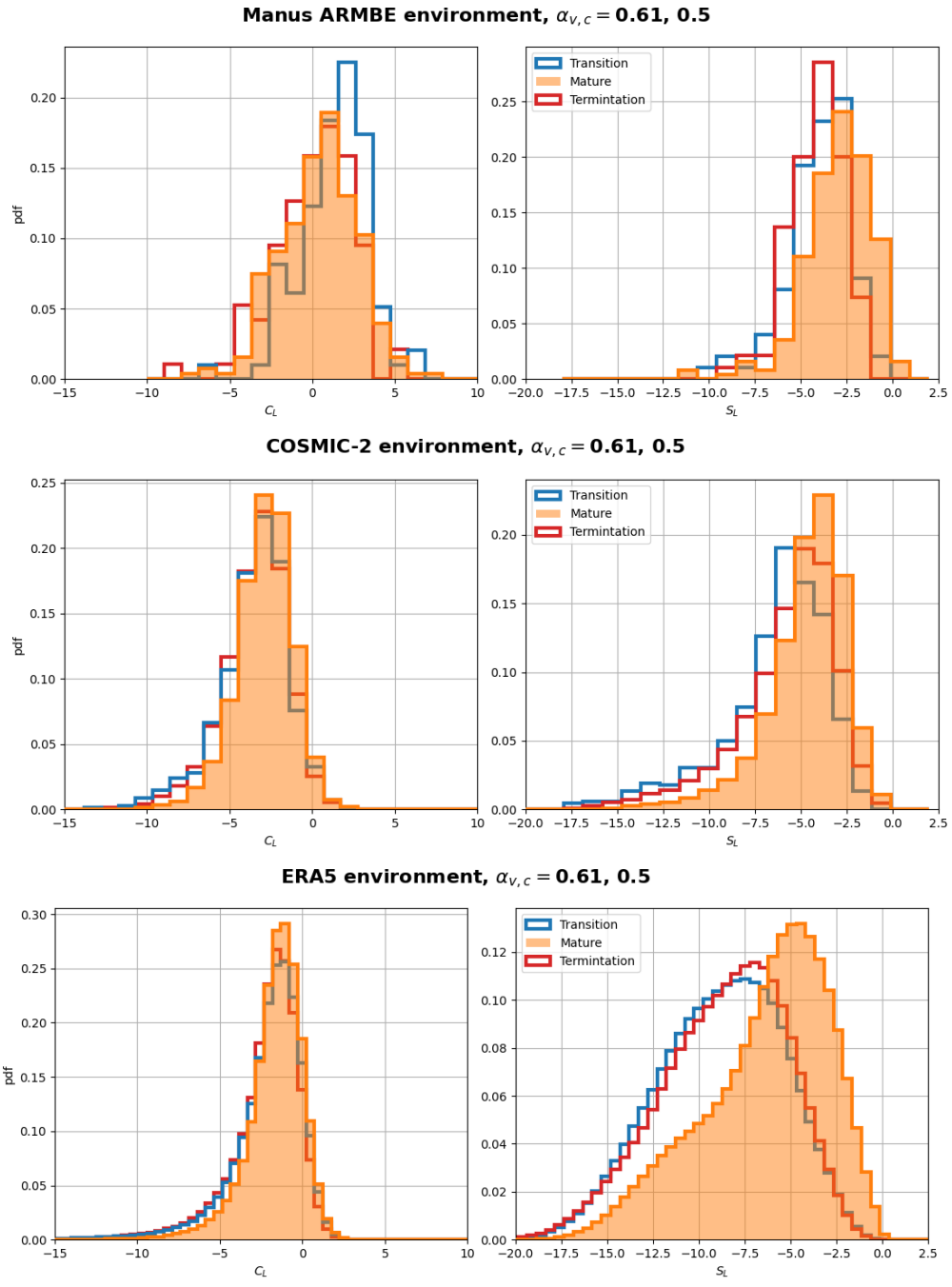

Figure 4.3: Probability distributions for life-cycle partitions for C_L (left) and S_L (right) transition times (blue-filled), mature times (orange-filled) and termination times (red-filled). The binning is different for each dataset, as the sample sizes vary greatly.

values at the terminations. COSMIC-2 and ERA5 increase C_L during convection, before its depleted and ends at a C_L-state lower than the transition. In the ARM data, this is accomplished through cooling and moistening then warming and drying of the LFT, while boundary layer continually cools (supplemental material). This indicates that events survive as long as their LFT undergoes some cooling and moistening. The highlight here is to show the feedback of convection on the environment; in every product, S_L reaches very high values in the precipitating state, a feedback only attainable through convection, not due to the environmental buildup of instability. The difference between the products also needs to be noted. The ARMBE and COSMIC-2 are not spatially averaged as the ERA5, so the boundary layer should take on higher values. This is not seen in COSMIC-2, as there is a dry bias in the boundary layer moisture (discussed in supplemental). The C_L values remain low for both ERA5 and COSMIC-2 compared to ARMBE.

The precipitation onset under all times can be biased by convection, as the rapid onset of precipitation along low-C_L with increasing S_L gives greater weighting to S_L factors. To minimize this bias, we exclude environments affected by convection from our estimation of the precipitation onset. An environment affected by convection is defined as any environmental sample with a precipitation rate over the precipitation threshold (here 0.5 $\mathrm{mm\,h^{-1}}$) within the previous 12 hours. The results of not applying the filter will be detailed in the following section.

Figure 4.4 shows the probability flow of S_L and C_L leading in the 12 hours leading up to convection (left; blue) and during convection (right; red). The flow for discrete bin (S_{Li}, C_{Lj}) is given by

$$F(S_{Li}, C_{Lj}) = \\ \mathrm{Avg}\left[\left(\frac{S_L^{lag} + S_L^{lead}}{2}, \frac{C_L^{lag} + C_L^{lead}}{2}\right) \text{where } (S_L^t, C_L^t) \in (S_{Li}, C_{Lj})\right] \times \mathrm{Prob}_{ij}$$

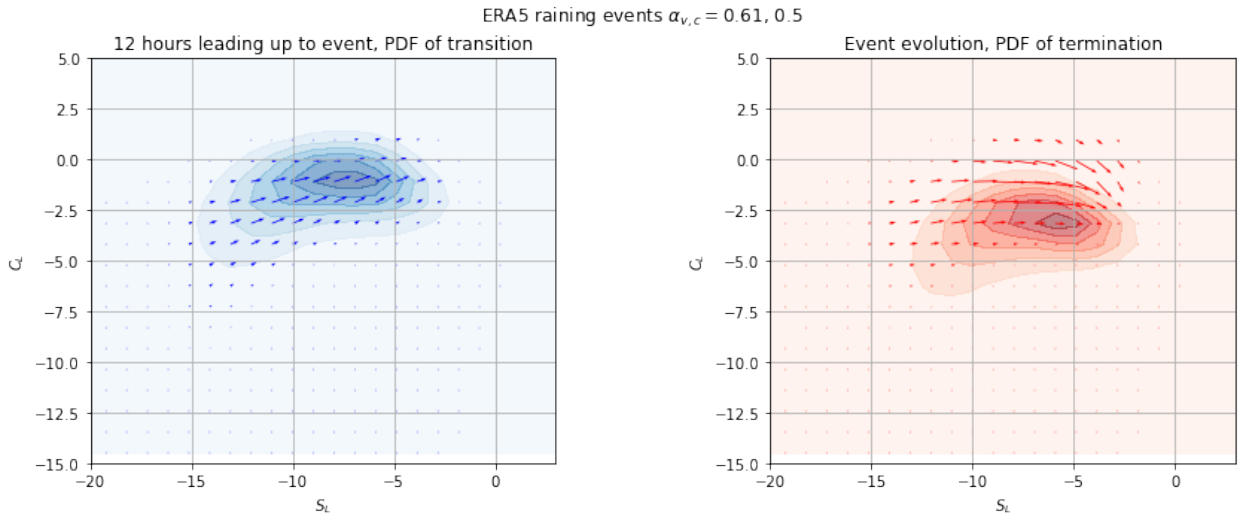

Figure 4.4: (left) The probability flow in the 12 hrs leading up to a convective event represented by vectors and the 2D PDF of the transition points nad (right) probability flow during convection and the 2D PDF of event termination

which is the average of the leading and lagging evolution for each (S_{Li}, C_{Lj}) bin with magnitude weighted by probability, Prob_{ij}, to illustrate the most probable path of the environment towards transition and event termination. Similar evolutions using leading and lagging times across discrete bins are calculated in Wolding et al. (2020).

As shown for ERA5 in figures 4.3 and 4.4, the movement of S_L over before and during a convective event can be due to either moistening or cooling in the LFT. Leading up to an event, the deepening of cumulus congestus in the LFT and its detrainment of moisture preconditions the free troposphere for convection, as entrainment of moister air in a rising plume does not dilute buoyancy as much (Waite and Khouider, 2010). Waite and Khouider (2010) found the moistening of the LFT to be the leading factor to the transition to deep convection, while the cooling of the troposhere and moistening of the boundary layer to be of less importance.Preconditioning by cumulus congestus was found to not be a dominant factor in the transition to deep cumulonimbus in Hohenegger and Stevens (2013). The authors note the slow timescale of moistening by congestus is not consistent with the observed rapid transition to deep convection, which is more consistent rapid cooling and moistening due

to mechanisms such as large-scale disturbances, waves, etc. A similar result was reached in Adames et al. (2021), who found the fast time-scale in which the cooling and moistening of the LFT occurs is consistent with inertio-gravity waves. A marginally subsaturated column within a few Kelvin to zero are convective, as a transient gravity wave can lower the θ_{es} of the environment (Raymond et al., 2003). With this evidence, there is likely a 'subsaturation regime' independent of CAPE-like factors. This regime of convection is apparent in Figure 4.5, where the S_L end of $\langle P \rangle$ dominates and looks independent of C_L.

4.3.4 Estimating the relative weighting of C_L and S_L for onset of convection

We will estimate the weighting of C_L and S_L through empirical methods using ARMBE, COSMIC2 and ERA5 reanalysis products. Similar to physical arguments made in Ahmed and Neelin (2021a), we will use the strength of convection as a proxy for convection via precipitation rate.

Similar to Ahmed and Neelin (2021a), we seek the direction defined by w_B in the $S_L - C_L$ plane that best describes the gradient of the 2D conditional average precipitation increase, or some vector whose direction is correlated most strongly with changes in $\langle P \rangle$. This vector represents the buoyancy axis — its (S_L, C_L) components characterize $(1 - w_B, w_B)$. Orthogonal to this vector lies the contours of buoyancy. To find such a vector, we use a simple approach: rotating a unit vector from $(1 - w_B, w_B) = (0, 1)$ to $(1, 0)$ and finding the angle at which the correlation with precipitation increases is highest.

The unit vector in this range can be described by

$$\vec{u} = \frac{(w_B, 1 - w_B)}{\| (w_B, 1 - w_B) \|}$$

where

$$B = g\kappa_0 \theta^L_{es0} \| (w_B, 1 - w_B) \| \vec{u} \cdot (C_L, S_L)$$

We apply a scalar projection of our unit B vector with the gradient of $\langle P \rangle$, also known as the directional derivative,

$$D_{\vec{u}}\langle P \rangle = \nabla \langle P \rangle \cdot \vec{u}$$

as part of a our optimizing function. Note $D_{\vec{u}}\langle P \rangle$ is maximized when $\vec{u}$ is most highly correlated with the gradient.

We now use an altered correlation scoring function, $S(w_B)$ that is essentially a probability PDF-weighted sum,

$$S(w_B) = \frac{\sum_i \sum_j D_{\vec{u}}\langle P \rangle_{ij} \times \text{Prob(trans)}_{ij}}{\sum_i \sum_j ||\nabla \langle P \rangle_{ij}|| \times \text{Prob(trans)}_{ij}} \tag{4.8}$$

where

$$1 = \sum_i \sum_j \text{Prob}(trans)_{ij}$$

is the PDF of the convective transition points.

The scoring function, $S(w_B) = 1$ if $\nabla \langle P \rangle$ is oriented in the $\vec{u}$ direction. The numerator of $S(w_B)$ weights the buoyancy axis direction according to increases in $S(w_B)$ and probability. Regions in the $C_L - S_L$ plane which do not increase ($\nabla \langle P \rangle \sim 0$) and have a low probability of occurrence (Prob) do not contribute to $S(w_B)$. The advantage of this scoring function is that a critical value which describes the beginning of the ramp of precipitation does not need to be defined, and there is a trade-off between probable increases in precipitation given by the Prob weighting and the magnitude of large increases in precipitation by the most buoyant environments, ensuring that rare but large departures in buoyancy are captured. We use three different $\langle P \rangle$ fields, (1) the first hour of precipitation and (2) average intensity, in which the domain consists only of unaltered environments and transition points, with precipitation matched as the first precipitation measurement in the event, and the average precipitation measurement of the event respectively, (3) and the conditional average precipitation over all times.

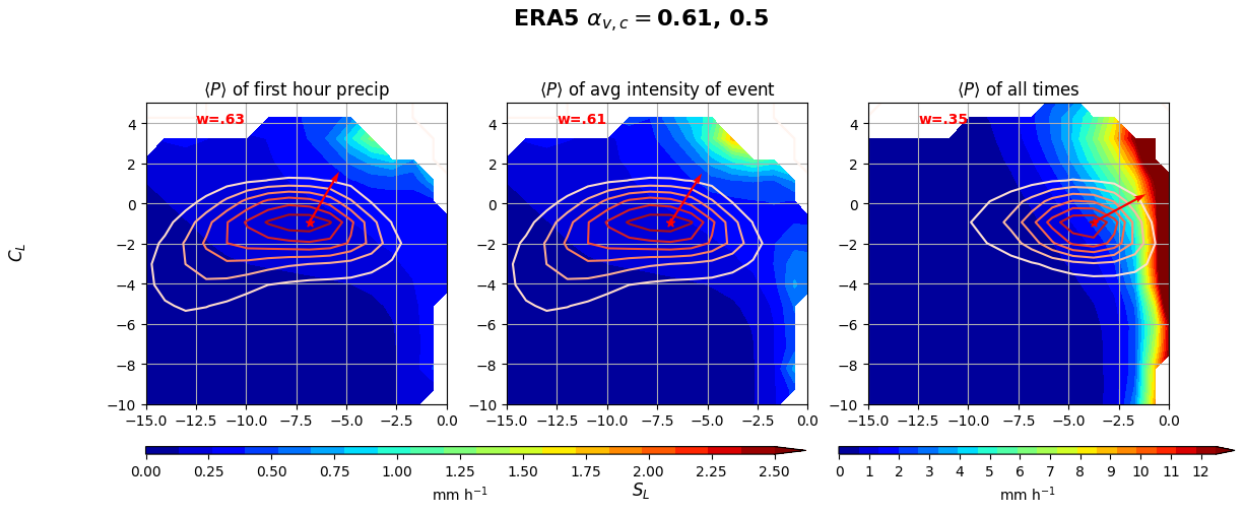

Figure 4.5: 2D conditional-average precipitation (color contours) in the ERA5 dataset for the first hour of precipitation (left), average intensity (middle), and without filtering the environment (right). The PDFs of transition of plotted in the left and middle panels while the right panel has the PDF if all raining times. The w_B value for each expected precipitation field is displayed and visually represented as the vector extending from the mode of the PDF, as estimated using the scoring function, eq. 4.8. Note for the right panel, we use the probability of precipitating PDF, Prob(P) instead of the transition in eq. 4.8

For data in which sampling is limited, we apply a numerical approximation to the gradient, similar to the method used in Ahmed and Neelin (2021a). We provide a brief summary along with our modifications here.

In Ahmed and Neelin (2021a), the authors approximate w_B in the ERA5 reanalysis and a number of models by using an approximation to the gradient of the 2D conditional average precipitation, $\langle P \rangle$ at the mode of the precipitating PDF. We apply slight changes to this methodology. Given the causality of buoyancy to precipitation, we use only nonprecipitating environments as detailed in section 4.3.3, and assign precipitation values to environmental transition points when calculating $\langle P \rangle$. Instead of using the mode of the precipitating PDF, we will use the PDF of the transitioning environment as in Figure 4.5. A numerical approximation to the gradient similar to that used in Ahmed and Neelin (2021a) is then applied using these slight modifications.

The mode of the transitioning PDF as in Figure 4.3 (blue) defines the boundaries of the regions in which the gradient is approximated. The boundaries are defined as so to assess

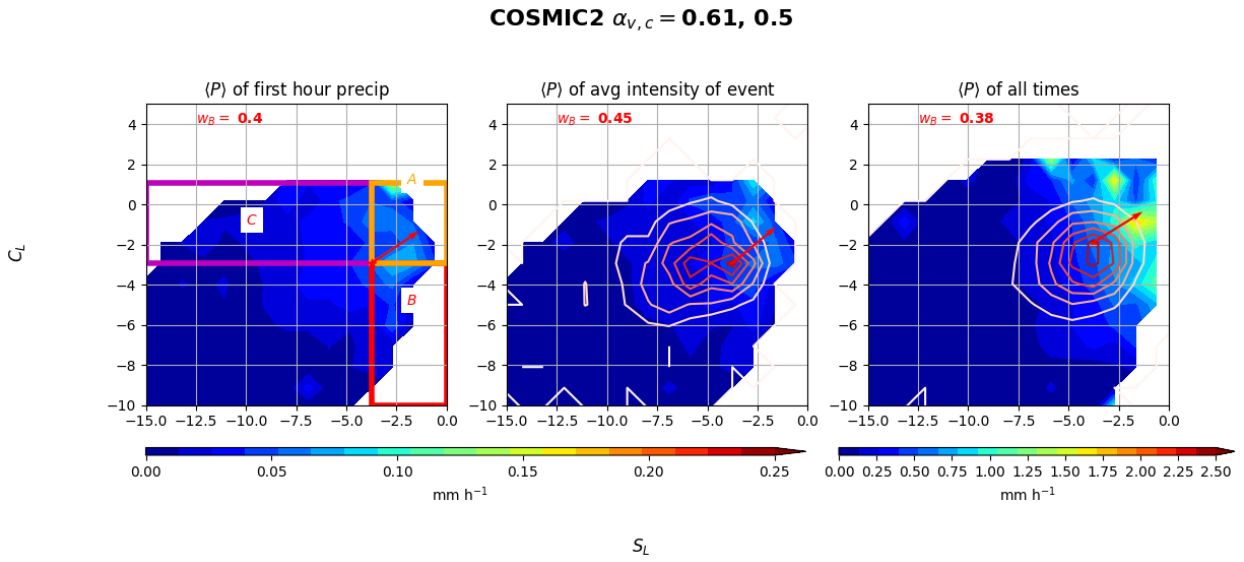

Figure 4.6: Similar to Figure 4.5, but for COSMIC2 data and the w_B value is estimated using estimated using the scoring function (4.10). The regions for the analysis are displayed in the left panel.

how departures from the most probable transition in either direction are reflected in the convective transition. Regions are shown in the left panel of Figure 4.6.

The gradient of $\langle P \rangle$ can be approximated as:

$$\begin{aligned} \nabla\langle P\rangle &= \left(\frac{\partial\langle P\rangle}{\partial S_L}, \frac{\partial\langle P\rangle}{\partial C_L}\right) \\ &\approx \left(\frac{\langle P\rangle_A - \langle P\rangle_C}{S_{LA} - S_{LC}}, \frac{\langle P\rangle_A - \langle P\rangle_B}{C_{LA} - C_{LB}}\right) \end{aligned}$$

where S_{LA} is the average of S_L in the S_A region, etc. Translating the gradient to w_B is,

$$\tan\varphi = \frac{\langle P\rangle_A - \langle P\rangle_C}{S_{LA} - S_{LC}} \times \frac{C_{LA} - C_{LB}}{\langle P\rangle_A - \langle P\rangle_B} \tag{4.9}$$

$$w_B = \frac{\tan\varphi}{1 + \tan\varphi} \tag{4.10}$$

For the ERA5 estimation as in Figure 4.5, the effects of including all times with those altered by convection, considerably affect the estimation of w_B by biasing S_L. The COSMIC-2 estimations as shown in figure 4.6, and show a similar trend in the w_B estimates when all times are included (albeit much smaller than ERA5).

The ERA5 estimates have considerably more weighting towards C_L than S_L than COSMIC-2. We note a dry boundary layer bias in the COSMIC-2 data where the boundary layer moisture is much less on average (shown in supplemental material).

Figure 4.7 shows the convective transition statistics among different w_B values for the ARMBE and COSMIC-2 datasets. At Manus, the numerical approximation yields $w_B = 0.31$, while the COSMIC-2 approximation is slightly larger, $w_B = .40$. A noticeable feature of Fig. 4.7 is how moving from an S_L weighting (blue, $w_B = 0.2$) to a C_L weighting ($w_B = 1.0$ (red)) is reflected in the strength of convection (left) and the probability of transition (middle). After $w_B = 0.5$, the pickup and the transition begin to weaken, emphasizing the importance of mixing and LFT moisture. Strong pickups at lower w_B's possibly stem from a mesoscale convective system or some other large disturbance that can bring a column to saturation.

The ARMBE data is very limited in sampling, yielding only 98 convective events at the Manus site after filtering for environments affected by convection within the prior 12 hours—even without the environmental filter, there amount to only 189 events in the dataset. Additionally, the same methods applied to the Nauru yields an estimation of $w_B = .08$. The climatology of Nauru is important in this regard, it lies on the edge of the of the western pacific warm pool, experiencing both upwelling and downwelling portions of the Walker Circulation (Long and McFarlane, 2012), spending more time at lower C_L. There is a more pronounced subsaturation regime of precipitation at Nauru, likely attributable to more instances of drizzle and a higher probability of precipitating at low C_L.

4.4 Conclusions

Lower free-tropospheric buoyancy can be partitioned into a weighting between undilute (C_L) and dilute (S_L) components, respectively representing (1) buoyancy contributions of a CAPE-like measure of convective instability without dilution by mixing of LFT air and (2) effects due to this mixing associated with LFT subsaturation. This partition is here shown to

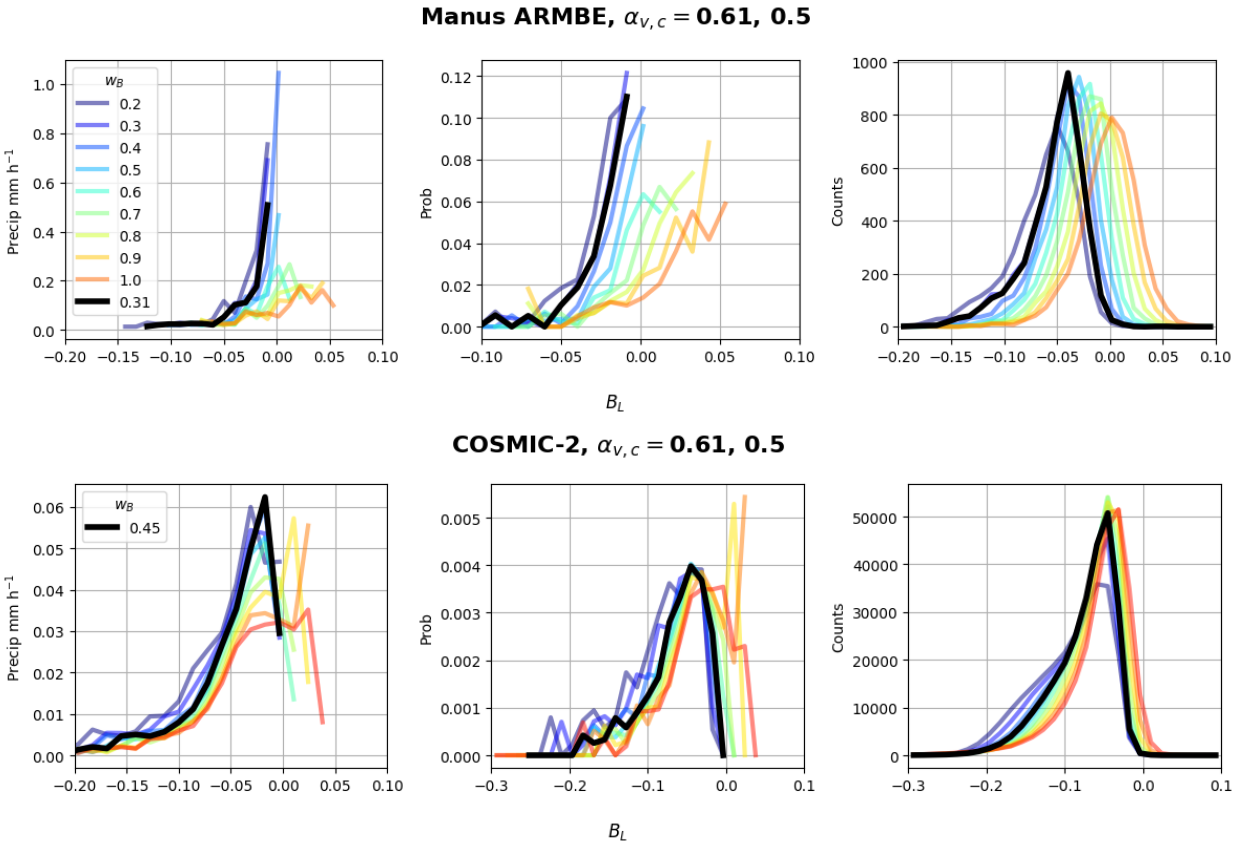

Figure 4.7: First hour precipitation conditionally averaged (left), transition probability (center), PDFs of B_L (right) using various weightings (colors) and the weighting estimated by (4.10)

extend to inclusion of condensate loading and direct water vapor effects on buoyancy, which appear in specific forms in C_L and S_L such that these are independent of mixing. The two effects tend to cancel in C_L, roughly balancing if the fraction of condensate retained in the parcel is in the middle of its possible range.

Using precipitation as a proxy for strength of convection, we show estimates of the weighting between these factors in observations and reanalysis products. This places constraints upon the importance of entrainment of LFT air, with each observational product having complementary strengths. ERA5 reanalysis yields a somewhat larger weighting for C_L, $w_B = 0.63$ in its convective transition compared to both COSMIC-2 and ARMBE data (0.40 and 0.31 respectively). Recalling that the weighting for LFT mixing is (1-w_B), all yield substantial role for LFT entrainment in the convective transition. Overall, the inclusion of condensate loading and direct water vapor effects on buoyancy do not substantially change the entrainment estimate.

These weightings are estimated using the relationship of precipitation at the first hour to the environment in order to minimize biases stemming from convection's feedback on the environment. The first hour precipitation representing convective transition shows a combined dependence on C_L and S_L; the inclusion of environments associated with more mature precipitation skews the relationship to a heavier S_L dependence. This increase in the S_L contribution is consistent with the convective life-cycle—C_L is rapidly depleted while S_L increases as convection matures.

4.5 Supplemental Material

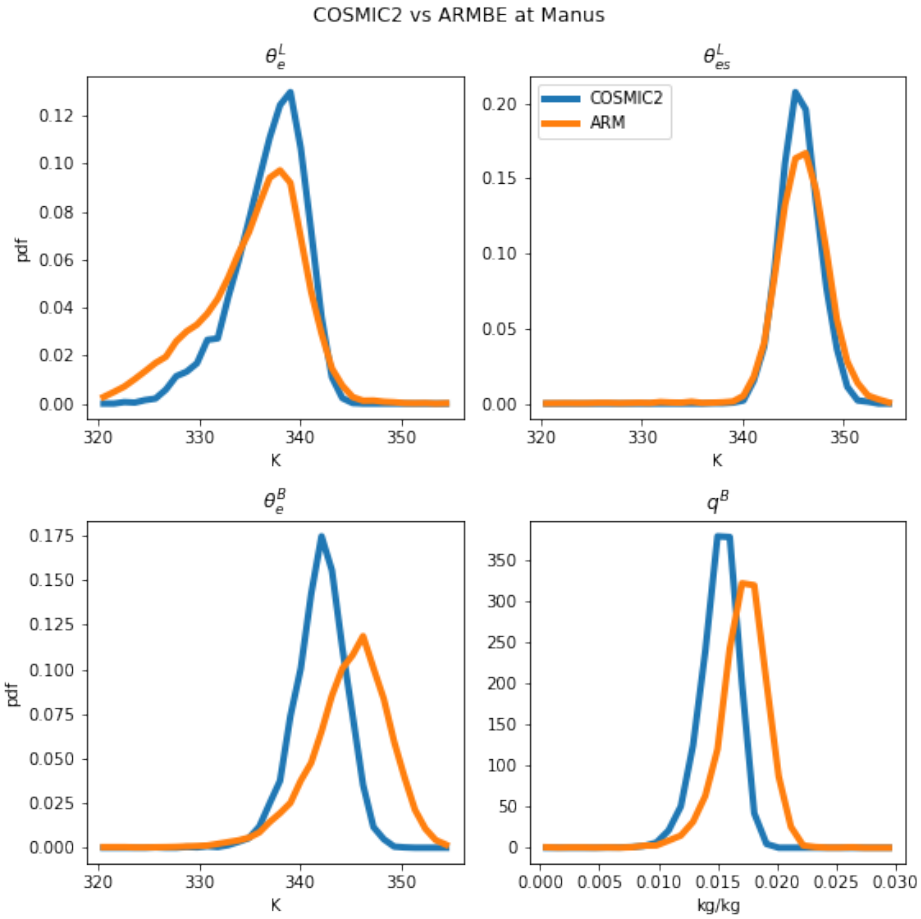

Figure 4.S1: COSMIC-2 vs ARM output at Manus site. While LFT values agree, (top row), boundary layer estimates vary greatly (bottom), due to boundary layer moisture (bottom right).

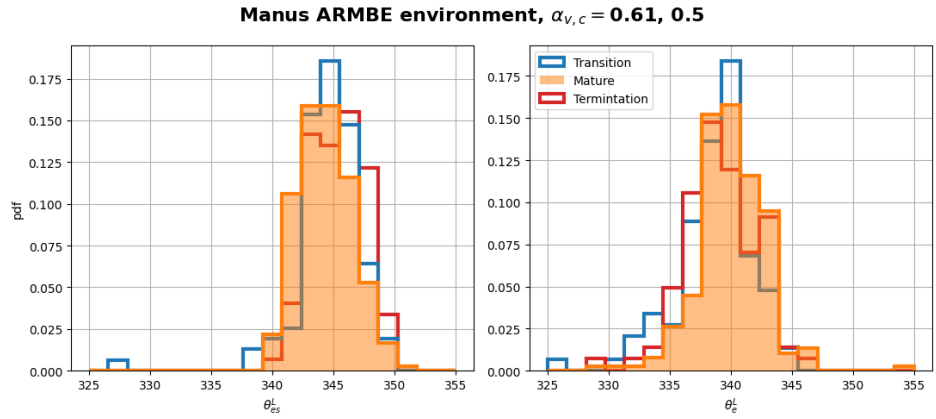

Figure 4.S2: Similar to Fig 4.3, but looking at θ_{es}^L (left) and θ_e^L (right).

Bibliography

Abbott, T. H., Stechmann, S. N., and Neelin, J. D. (2016). Long temporal autocorrelations in tropical precipitation data and spike train prototypes. *Geophys. Res. Lett.*, 43.

Adames, Á. F., Powell, S. W., Ahmed, F., Mayta, V. C., and Neelin, J. D. (2021). Tropical precipitation evolution in a buoyancy-budget framework. *Journal of the Atmospheric Sciences*, 78(2):509–528.

Ahmed, F. and Neelin, J. D. (2018a). Reverse engineering the tropical precipitation–buoyancy relationship. *Journal of the Atmospheric Sciences*, 75(5):1587–1608.

Ahmed, F. and Neelin, J. D. (2018b). Reverse engineering the tropical precipitation-buoyancy relationship. *J. Atmos. Sci.*, 75:1587–1608.

Ahmed, F. and Neelin, J. D. (2021a). A process-oriented diagnostic to assess precipitation-thermodynamic relations and application to cmip6 models. *Geophysical Research Letters*, 48(14):e2021GL094108.

Ahmed, F. and Neelin, J. D. (2021b). Protected convection as a metric of dry air influence on precipitation. *Journal of Climate*, 34(10):3821–3838.

Ahmed, F. and Schumacher, C. (2015). Convective and stratiform components of the precipitation-moisture relationship. *Geophysical Research Letters*, 42(23):10–453.

Ahmed, F. and Schumacher, C. (2017). Geographical differences in the tropical precipitation-

moisture relationship and rain intensity onset. *Geophysical Research Letters*, 44(2):1114–1122.

Allen, M. R. and Ingram, W. J. (2002). Constraints on future changes in climate and the hydrologic cycle. *Nature*, 419:224–232.

Ando, T., Higuchi, T., Hotta, H., Iwakiri, T., Jinno, T., Kino, K., Takano, Y., Toda, M., Yamazaki, K., Suzuki, K. S., et al. (2021). Description of miroc6 agcm.

Arakawa, A. (2004). The cumulus parameterization problem: Past present and future. *J. Climate*, 17:2,493–2,525.

Arakawa, A. and Schubert, W. H. (1974). Interaction of a cumulus cloud ensemble with the large-scale environment Part I. *J. Atmos. Sci.*, 31:674–701.

Bacmeister, J., Lauritzen, P., Dai, A., and Truesdale, J. (2012). Assessing possible dynamical effects of condensate in high resolution climate simulations. *Geophysical Research Letters*, 39(4).

Bao, J. and Stevens, B. (2021). The elements of the thermodynamic structure of the tropical atmosphere. *Journal of the Meteorological Society of Japan. Ser. II*, 99(6):1483–1499.

Bao, J., Stevens, B., Kluft, L., and Jiménez-de-la Cuesta, D. (2021). Changes in the tropical lapse rate due to entrainment and their impact on climate sensitivity. *Geophysical Research Letters*, 48(18):e2021GL094969.

Bechtold, P., Köhler, M., Jung, T., Doblas-Reyes, F., Leutbecher, M., Rodwell, M. J., Vitart, F., and Balsamo, G. (2008a). Advances in simulating atmospheric variability with the ECMWF model: From synoptic to decadal time-scales. *Quart. J. Roy. Meteor. Soc.*, 134:1337–1351.

Bechtold, P., Köhler, M., Jung, T., Doblas-Reyes, F., Leutbecher, M., Rodwell, M. J., Vitart, F., and Balsamo, G. (2008b). Advances in simulating atmospheric variability with the

ecmwf model: From synoptic to decadal time-scales. *Quarterly Journal of the Royal Meteorological Society: A journal of the atmospheric sciences, applied meteorology and physical oceanography*, 134(634):1337–1351.

Bentsen, M., Oliviè, D. J. L., Seland, y., Toniazzo, T., Gjermundsen, A., Graff, L. S., Debernard, J. B., Gupta, A. K., He, Y., Kirkevåg, A., Schwinger, J., Tjiputra, J., Aas, K. S., Bethke, I., Fan, Y., Griesfeller, J., Grini, A., Guo, C., Ilicak, M., Karset, I. H. H., Landgren, O. A., Liakka, J., Moseid, K. O., Nummelin, A., Spensberger, C., Tang, H., Zhang, Z., Heinze, C., Iversen, T., and Schulz, M. (2019). Ncc noresm2-mm model output prepared for cmip6 cmip historical.

Betts, A. K. (1986). A new convective adjustment scheme. Part I: Observational and theoretical basis. *Quart. J. Roy. Meteor. Soc.*, 112:677–691.

Betts, A. K. and Miller, M. J. (1986). A new convective adjustment scheme. Part II: Single column tests using GATE wave, BOMEX, ATEX and arctic air-mass data sets. *Quart. J. Roy. Meteor. Soc.*, 112:693–709.

Biasutti, M. (2013). Forced sahel rainfall trends in the cmip5 archive. *Journal of Geophysical Research: Atmospheres*, 118(4):1613–1623.

Biasutti, M. and Sobel, A. H. (2009). Delayed sahel rainfall and global seasonal cycle in a warmer climate. *Geophysical Research Letters*, 36(23).

Bretherton, C. S., Peters, M. E., and Back, L. (2004). Relationships between water vapor path and precipitation over the tropical oceans. *J. Climate*, 17:1517–1528.

Bretherton, C. S. and Smolarkiewicz, P. K. (1989). Gravity waves compensating subsidence and detrainment around cumulus clouds. *J. Atmos. Sci.*, 46:740–759.

Brown, J. R., Jakob, C., and Haynes, J. M. (2010). An evaluation of rainfall frequency

and intensity over the australian region in a global climate model. *Journal of Climate*, 23(24):6504–6525.

Caldwell, P. M., Mametjanov, A., Tang, Q., Van Roekel, L. P., Golaz, J.-C., Lin, W., Bader, D. C., Keen, N. D., Feng, Y., Jacob, R., et al. (2019). The doe e3sm coupled model version 1: Description and results at high resolution. *Journal of Advances in Modeling Earth Systems*, 11(12):4095–4146.

Cao, J. and Wang, B. (2019). NUIST NESMv3 model output prepared for CMIP6 CMIP historical.

Cao, J., Wang, B., Yang, Y.-M., Ma, L., Li, J., Sun, B., Bao, Y., He, J., Zhou, X., and Wu, L. (2018). The nuist earth system model (nesm) version 3: description and preliminary evaluation. *Geoscientific Model Development*, 11(7):2975–2993.

Chen, D. and Dai, A. (2019). Precipitation characteristics in the community atmosphere model and their dependence on model physics and resolution. *Journal of Advances in Modeling Earth Systems*, 11(7):2352–2374.

Chikira, M. and Sugiyama, M. (2010). A cumulus parameterization with state-dependent entrainment rate. part i: Description and sensitivity to temperature and humidity profiles. *Journal of Atmospheric Sciences*, 67(7):2171–2193.

Covey, C., Gleckler, P. J., Doutriaux, C., Williams, D. N., Dai, A., Fasullo, J., Trenberth, K., and Berg, A. (2016). Metrics for the diurnal cycle of precipitation: Toward routine benchmarks for climate models. *Journal of Climate*, 29(12):4461–4471.

Del Genio, A. D. (2012). Representing the sensitivity of convective cloud systems to tropospheric humidity in general circulation models. *Surv. Geophys.*, 33:637–656.

Del Genio, A. D. and Wu, J. (2010). The Role of Entrainment in the Diurnal Cycle of Continental Convection. *Journal of Climate*, 23(10):2722–2738.

DelGenio, A. D. and Yao, M.-S. (1993). Efficient cumulus parameterization for long-term climate studies: The giss scheme. In *The representation of cumulus convection in numerical models*, pages 181–184. Springer.

Emanuel, K. A. (1994). *Atmospheric Convection*. Oxford University Press, New York.

Emanuel, K. A., Neelin, J. D., and Bretherton, C. S. (1994). On large-scale circulations in convecting atmospheres. *Quart. J. Roy. Meteor. Soc.*, 120:1111–1143.

Emmenegger, T., Ahmed, F., Kuo, Y.-H., Xie, S., Zhang, C., Tao, C., and Neelin, J. D. (2024). The physics behind precipitation onset bias in cmip6 models: the pseudo-entrainment diagnostic and trade-offs between lapse rate and humidity. *Journal of Climate*, 37(6):2013–2033.

Emmenegger, T., Kuo, Y.-H., Xie, S., Zhang, C., Tao, C., and Neelin, J. D. (2022). Evaluating tropical precipitation relations in cmip6 models with arm data. *Journal of Climate*, 35(19):6343–6360.

Fuchs-Stone, Ž., Raymond, D. J., and Sentić, S. (2020). Otrec2019: Convection over the east pacific and southwest caribbean. *Geophysical Research Letters*, 47(11):e2020GL087564.

Gaustad, K. and Riihimaki, L. (1998). Mwr retrievals (mwrret1liljclou).

Giangrande, S. E., Toto, T., Jensen, M. P., Bartholomew, M. J., Feng, Z., Protat, A., Williams, C. R., Schumacher, C., and Machado, L. (2016). Convective cloud vertical velocity and mass-flux characteristics from radar wind profiler observations during goamazon2014/5. *Journal of Geophysical Research: Atmospheres*, 121(21):12–891.

Gjorgjievska, S. and Raymond, D. (2013). Interaction between dynamics and thermodynamics during tropical cyclogenesis. *Atmospheric Chemistry & Physics Discussions*, 13(7).

Hajima, T., Abe, M., Arakawa, O., Suzuki, T., Komuro, Y., Ogura, T., Ogochi, K., Watanabe, M., Yamamoto, A., Tatebe, H., Noguchi, M. A., Ohgaito, R., Ito, A., Yamazaki, D., Ito, A.,

Takata, K., Watanabe, S., Kawamiya, M., and Tachiiri, K. (2019). MIROC MIROC-ES2L model output prepared for CMIP6 CMIP historical.

Hersbach, H., Bell, B., Berrisford, P., Hirahara, S., Horányi, A., Muñoz-Sabater, J., Nicolas, J., Peubey, C., Radu, R., Schepers, D., et al. (2020). The ERA5 global reanalysis. *Quarterly Journal of the Royal Meteorological Society*.

Hirota, N., Takayabu, Y. N., Watanabe, M., Kimoto, M., and Chikira, M. (2014). Role of convective entrainment in spatial distributions of and temporal variations in precipitation over tropical oceans. *Journal of Climate*, 27(23):8707–8723.

Hohenegger, C. and Stevens, B. (2013). Preconditioning deep convection with cumulus congestus. *Journal of the Atmospheric Sciences*, 70(2):448–464.

Holdridge, D. and Kyrouac, J. (1998). Surface meteorological instrumentation (met).

Holloway, C. E. and Neelin, J. D. (2009a). Moisture vertical structure, column water vapor, and tropical deep convection. *J. Atmos. Sci.*, 66:1665–1683.

Holloway, C. E. and Neelin, J. D. (2009b). Moisture vertical structure, column water vapor, and tropical deep convection. *Journal of Atmospheric Sciences*, 66(6):1665–1683.

Holloway, C. E. and Neelin, J. D. (2010). Temporal relations of column water vapor and tropical precipitation. *J. Atmos. Sci.*, 67:1091–1105.

Hourdin, F., Grandpeix, J.-Y., Rio, C., Bony, S., Jam, A., Cheruy, F., Rochetin, N., Fairhead, L., Idelkadi, A., Musat, I., Dufresne, J.-L., Lahellec, A., Lefebvre, M.-P., and Roehrig, R. (2013). Lmdz5b: the atmospheric component of the ipsl climate model with revisited parameterizations for clouds and convection. *Climate Dynamics*, 40(9-10):2193–2222.

Hwang, Y.-T. and Frierson, D. M. W. (2013). Link between the double-intertropical convergence zone problem and cloud biases over the Southern Ocean. *Proceedings of the National Academy of Sciences*, 110:4935–4940.

Igel, M. R. and Biello, J. A. (2019). A reconstructed total precipitation framework. *npj Climate and Atmospheric Science*, 2(1):1–7.

Jensen, M. P. and Del Genio, A. D. (2006). Factors limiting convective cloud-top height at the ARM nauru island climate research facility. *J. Climate*, 19:2105–2117.

Jiang, X., Kim, D., and Maloney, E. D. (2017). Progress and status of mjo simulation in climate models and process-oriented diagnostics. In *Sixth Int. Workshop on Monsoons*, pages 119–124.

Jing, X., Suzuki, K., Guo, H., Goto, D., Ogura, T., Koshiro, T., and Mülmenstädt, J. (2017). A multimodel study on warm precipitation biases in global models compared to satellite observations. *Journal of Geophysical Research: Atmospheres*, 122(21):11–806.

Kain, J. S. and Fritsch, J. M. (1990). A one-dimensional entraining/detraining plume model and its application in convective parameterization. *J. Atmos. Sci.*, 47:2784–2802.

Keil, C., Heinlein, F., and Craig, G. C. (2014). The convective adjustment time-scale as indicator of predictability of convective precipitation. *Quarterly Journal of the Royal Meteorological Society*, 140(679):480–490.

Kim, D., Del Genio, A. D., and Yao, M.-S. (2013). Moist convection scheme in model e2. *arXiv preprint arXiv:1312.7496*.

Kim, D., Sobel, A. H., Del Genio, A. D., Chen, Y., Camargo, S. J., Yao, M.-S., Kelley, M., and Nazarenko, L. (2012). The tropical subseasonal variability simulated in the nasa giss general circulation model. *Journal of Climate*, 25(13):4641–4659.

Kumar, V. V., Jakob, C., Protat, A., Williams, C. R., and May, P. T. (2015). Mass-flux characteristics of tropical cumulus clouds from wind profiler observations at darwin, australia. *Journal of the Atmospheric Sciences*, 72(5):1837–1855.

Kuo, Y.-H., Mechoso, C. R., and Neelin, J. D. (2017). Tropical convective onset statistics and causality in the water vapor-precipitation relation. *J. Atmos. Sci.*, 74:915–930.

Kuo, Y.-H., Neelin, J. D., Booth, J. F., Chen, C.-C., Chen, W.-T., Gettelman, A., Jiang, X., Maloney, E., Mechoso, C. R., Ming, Y., Schiro, K. A., Seman, C. J., Wu, C.-M., and Zhao, M. (2020). Convective transition statistics over tropical oceans for climate model diagnostics: GCM evaluation. *J. Atmos. Sci.*, 77:379–403.

Kuo, Y.-H., Neelin, J. D., and Schiro, K. A. (2018). Convective transition statistics over tropical oceans for climate model diagnostics: Observational baseline. *J. Atmos. Sci.*, 75:1553–1570.

Long, C. N. and McFarlane, S. A. (2012). Quantification of the impact of nauru island on arm measurements. *Journal of applied meteorology and climatology*, 51(3):628–636.

Luo, Z. J., Liu, G. Y., and Stephens, G. L. (2010). Use of A-Train data to estimate convective buoyancy and entrainment rate. *Geophys. Res. Lett.*, 37.

Maloney, E. D., Adames, Á. F., and Bui, H. X. (2019). Madden–julian oscillation changes under anthropogenic warming. *Nature Climate Change*, 9(1):26–33.

Manabe, S., Smagorinsky, J., and Strickler, R. F. (1965). Simulated climatology of a general circulation model with a hydrologic cycle. *Monthly Weather Review*, 93(12):769–798.

Manabe, S. and Strickler, R. F. (1964). Thermal equilibrium of the atmosphere with a convective adjustment. *J. Atmos. Sci.*, 21:361–385.

Mapes, B. and Neale, R. (2011). Parameterizing convective organization to escape the entrainment dilemma. *Journal of Advances in Modeling Earth Systems*, 3(2).

Mather, J. H. and Voyles, J. W. (2013). The arm climate research facility: A review of structure and capabilities. *Bulletin of the American Meteorological Society*, 94(3):377–392.

Matthews, S., Hacker, J. M., Cole, J., Hare, J., Long, C. N., and Reynolds, R. M. (2007). Modification of the atmospheric boundary layer by a small island: Observations from nauru. *Monthly weather review*, 135(3):891–905.

McGee, C. J. and van den Heever, S. C. (2014). Latent heating and mixing due to entrainment in tropical deep convection. *Journal of the Atmospheric Sciences*, 71(2):816–832.

Meehl, G. A., Collins, W. D., Boville, B. A., Kiehl, J. T., Wigley, T. M. L., and Arblaster, J. M. (2000). Response of the NCAR climate system model to increased CO_2 and the role of physical processes. *J. Climate*, 13:1879–1898.

Mission, T. R. M. (2011). Trmm (tmpa) rainfall estimate l3 3 hour 0.25 degree x 0.25 degree v7, greenbelt, md, goddard earth sciences data and information services center (ges disc). *TRMM_3B42_7. html*.

Möbis, B. and Stevens, B. (2012). Factors controlling the position of the intertropical convergence zone on an aquaplanet. *Journal of Advances in Modeling Earth Systems*, 4(4).

Moorthi, S. and Suarez, M. J. (1992). Relaxed Arakawa-Schubert: A parameterization of moist convection for general circulation models. *Mon. Wea. Rev.*, 120:978–1002.

NASA Goddard Institute for Space Studies (NASA/GISS) (2018). NASA-GISS GISS-E2.1G model output prepared for CMIP6 CMIP historical.

Neale, R. B. et al. (2010). Description of the ncar community atmosphere model (cam 5.0).

Neale, R. B., Richter, J. H., and Jochum, M. (2008). The impact of convection on ENSO: From a delayed oscillator to a series of events. *J. Climate*, 21:5904–5924.

Neelin, J. D., Lintner, B. R., Tian, B., Li, Q., Zhang, L., Patra, P. K., Chahine, M. T., and Stechmann, S. N. (2010). Long tails in deep columns of natural and anthropogenic tropospheric tracers. *Geophys. Res. Lett.*, 37:L05804.

Neelin, J. D., Peters, O., and Hales, K. (2009). The transition to strong convection. *J. Atmos. Sci.*, 66:2367–2384.

Neelin, J. D., Peters, O., Lin, J. W.-B., Hales, K., and Holloway, C. E. (2008a). Rethinking convective quasi-equilibrium: Observational constraints for stochastic convective schemes in climate models. *Philosophical Transactions of the Royal Society A: Mathematical, Physical and Engineering Sciences*, 366(1875):2579–2602.

Neelin, J. D., Peters, O., Lin, J. W.-B., Hales, K., and Holloway, C. E. (2008b). Rethinking convective quasi-equilibrium: observational constraints for stochastic convective schemes in climate models. *Phil. Trans. Royal Soc. A*, 366:2581–2604.

Neelin, J. D. and Yu, J.-Y. (1994). Modes of tropical variability under convective adjustment and the Madden-Julian oscillation. Part I: Analytical results. *J. Atmos. Sci.*, 51:1876–1894.

Neelin, J. D. and Zeng, N. (2000). A quasi-equilibrium tropical circulation model—formulation. *J. Atmos. Sci.*, 57:1741–1766.

Nordeng, T. E. (1994). Extended versions of the convective parametrization scheme at ecmwf and their impact on the mean and transient activity of the model in the tropics. *Research Department Technical Memorandum*, 206:1–41.

Oueslati, B. and Bellon, G. (2013). Convective entrainment and large-scale organization of tropical precipitation: Sensitivity of the cnrm-cm5 hierarchy of models. *Journal of Climate*, 26(9):2931–2946.

Pall, P., Allen, M. R., and Stone, D. A. (2007). Testing the Clausius-Clapeyron constraint on changes in extreme precipitation under CO_2 warming. *Climate Dynamics*, 28:351–363.

Pathak, R., Sahany, S., Mishra, S. K., and Dash, S. (2019). Precipitation biases in cmip5 models over the south asian region. *Scientific reports*, 9(1):1–13.

Peters, O. and Neelin, J. D. (2006). Critical phenomena in atmospheric precipitation. *Nature Physics*, 2:393–396.

Powell, S. W. (2022). Criticality in the shallow-to-deep transition of simulated tropical marine convection. *Journal of the Atmospheric Sciences*.

Rasch, P., Xie, S., Ma, P.-L., Lin, W., Wang, H., Tang, Q., Burrows, S., Caldwell, P., Zhang, K., Easter, R., et al. (2019). An overview of the atmospheric component of the energy exascale earth system model. *Journal of Advances in Modeling Earth Systems*, 11(8):2377–2411.

Raymond, D., Sessions, S., and López Carrillo, C. (2011). Thermodynamics of tropical cyclogenesis in the northwest pacific. *Journal of Geophysical Research: Atmospheres*, 116(D18).

Raymond, D. J. (1994). Cumulus convection and the madden-julian oscillation of the tropical troposphere. *Physica D: Nonlinear Phenomena*, 77(1-3):1–22.

Raymond, D. J. (1995). Regulation of moist convection over the west pacific warm pool. *Journal of Atmospheric Sciences*, 52(22):3945–3959.

Raymond, D. J. (2017). Convection in the east pacific intertropical convergence zone. *Geophysical Research Letters*, 44(1):562–568.

Raymond, D. J., Raga, G., Bretherton, C. S., Molinari, J., López-Carrillo, C., and Fuchs, Ž. (2003). Convective forcing in the intertropical convergence zone of the eastern pacific. *Journal of the atmospheric sciences*, 60(17):2064–2082.

Rio, C., Hourdin, F., Grandpeix, J.-Y., and Lafore, J.-P. (2009). Shifting the diurnal cycle of parameterized deep convection over land. *Geophysical Research Letters*, 36(7).

Rushley, S., Kim, D., Bretherton, C., and Ahn, M.-S. (2018). Reexamining the nonlinear

moisture-precipitation relationship over the tropical oceans. *Geophysical research letters*, 45(2):1133–1140.

Sahany, S., Neelin, J. D., Hales, K., and Neale, R. B. (2012). Temperature-moisture dependence of the deep convective transition as a constraint on entrainment in climate models. *J. Atmos. Sci.*, 69:1340–1358.

Sarachik, E. S. (1985). A simple theory for the vertical structure of the tropical atmosphere. *Pure Appl. Geophys.*, 123:261–271.

Schiro, K., Neelin, J. D., Adams, D. K., and Lintner, B. R. (2016a). Deep convection and column water vapor over tropical land vs. tropical ocean: A comparison between the Amazon and the Tropical Western Pacific. *J. Atmos. Sci.*, 73:4043–4063.

Schiro, K. A. (2017). *Thermodynamic Controls on Deep Convection in the Tropics: Observations and Applications to Modeling*. PhD thesis, University of California, Los Angeles. 132 pp.

Schiro, K. A., Ahmed, F., Giangrande, S. E., and Neelin, J. D. (2018a). GoAmazon2014/5 campaign points to deep-inflow approach to deep convection across scales. *Proceedings of the National Academy of Sciences*, 115:201719842.

Schiro, K. A., Ahmed, F., Giangrande, S. E., and Neelin, J. D. (2018b). Goamazon2014/5 campaign points to deep-inflow approach to deep convection across scales. *Proceedings of the National Academy of Sciences*, 115(18):4577–4582.

Schiro, K. A. and Neelin, J. D. (2019). Deep convective organization, moisture vertical structure, and convective transition using deep-inflow mixing. *J. Atmos. Sci.*, 76(4):965–987.

Schiro, K. A., Neelin, J. D., Adams, D. K., and Lintner, B. R. (2016b). Deep convection and column water vapor over tropical land versus tropical ocean: A comparison between the

amazon and the tropical western pacific. *Journal of the Atmospheric Sciences*, 73(10):4043–4063.

Schmidt, G. A., Kelley, M., Nazarenko, L., Ruedy, R., Russell, G. L., Aleinov, I., Bauer, M., Bauer, S. E., Bhat, M. K., Bleck, R., et al. (2014). Configuration and assessment of the giss modele2 contributions to the cmip5 archive. *Journal of Advances in Modeling Earth Systems*, 6(1):141–184.

Schneider, T., O'Gorman, P. A., and Levine, X. J. (2010). Water Vapor and the Dynamics of Climate Changes. *Reviews of Geophysics*, 48(3):RG3001.

Seland, Ø., Bentsen, M., Olivié, D., Toniazzo, T., Gjermundsen, A., Graff, L. S., Debernard, J. B., Gupta, A. K., He, Y.-C., Kirkevåg, A., et al. (2020). Overview of the norwegian earth system model (noresm2) and key climate response of cmip6 deck, historical, and scenario simulations. *Geoscientific Model Development*, 13(12):6165–6200.

Seland, y., Bentsen, M., Oliviè, D. J. L., Toniazzo, T., Gjermundsen, A., Graff, L. S., Debernard, J. B., Gupta, A. K., He, Y., Kirkevåg, A., Schwinger, J., Tjiputra, J., Aas, K. S., Bethke, I., Fan, Y., Griesfeller, J., Grini, A., Guo, C., Ilicak, M., Karset, I. H. H., Landgren, O. A., Liakka, J., Moseid, K. O., Nummelin, A., Spensberger, C., Tang, H., Zhang, Z., Heinze, C., Iversen, T., and Schulz, M. (2019). NCC NorESM2-LM model output prepared for CMIP6 CMIP historical.

Singh, M. S. and Neogi, S. (2022). On the interaction between moist convection and large-scale ascent in the tropics. *Journal of Climate*, pages 1–47.

Singh, M. S. and O'Gorman, P. A. (2013). Influence of entrainment on the thermal stratification in simulations of radiative-convective equilibrium. *Geophysical Research Letters*, 40(16):4398–4403.

Singh, M. S., Warren, R. A., and Jakob, C. (2019). A steady-state model for the relationship

between humidity, instability, and precipitation in the tropics. *Journal of Advances in Modeling Earth Systems*, 11(12):3973–3994.

Sobel, A. H. and Bretherton, C. S. (2000). Modeling tropical precipitation in a single column. *J. Climate*, 13:4378–4392.

Stephens, G. L., L'Ecuyer, T., Forbes, R., Gettelmen, A., Golaz, J.-C., Bodas-Salcedo, A., Suzuki, K., Gabriel, P., and Haynes, J. (2010). Dreary state of precipitation in global models. *Journal of Geophysical Research: Atmospheres*, 115(D24).

Stevens, B., Brogniez, H., Kiemle, C., Lacour, J.-L., Crevoisier, C., and Kiliani, J. (2017). Structure and dynamical influence of water vapor in the lower tropical troposphere. In *Shallow clouds, water vapor, circulation, and climate sensitivity*, pages 199–225. Springer.

Stevens, B. and Siebesma, A. P. (2020). Clouds as fluids. *Clouds and Climate, A. Siebesma, S. Bony, C. Jakob, and B. Stevens, Eds., Climate Science's Greatest Challenge, Cambridge Univ. Press., UK*, pages 35–73.

Stokes, G. M. and Schwartz, S. E. (1994). The Atmospheric Radiation Measurement (ARM) Program: Programmatic background and design of the cloud and radiation testbed. *Bull. Amer. Meteor. Soc.*, 75:1201–1221.

Su, H., Jiang, J. H., Neelin, J. D., Shen, T. J., Zhai, C., Yue, Q., Wang, Z., Huang, L., Choi, Y.-S., Stephens, G. L., and Yung, Y. L. (2017). Tightening of tropical ascent and high clouds key to precipitation change in a warmer climate. *Nature Comm.*, 8:15771.

Suhas, E. and Zhang, G. J. (2014). Evaluation of trigger functions for convective parameterization schemes using observations. *J. Climate*, 27:7647–7666.

Tan, J., Petersen, W. A., Kirstetter, P.-E., and Tian, Y. (2017). Performance of imerg as a function of spatiotemporal scale. *Journal of Hydrometeorology*, 18(2):307–319.

Tang, S., Gleckler, P., Xie, S., Lee, J., Ahn, M.-S., Covey, C., and Zhang, C. (2021). Evaluating the diurnal and semidiurnal cycle of precipitation in cmip6 models using satellite-and ground-based observations. *Journal of Climate*, 34(8):3189–3210.

Tang, S., Xie, S., Guo, Z., Hong, S.-Y., Khouider, B., Klocke, D., Köhler, M., Koo, M.-S., Krishna, P. M., Larson, V. E., et al. (2022). Long-term single-column model intercomparison of diurnal cycle of precipitation over midlatitude and tropical land. *Quarterly Journal of the Royal Meteorological Society*, 148(743):641–669.

Tatebe, H. and Watanabe, M. (2018). MIROC MIROC6 model output prepared for CMIP6 CMIP historical.

Tian, B. and Dong, X. (2020). The double-itcz bias in cmip3, cmip5, and cmip6 models based on annual mean precipitation. *Geophysical Research Letters*, 47(8):e2020GL087232.

Tiedtke, M. (1989). A comprehensive mass flux scheme for cumulus parameterization in large-scale models. *Mon. Wea. Rev.*, 117:1779–1800.

Tokioka, T., Yamazaki, K., Kitoh, A., and Ose, T. (1988). The equatorial 30-60 day oscillation and the Arakawa-Schubert penetrative cumulus parameterization. *J. Meteor. Soc. Japan*, 66:883–901.

Trenberth, K. E., Dai, A., Rasmussen, R. M., and Parsons, D. B. (2003). The Changing Character of Precipitation. *Bulletin of the American Meteorological Society*, 84(9):1205–1218.

Turk, F. J., Padullés, R., Morabito, D. D., Emmenegger, T., and Neelin, J. D. (2022). Distinguishing convective-transition moisture-temperature relationships with a constellation of polarimetric radio occultation observations in and near convection. *Atmosphere*, 13(2):259.

Turner, D. D., Clough, S. A., Liljegren, J. C., Clothiaux, E. E., Cady-Pereira, K. E., and Gaustad, K. L. (2007). Retrieving liquid wat0er path and precipitable water vapor from

the atmospheric radiation measurement (arm) microwave radiometers. *IEEE Transactions on Geoscience and Remote Sensing*, 45(11):3680–3690.

Voigt, A., Biasutti, M., Scheff, J., Bader, J., Bordoni, S., Codron, F., Dixon, R. D., Jonas, J., Kang, S. M., Klingaman, N. P., et al. (2016). The tropical rain belts with an annual cycle and a continent model intercomparison project: Tracmip. *Journal of Advances in Modeling Earth Systems*, 8(4):1868–1891.

Waite, M. L. and Khouider, B. (2010). The deepening of tropical convection by congestus preconditioning. *Journal of the Atmospheric Sciences*, 67(8):2601–2615.

Wentz, F., Gentemann, C., and Hilburn, K. (2015). Remote sensing systems trmm tmi daily environmental suite on 0.25 deg grid, version 7.1. *Remote Sensing Systems, Santa Rosa, CA, http://www. remss. com/missions/tmi*.

Wieners, K.-H., Giorgetta, M., Jungclaus, J., Reick, C., Esch, M., Bittner, M., Legutke, S., Schupfner, M., Wachsmann, F., Gayler, V., Haak, H., de Vrese, P., Raddatz, T., Mauritsen, T., von Storch, J.-S., Behrens, J., Brovkin, V., Claussen, M., Crueger, T., Fast, I., Fiedler, S., Hagemann, S., Hohenegger, C., Jahns, T., Kloster, S., Kinne, S., Lasslop, G., Kornblueh, L., Marotzke, J., Matei, D., Meraner, K., Mikolajewicz, U., Modali, K., Müller, W., Nabel, J., Notz, D., Peters, K., Pincus, R., Pohlmann, H., Pongratz, J., Rast, S., Schmidt, H., Schnur, R., Schulzweida, U., Six, K., Stevens, B., Voigt, A., and Roeckner, E. (2019a). MPI-M MPI-ESM1.2-LR model output prepared for CMIP6 CMIP historical.

Wieners, K.-H., Giorgetta, M., Jungclaus, J., Reick, C., Esch, M., Bittner, M., Legutke, S., Schupfner, M., Wachsmann, F., Gayler, V., Haak, H., de Vrese, P., Raddatz, T., Mauritsen, T., von Storch, J.-S., Behrens, J., Brovkin, V., Claussen, M., Crueger, T., Fast, I., Fiedler, S., Hagemann, S., Hohenegger, C., Jahns, T., Kloster, S., Kinne, S., Lasslop, G., Kornblueh, L., Marotzke, J., Matei, D., Meraner, K., Mikolajewicz, U., Modali, K., Müller, W., Nabel, J., Notz, D., Peters, K., Pincus, R., Pohlmann, H., Pongratz, J., Rast, S., Schmidt, H.,

Schnur, R., Schulzweida, U., Six, K., Stevens, B., Voigt, A., and Roeckner, E. (2019b). MPI-M MPI-ESM1.2-LR model output prepared for CMIP6 CMIP historical.

Wolding, B., Dias, J., Kiladis, G., Ahmed, F., Powell, S. W., Maloney, E., and Branson, M. (2020). Interactions between Moisture and Tropical Convection. Part I: The Coevolution of Moisture and Convection. *Journal of the Atmospheric Sciences*, 77(5):1783–1799.

Wolding, B., Powell, S. W., Ahmed, F., Dias, J., Gehne, M., Kiladis, G., and Neelin, J. D. (2022). Tropical thermodynamic–convection coupling in observations and reanalyses. *Journal of the Atmospheric Sciences*, 79(7):1781–1803.

Wolding, B. O. and Maloney, E. D. (2015). Objective diagnostics and the madden–julian oscillation. part ii: Application to moist static energy and moisture budgets. *Journal of Climate*, 28(19):7786–7808.

Xie, S., Lin, W., Rasch, P. J., Ma, P.-L., Neale, R., Larson, V. E., Qian, Y., Bogenschutz, P. A., Caldwell, P., Cameron-Smith, P., et al. (2018). Understanding cloud and convective characteristics in version 1 of the e3sm atmosphere model. *Journal of Advances in Modeling Earth Systems*, 10(10):2618–2644.

Xie, S., McCoy, R. B., Klein, S. A., Cederwall, R. T., Wiscombe, W. J., and coauthors (2010). Clouds and more: ARM climate modeling best estimate data. *Bull. Amer. Meteorol. Soc.*, 91(1):13–20.

Xie, S., Wang, Y.-C., Lin, W., Ma, H.-Y., Tang, Q., Tang, S., Zheng, X., Golaz, J.-C., Zhang, G. J., and Zhang, M. (2019). Improved diurnal cycle of precipitation in e3sm with a revised convective triggering function. *Journal of Advances in Modeling Earth Systems*, 11(7):2290–2310.

Xie, S., Xu, K.-M., Cederwall, R. T., Bechtold, P., Genio, A. D. D., Klein, S. A., Cripe, D. G., Ghan, S. J., Gregory, D., Iacobellis, S. F., et al. (2002). Intercomparison and evaluation of

cumulus parametrizations under summertime midlatitude continental conditions. *Quarterly Journal of the Royal Meteorological Society: A journal of the atmospheric sciences, applied meteorology and physical oceanography*, 128(582):1095–1135.

Xie, S. and Zhang, M. (2000). Impact of the convection triggering function on single-column model simulations. *Journal of Geophysical Research: Atmospheres*, 105(D11):14983–14996.

Xu, K.-M. and Randall, D. A. (2001). Updraft and downdraft statistics of simulated tropical and midlatitude cumulus convection. *Journal of the atmospheric sciences*, 58(13):1630–1649.

Yang, D. and Seidel, S. D. (2020). The incredible lightness of water vapor. *Journal of Climate*, 33(7):2841–2851.

Yang, D., Zhou, W., and Seidel, S. D. (2022). Substantial influence of vapour buoyancy on tropospheric air temperature and subtropical cloud. *Nature Geoscience*, 15(10):781–788.

Yano, J.-I. and Plant, R. (2012). Convective quasi-equilibrium. *Reviews of Geophysics*, 50(4).

Yeo, K. and Romps, D. M. (2013). Measurement of convective entrainment using lagrangian particles. *Journal of the Atmospheric Sciences*, 70(1):266–277.

Yukimoto, S., Koshiro, T., Kawai, H., Oshima, N., Yoshida, K., Urakawa, S., Tsujino, H., Deushi, M., Tanaka, T., Hosaka, M., Yoshimura, H., Shindo, E., Mizuta, R., Ishii, M., Obata, A., and Adachi, Y. (2019). MRI MRI-ESM2.0 model output prepared for CMIP6 CMIP historical.

Yukimoto, S., Yoshimura, H., Hosaka, M., Sakami, T., Tsujino, H., HIRABARA, M., Tanaka, T. Y., DEUSHI, M., OBATA, A., NAKANO, H., et al. (2011). Meteorological research institute-earth system model version 1 (mri-esm1)-model description. *Technical Reports of the Meteorological Research Institute*, (64):92.

Zhang, C., Xie, S., Tao, C., Tang, S., Emmenegger, T., Neelin, J., Schiro, K., Lin, W., and Shaheen, Z. (2020a). The arm data-oriented metrics and diagnostics package for climate

models: A new tool for evaluating climate models with field data. *Bulletin of the American Meteorological Society*, 101(10):E1619–E1627.

Zhang, C., Xie, S., Tao, C., Tang, S., Emmenegger, T., Neelin, J. D., Schiro, K. A., Lin, W., and Shaheen, Z. (2020b). The ARM data-oriented metrics and diagnostics package for climate models — a new tool for evaluating climate models with field data. *BAMS*, page submitted.

Zhang, G. J. (2009). Effects of entrainment on convective available potential energy and closure assumptions in convection parameterization. *J. Geophys. Res.*, 114.

Zhang, G. J. and McFarlane, N. A. (1995). Role of convective scale momentum transport in climate simulation. *J. Geophys. Res.*, 100:1417–1426.

Zhang, Y. and Klein, S. A. (2010). Mechanisms affecting the transition from shallow to deep convection over land: Inferences from observations of the diurnal cycle collected at the arm southern great plains site. *Journal of the Atmospheric Sciences*, 67(9):2943–2959.

Zhang, Y., Xie, S., Lin, W., Klein, S. A., Zelinka, M., Ma, P.-L., Rasch, P. J., Qian, Y., Tang, Q., and Ma, H.-Y. (2019). Evaluation of clouds in version 1 of the e3sm atmosphere model with satellite simulators. *Journal of Advances in Modeling Earth Systems*, 11(5):1253–1268.

Zhao, M., Held, I. M., Lin, S. J., and Vecchi, G. A. (2009). Simulations of global hurricane climatology, interannual variability, and response to global warming using a 50-km resolution GCM. *J. Climate*, 22:6653–6678.

Zhou, W. and Xie, S.-P. (2019). A conceptual spectral plume model for understanding tropical temperature profile and convective updraft velocities. *Journal of the Atmospheric Sciences*, 76(9):2801–2814.

Zhu, H. and Hendon, H. H. (2015). Role of large-scale moisture advection for simulation of

the mjo with increased entrainment. *Quarterly Journal of the Royal Meteorological Society*, 141(691):2127–2136.

Zuidema, P., Torri, G., Muller, C., and Chandra, A. (2017). A survey of precipitation-induced atmospheric cold pools over oceans and their interactions with the larger-scale environment. *Surveys in Geophysics*, 38(6):1283–1305.